UNIVERSITY OF CALIFORNIA
RIVERSIDE

A Mechanistic Exploration of Porous Carbons derived from Simple Polysaccharides with Embedded Metal Nanoparticles and their Relevance to Environmental and Electrochemical Applications

A Dissertation submitted in partial satisfaction of
the requirements for the degree of

Doctor of Philosophy

in

Materials Science and Engineering

by

Fabian Ellsworth Villalobos

December 2018

Dissertation Committee:

Dr. Cengiz Ozkan, Co-Chairperson
Dr. Mihri Ozkan, Co-Chairperson
Dr. Kambiz Vafai
Dr. Juchen Guo

The Dissertation of Fabian Ellsworth Villalobos is approved:

_____

_____

_____

Committee Co-Chairperson

_____

Committee Co-Chairperson

University of California, Riverside

Acknowledgments

I am grateful to my co-advisors, Dr. Cengiz Ozkan and Dr. Mihri Ozkan. Without their support and paternal nature, I would not have had the opportunity to conduct research, let alone become a dedicated scientist. They welcomed me into their lab as a Master's student and gave me an offer I couldn't refuse. This work represents the gratitude I feel for their help.

I would like to thank my lab mates for their help in all respects, from emotional and spiritual, to scientific and logical. I would especially like to thank Dr. Andrew J Patalano, for without his organic chemistry background, the following work could not have been accomplished. Our fervent debates and clash of ideologies served to forge us into accomplished scientists and for that I am grateful. I would also like to thank Daisy Patino for introducing me to my project and thesis, and without her I would not have had the proper footing to navigate the Ozkan Lab. Likewise, the healthy discussions and debates the Ozkan group fosters lead me to my system of organization, literature review, experimentation, and writing. For this I say thank you to Arash Mirjalili, Pedro Peña, Yige Li, Bo Dong, and Taner Zerrin. I would also like to thank Jingjing Liu for going through the last few months before our dissertation together, she knows how hard it was to put together the data needed to complete this work. I owe a great deal of gratitude to my undergraduates who toiled in the lab and contributed toward the data collection. I would like to thank Evan Jauregui, Melissa Schellinger-Gutierrez, Nicholas Roskopf, Jason Zhang, and Maria Renteria. Without their help and great attitudes, this work would have been too much to bare alone and I wish them success in their endeavors.

There are a great deal of people outside of the Ozkan group to whom I also owe my thanks. Steven Herrera did much to get me into graduate school as well as getting me out. Without his support and attitude, I would not be exiting in a timely manner. He also contributed to the carbon foam project with his expertise in Micro-CT. I am glad to have had him as a groomsmen. The help I received from Nicholas Derimow was multi-faceted, from the scientific to the absurd, his company brought a sense of tranquility to my often chaotic thoughts. His expertise was invaluable in my search to explain the metallurgical components of the project as well as the microscopy. I am truly grateful to have had him in my life during this time. Ece Ayatn-Coleman contributed her knowledge in Raman, peak-fitting, and analysis and I am appreciative of her skills. I often thought she was one of the most intelligent students in the MSE program and her help only confirmed my suspicions. Finally, I am appreciative of my fellow MSE students, including but not limited to: Christian Roach, Devin Coleman, Trevor Clark, Brandon Davis, Thomas Duger, Nicholas Yaraghi, Jesus Rivera, Maximilian Mayther, Melina Fuentes, Austin Woodard, and too many more to name.

To my loving wife. She put up with my nonsense, goofiness, and beard. She deserves more than I can give her and I will try my best to live up to her expectations. I love her so much and I wouldn't have survived without her. I love you.

To my parents for all their support, love, and compassion. To my mother for her drive and determination to get me the opportunities that I am able to take advantage of. To my father for his motivation and energy. To my stepfather for his discipline and sense of duty. To my brother, I hope he goes on to have more success than I.

ABSTRACT OF THE DISSERTATION

A Mechanistic Exploration of Porous Carbons derived from Simple Polysaccharides with Embedded Metal Nanoparticles and their Relevance to Environmental and Electrochemical Applications

by

Fabian Ellsworth Villalobos

Doctor of Philosophy, Graduate Program in Materials Science and Engineering
University of California, Riverside, December 2018
Dr. Cengiz Ozkan, Co-Chairperson
Dr. Mirhi Ozkan, Co-Chairperson

Presented herein are a review of climate change, renewable energy, and the need for energy storage along with a review of oil spills and the need for alternative methods of oil recovery, and finally the potential for carbon foams to address the needs for both as demonstrated by the research accomplished. Research performed with respect to carbon foams includes their polymerization from simple sugars; mechanisms for the growth of embedded metal particles (ranging from the micron- to nano-size); the encapsulation by graphite of metals with sufficient carbon solubility; and utilization of carbon solubility to use the foam as a substrate for growth of carbon nanotubes and graphene; and applications of the varieties of foams generated during the course of the research. A mechanism is proposed for the oxidation of simple polysaccharides and monosaccharides for the polymerization of the carbon foam from soluble precursors in aqueous solution a gel-resin capable of volumetric expansion commonly termed a carbon foam. The analysis of new carbon foams using a variety of metal

nitrate precursors to generate alternative foams is presented using a variety of characterization techniques such as XRD, Raman, Micro-CT, BET, ImageJ software, SEM, EDS, STEM, and EELS. Analysis of the carbon nanotubes grown on carbon foam substrates was performed using XRD, Raman, SAS statistical software, SEM, and TEM. Applications of carbon foams with embedded metal particles and carbon nanotubes include: a hierarchical sponge with oleophilic and hydrophobic properties as a selective oil sorbent material; carbon nanotube coated micron-sized particle as active material in an electrochemical double-layer capacitor; and the use of carbon foams as a sacrificial scaffold for the growth of metal foams. A review of the research concludes the thesis as well as recommendations and potential projects for those who may continue the study of carbon foams and their applications.

Contents

List of Figures

List of Tables

Chapter 1

Introduction

1.1 Climate, Energy, and Storage

The drive towards clean energy storage research stems from the scientific community's concern for climate change and its affect on our planet [151, 171, 49, 91, 127, 101]. Although unprecedented economic growth brought many out of poverty, the industrial revolution was built on a foundation of energy consumption which increased the productivity of farming, transportation, and trade. This energy was born of our predecessor species, mainly the dinosaurs. Millions of years of tectonic forces produced coal, oil, and tar from the carbon remains of those species from long ago. It was not until the steam engine and the study of thermodynamics did our energy production increase to the point that CO_2 and CH_4 emissions outpaced nature's ability to consume them in the form of plant matter and bacteria, thereby off-balancing the global carbon cycle equilibrium. This is increasing the average heat capacity of our atmosphere, allowing it to retain heat from the sun and gradually increase the average temperature of the earth as a whole. The increase in global

average temperature could have a variety of possible effects [141]. The transportation sector of our global economy consumed 31% of the total final energy consumption in 2006. Road transport contributed 82% to this number and produced about 25% of the CO_2 emissions that year [171]. Targeting road transport and their fuel sources then becomes a strategy worth pursuing to aid in preventing climate change or at the very least, reducing its effects.

1.1.1 Climate Change and its Potential Risks

An increase in global average temperature between 2°C and 11°C is predicted by the end of the 21st century [89]. By changing the heat trapping capacity of the earth, carbon emissions are imposing a number of threats [141] unheard of since the dawn of human history. The increase in heat accelerates the rate at which ice melts at the poles and alters the natural ocean cycles that regulate the temperature of earth's climate. Concurrently, sea levels are expected to rise, endangering the populations of coastal areas world wide. Indeed, there are already disappearing beaches, islands, and communities [82].

Melting Glaciers Though the threat of melting glaciers may seem to be limited to rising sea levels, more complicated and nuanced problems of greater urgency are not regularly communicated to the public. Roughly one sixth of the earth's population relies upon glaciers for fresh water during summer months [14]. Glaciers act as water storage during the colder seasons, keeping the water frozen until the warmer dry season melts the snow and ice pack; it then flows into water supplies like the Yangtze River in China and the Quelccaya in the South American Andes [14]. China alone has 46,377 glaciers, 80% of which are in a state of retreat [128]. These glaciers not only feed water into rivers in China, but also its

neighboring countries. Alterations in the hydrological cycle in snowmelt dominated regions could leave them without adequate water storage capacity, endangering one sixth of the globe with water shortages. Limited fresh water resources could have the potential to be become sources of tension between these populations and regions in the future. A water supply crisis is imminent and water management techniques will not be enough to help without significant changes to agriculture, industry, and lifestyle.

Intensified Weather Patterns Superstorms such as Sandy, Harvey, Irma, Katrina, Maria, Wilma, and Irene have been devastating to the affected communities. Although the number of storms originating in the Atlantic and Pacific Oceans has not been increasing, hurricanes and tropical storms have become more variable in intensity [98] which means that extreme weather events thought to be rare could become more common. Droughts in Africa and the Middle East are becoming more common and are lasting longer in duration [98, 62]. Low precipitation is requisite for moisture deficits and high temperatures can exacerbate evaporation. This works to lower the moisture content in the soil which can increase the risk of wildfires, excessive ground water withdrawal, decreased hydroelectric power production, and damage ecological habits [40]. In Syria, there have been indications as early as 2008 that winter rainfall has been reducing year on end and is thought to be a leading cause in the Syrian Civil War [62]. Between 2006 and 2009, 1.3million Syrian citizens were affected by agricultural shortages which forced them to move towards the outskirts of Aleppo, Damascus, and Homs[62]; the same cities now torn apart by war. Areas with forests that begin to experience multi-year droughts then become prone to wildfires as is the case in California. In the 1980's, summer and spring temperatures began to rise above

the norm. Spring snowmelt also started to begin earlier in the year. These factors combined to lower moisture in California, and these same factors correlate with appearance of longer wildfire seasons, longer wildfire duration, and higher frequency of wildfires. This has lead federal land-management agencies to regularly exceed $1billion in firefighting expenditures annually [168]. The growing intensity of weather patterns is leading to massive costs for our federal and state governments and will only get worse with time.

Ocean Acidification Shallow marine organisms that rely upon carbonate calcification are expected to be affected by ocean acidification. This is because roughly one third of CO_2 that is emitted into the atmosphere is absorbed into the ocean where is disrupts the concentration of carbonate ($CO_3{}^{2-}$) and lowers the pH, thus acidifying the aqueous environment [90, 88]. As CO_2 dissolves into aqueous conditions, it undergoes hydrolysis reactions and produces $CO_3{}^{2-}$ which can react with minerals in the ocean to produce calcium carbonate ($CaCO_3$). Calcifying creatures like corals, bivalves, plankton, echinoderms, and crustaceans then use the de-mineralized Ca to construct their shells and supporting structures [88, 90]. As the concentration of $CO_3{}^{2-}$ rises, more calcium is stripped from whatever source is in the ocean, including the shells of these marine calcifiers. This can have negative impacts on the fertilization, cleavage, larva, settlement, and reproductive stages [90], preventing them from forming protective shells and skeletal structures. These organisms construct both aragonite and calcite phases of $CaCO_3$ and both are affected by the imbalance of carbonate in the ocean. Aragonite has more solubility in ocean conditions and organisms reliant upon it are predicted to be affected sooner. Carbonate levels in the high-latitude oceans are predicted to become saturated by 2050, lowering the level of aragonite, dissolving the

shells of creatures [90]. The disruption of fauna at the base of the food chain will fail to sustain those species dependent on their continued survival. Species dependent on coral reefs, crustaceans, plankton, and bivalves will all lose vital habitats and food supplies.

Permafrost The natural fluxes of carbon in and out of the atmosphere are an order of magnitude larger than that contributed by humans. Any changes in the natural carbon cycle also affect the bulk contributor towards CO_2 and CH_4 emissions. There is an estimated 1672Pg (petagrams, 1Pg = 1 billion metric tons) of carbon in the northern circumpolar permafrost zone alone [141]. As the global average temperature rises, permafrost could begin to thaw and melt and microbial decomposition of peatland vegetable matter would increase rapidly, releasing CO_2 and mineral carbon that was frozen. Permafrost is made up of an active surface layer that thaws and freezes with the seasons and can vary between a few tens of centimeters up to 2m. Below is the ice-rich transition zone which separates the active layer from the more stable permafrost below which can occupy a few meters. The permafrost region below can contain up to 80% ice by volume. This means that any thawing and melting would change not only the carbon content of the environment, but the topology as well, reshaping the ecosystem with it [141]. Initially, thawed lands will form depressions and new wetlands and ponds will appear, interconnected by new drainage networks. This could temporarily establish new aquatic communities in places where terrestial species once roamed. But over time surface water would drain into groundwater systems reducing fresh water habitats [79].

A drastic and permanent increase in temperature is not necessary; by definition, only brief instances above 0°C are enough to melt ice and begin decomposition. As time

passes and temperatures rise, man made carbon emissions could quite possibly thaw a sleeping giant. These terrestrial and ocean responses to climate change may add up to twice the carbon emissions humans are responsible for emitting [141].

Sea Level Rise Possibly the most frightening challenges to global society and order are presented by the increase in sea level. Four separate satellites estimate that not only has the sea level risen 3±0.4mm/y the past 25 years, but that rate is increasing by 0.084±0.025mm/y^2 [119]. At that acceleration and growth rate, an increase in 65cm is expected by the year 2100. This is a global average and a conservative estimate that does not take into account additional increases in carbon emissions over time, which is still happening. Localized increases in thermal expansion and slowing of the North Atlantic Ocean circulation threaten cities on the East Coast of the United States with as much as 18 inches of water [98]. Inevitable hurricane and winter storm surges threaten some of the United States' most populous cities and centers of economy, politics, culture, and eduction. Damage to ecosystems that can result from flooding include:

- Submersion of low-lying land
- Erosion of beaches
- Conversion of wetlands to open water
- Increase of salinity in estuaries

Even a 2°C rise in global average temperature is estimated to rise the sea level by 1.5-4m by the year 2300. Within two centuries, global sea levels will have forced millions

of people to retreat from the coastal regions. Mass migration and immigration will force developing and developed governments to either work together or apart. National and international political alliances will be strained. Armed conflict is almost a guarantee. Sea level rise may sound like a nuisance, but it is more than that, it is possibly the single greatest challenge humanity will face in the coming centuries.

1.1.2 Clean Energy

Almost all forms of energy have origins in the sun. The sun's light heats our planet's atmosphere, driving a breeze that turns our wind mills and powers our climates; moving clouds and water vapor from oceans to mountain tops. There, water rains and snows onto the land forming lakes and rivers that flow back to the ocean, and on its way, we use it to power hydroelectric dams and water wheels. The water satiates plants' thirst as they absorb the suns rays to sustain themselves in a process called photosynthesis. These plants in turn nourish animals and fungi, which feeds even more animals. Eventually, plants and animals decompose and terrestrial forces transform these forgotten souls into the fossil fuels that we burn today. Now we have once again looked back toward the sun to feed our solar cells and inspire our nuclear aspirations.

To combat the threats of climate change, electrification of fossil fuel dependent motors is a requisite for cutting carbon emissions. This may seem like a complete solution at first glance, but upon further inspection, it can be intuited that electrification will only cut off carbon emissions from the end user, not from the coal and natural gas plants which generate the majority of emissions world wide. These emissions must be included in any realistic effort to cut down on carbon emissions. Clearly this implies the vast majority of

energy production in the world will have to change towards renewable sources [179]. But more than this, not utilizing renewable sources is a waste of perfectly good energy already available to our world. Like a faucet that is permanently left running; solar, wind, and others are sources of energy that go unused every day. It is time to put a cup under the faucet and not let a drop go to waste.

Solar About 5 kWh/m^2 of incident light lands on the United States' surface every day. This equates to 4000 times the United States' energy production in 2005, making photovoltaic (PV) solar a leading candidate for clean energy generation [107]. Though much of the surface area is not feasible to harness and although our current technology can only capture 20% of that light, this still leaves the uncaptured sunlight at well over 8 times that which is being consumed [107]. Concentrator mirrors can increase this efficiency up to 40%, though many commercial PV systems fall below 10%. After a large number of years of declining prices, the price of installation has started to slow down and is currently below \$4/W [13] which makes it more than competitive with coal. This makes rooftop solar installations a viable source of energy production in a distributed energy network. Many novel concepts are being proposed that integrate rooftop solar with electric vehicles. For example: parking lots and structures inhabit an estimated 19 billion m^2 in the United States alone [107]. Most are not structures and are simply plots of asphalt surrounding grocery and shopping centers, office buildings, and educational institutions. The benefits of rooftop solar in parking lots is multifaceted:

- No new land is needed for installation

- No major structural renovations are needed
- Electricity could supply parked EVs and hybrids
- Provides shade and reduces fuel consumption from air-conditioning

Novel systems like these show the ingenuity possible with renewable energy sources. However each source of energy has its own drawbacks. Currently, solar cell production uses fossil fuels in the manufacturing process, although when sufficient solar installations are available, these emissions can be negated. Unfortunately, cadmium telleride thin film solar cells produce cadmium waste in the manufacturing process as well as when mining ore. Inherent disadvantageous cannot be ignored either: solar panels do not produce electricity at night and during seasonal changes the tilt of the earth's axis reduces light exposed to certain regions of the earth's surface, diminishing the electricity generated. That being said, even during the winter season, most solar installations generate a net surplus of energy at mid day. Additionally, energy generated from solar is predictable, a very important quality when servicing a large population, and thus remains a strong contender for replacing fossil fuels.

Wind Energy from land-based wind has a yearly potential twice what was needed by the US in 2005. Recently, the price of wind has dropped to less than \$0.50/W as installations of wind turbines have increased in the last two decades [107]. Globally, the estimated capacity of wind power has grown to 487GW which represents 5% of the global electric supply in 2016 [117]. This growth can be attributed to the smaller footprint required by turbines. Many farmers and ranchers in the United States' South West have been slowly installing

wind turbines in their fields. The advantage is two fold: unused land on the premises are now utilized and a more stable income is generated that can mitigate the financial hardship of low yield seasons. The concern with wind is the lack of consistence when compared to solar; a less predictable source of energy is not favorable for investment. A gust of wind can vary at an hourly level or even minute to minute.

Offshore, or Nautical wind, could also provide an additional 70% of the energy required in 2005 [107] and they provide additional benefits as well. Many coastal regions are large population centers requiring more energy than other parts of the nation. Limited real estate in these markets make solar installations and terrestrial wind farms difficult to compete. Having energy production offshore does not conflict with land usage and requires little to no investment in long-distance transmission [117]. The wind over oceans is also steadier, providing more reliable output [107]. Along the Eastern Coast conditions make nautical wind favorable to solar in the North East, especially in New York, Massachusetts, Connecticut, and Rhode Island. Had they been constructed along the East Coast, offshore wind could have replaced 20,000kg of CO_2 per MWh of wind, in conjunction with reducing emissions from SO_2 and particulate matter (PM), generated from coal and natural gas from 2007-2016 [117]. In fact, many European countries rely heavily on nautical wind, while the United States only had 30MW of offshore installation in 2016. This is an area where the United States has room for growth.

1.1.3 Energy Storage

Because not any one clean energy source is fully capable of providing for citizens needs, energy storage plays a key role in the transition from fossil fuels. Solar and wind,

though the largest and most popular clean energy sources today, are still limited by their ability to provide energy and power at all times of the day. It is then paramount that novel methods of energy storage be developed to supply electricity when the sun is not shining and the wind is not blowing. Traditionally, hydroelectric dams have served as a reservoir for large scale energy production and have provided the United States, China, and Europe with power for decades. Though there are energy losses while transmitting electricity at high voltage through power lines, the major set back of hydroelectric dams is their impact on local ecosystems and peoples while not being able to provide energy on the go. These dams can provide direct energy to power buildings, equipment, and transportation connected to the grid, but not to portable systems. To fill this void, rechargeable batteries and supercapacitors are advantageous. Electrical energy can be stored in two fundamentally different ways:

1. Through chemical potential whereby Faradaic processes transfer electrons through oxidation and reduction of electrochemically active species as in the case of batteries

2. Electrostatically, which is a non-Faradaic method whereby electrons are stored at two oppositely charged plates as is the case in capacitors.

The highly reversible processes of batteries and capacitors means the efficiencies of these two methods of storage are greater than those of combustible fuels, which are limited by the thermodynamics of the Carnot cycle [31].

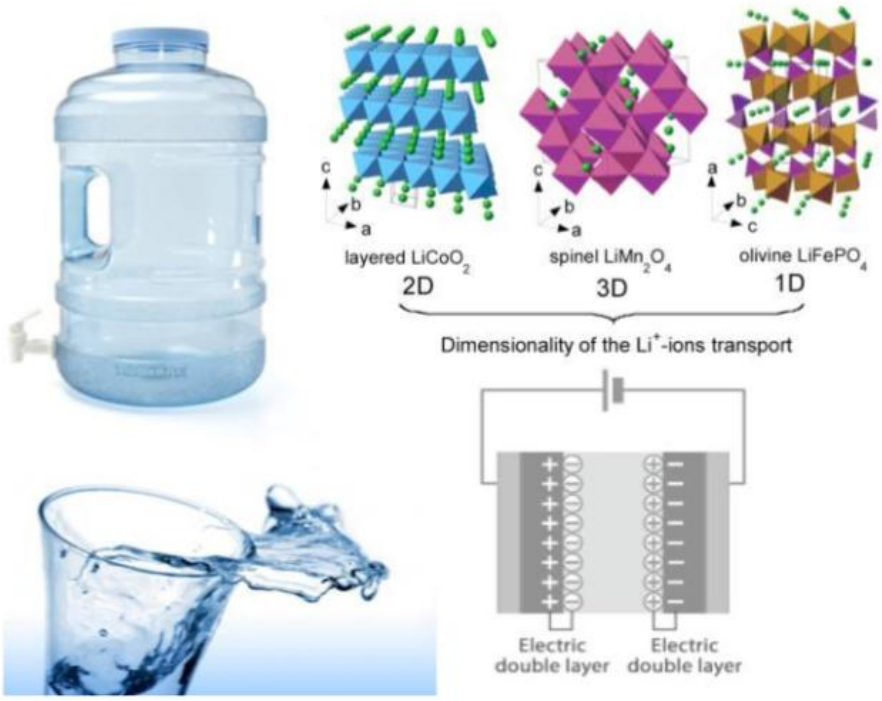

Figure 1.1: Visualizing the difference between a battery and a capacitor. Modified from [12]

1.1.4 Battery vs Capacitor

Rechargeable batteries and supercapacitors can fill the gap left between direct energy sources and the needs of an increasingly mobile and decentralized society. Rechargeable battery chemistries like lithium-ion, nickel-metal hydride, and lead-acid have captured a large share of the mobile energy storage market which includes: smart phones, laptop computers, and electric vehicles. This is due to their high specific capacity (mAh/g), specific energy (Wh/g), and energy density (Wh/L). The virtue of their materials' electrochemical properties has lead to this market domination. However, these systems lack the ability to provide that same energy at a high rate of discharge known as power density (W/g or W/L) which are required for power tools, voltage stabilizers, and accelerating electric vehicles. Conversely, capacitors are devices that can deliver the energy they store at high speed although they have their own drawbacks; they often hold very little total energy and are thus not energy dense.

The difference between batteries and capacitors can be seen by analogy in Figure 1.1. Batteries work by storing chemical ions in the void space within the atomic crystal structure or by reacting with the material utilized. Because of this, batteries can store more energy, but those voids also restrict the ion's movement, slowing down the chemical reaction, and thus the release of energy. A capacitor works by storing chemical ions on the surface of the chosen material which affords them greater freedom of motion, and consequently they are quick to release that energy. However their surface area is much smaller and therefore limits how much they can store [146]. Its like the difference between a tank of water and a cup. The tank can hold much more water, but only lets out a little at a time; the cup

only holds a small amount but can empty its volume very quickly. A nuanced presentation of the electrochemical differences and similarities will be discussed in Section 5.1. These two systems are complimentary, and both must be discussed when pursuing energy storage solutions.

1.2 Environmental Clean up and Oil Spills

Today's economy has been reliant upon fossil fuels for well over a century and in that time we have learned that our modern standard of living is often acquired at the expense of our environment. The production of essential fuels, lubricants, and polymers are built upon the extraction and refining of crude oil [53]. Intermittently, during the drilling of wells and transportation of crude, we are confronted with negligence and unforeseen events resulting in spills as seen in Table 1.1. These catastrophes inflict damage on multiple fronts. Nearby marshland and beaches experience a reduction in animal life and vegetation, which in turn can lead to erosion of the land [145]. In the ocean, coral reefs die off and habitats for coastal dwellers are lost [140]. Large and small fishing operations suffer loss of income due to tainted shrimp, fish, and oysters by oil and dispersants for generations of game [162]. As a result the tourism industry falls into decline and hundreds of thousands of jobs are affected [132] and entire economies can end up in disrepair as a result of a single spill.

Over time we have managed to learn from past mishaps and have been able to decrease the number of oil spills for the last 40 years as seen in Figure 1.2. Although large oil tanker spills ($>$ 700 tonnes) have decreased in that period, small tanker spills ($<$ 7 tonnes) have increased and are often not reported at all [158]. But this neglects the

Table 1.1: Major Oil Spill Incidents [77, 153]

Incident	**Location**	**Date**	**Amount** (tons)
Exxon Valdez	Alaska	March 24, 1989	3.6×10^4
Gulf War	Iraq, Persian Gulf	January 23, 1991	4×10^4
ABT Summer	Angola	May 28, 1991	26×10^4
MV Braer	Scotland	January 5, 1993	9×10^4
Orapin Global-Evoikos Collision	Malaysia	October 15, 1997	2×10^4
Nakhodka	Japan	January 2, 1997	4.5×10^3
Jessica	Galapagos Islands	January 20, 2001	70×10^4
Prestige	Spain	November 13, 2002	4×10^4
Deepwater Horizon	Gulf of Mexico	April 20, 2010	62.7×10^4

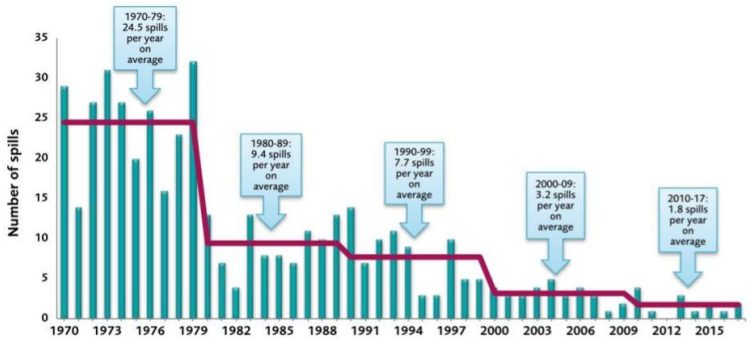

Figure 1.2: Number of Large Spill (>700 tonnes) from 1970-2017. Reproduced from [158]

fact that "tanker and oil rig spills only account for 12.5% and 1.5% of the total oil spilled respectively" and the principle loss of oil occurs while being transported or during storage [77]. Renewable energy research and production will likely decrease our future dependence on fossil fuels, but these technologies are still in their early stages of growth and adoption. Even so, renewables will not entirely replace fossil fuels for some processes, suggesting oil spills will continue to occur. Thus, recovery methods are needed to mitigate any potential spills and accidents.

1.2.1 Current Methods

Currently, three methods are recommended for recovery of crude oil during a spill at sea: skimming, dispersants, and combustion [153, 77]. Skimming involves the use of smaller vessels dragging floating nets or absorbent materials that work in several ways, usually by encircling the pools of floating crude and withdrawing the net to collect the oil in containers. Chemical dispersants work by breaking up larger collectives of oil into microscopic droplets that can be more easily dissolved in the ocean. Studies on marine life may not be conducted thoroughly before use and some dispersants can reduce the survival rate of coral larvae, leading to collapse of entire colonies [63]. Combustion involves in situ ignition of floating pools of oil that results in the emission of CO_2 and Polycyclic Aromatic Hydrocarbon (PAH) compounds [19]. Increased CO_2 emissions are responsible for manmade climate change while PAH compounds may increase susceptibility to breast cancer in women [135] and childhood obesity in children of women exposed to high levels of PAH compounds [136]. These were the methods employed after the explosion at the Deepwater Horizon oil well in the Gulf of Mexico in 2010 [153]. During the incident, an estimated 4.9 million barrels of oil leaked into the Gulf of Mexico [153, 32] until the well was capped. Of this, as seen in Figure 1.3, roughly 25% of the total was recovered via skimming or burned releasing CO_2 and PAH into the atmosphere. Another 24% was chemically dispersed and 25% was dispersed as a result of natural currents and weather. The remaining 26% is below the surface or washed ashore [153]. It is clear that environmentally benign methods with greater efficacy are needed.

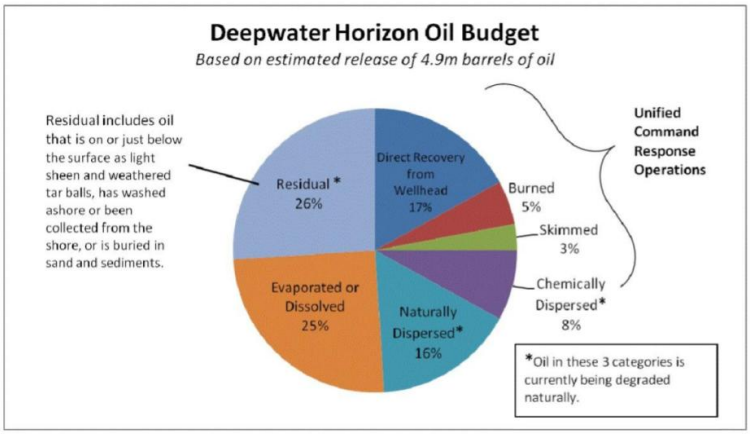

Figure 1.3: Shows current best estimates for what happened to the leaked oil during the BP Oil Spill in 2010 [153]

1.3 Carbon Allotropes

Carbon is the basic building block of life and as such, the element deserves a closer look if only for appreciation. Carbon is the 6th element in the periodic table, the 4th most abundant in the universe, and holds 4 electrons in its valence shell. These 4 electrons are responsible for the vast assortment of bonds carbon can form with other elements to produce molecules as varied as hydrocarbons, polymers, ceramics, metal-carbides, amino acids, and lipids. It is also responsible for the many allotropes, or alternative atomic arrangements, in which carbon can be naturally found and their corresponding properties as demonstrated in Figure 1.5. This work will focus on elemental carbon and some of its allotropes which can be separated into a few categories: Amorphous, Classical, New, and Nano [77].

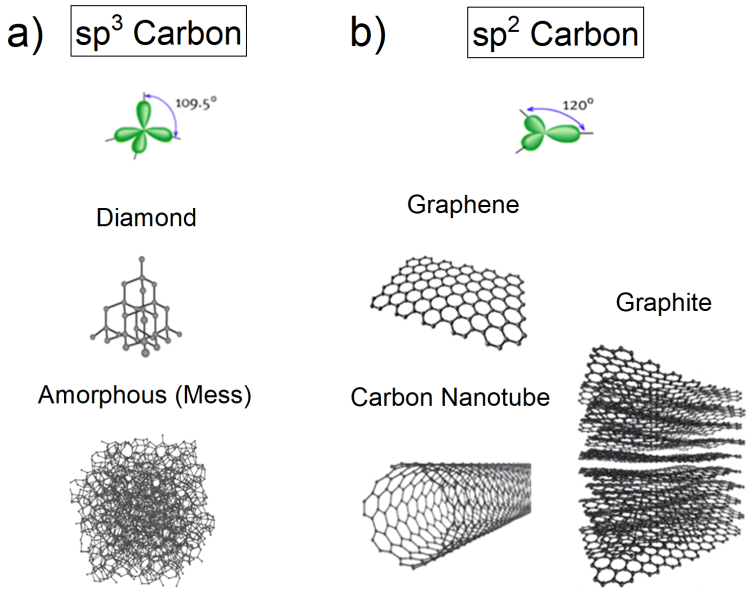

Figure 1.4: Common allotropes of carbon as a result of a) sp^3 bonds and b) sp^2 bonds. Modified from [85]

1.3.1 Classical Carbons: Diamond and Graphite

Before defining amorphous materials, it is wise to define crystalline materials. In materials science, a crystal is a repeating unit of atoms, ions, or molecules that extend in two - three dimensions of a lattice. Most people are familiar with these two allotropes which represent two different bonds and consequently the dimensional structures that can be formed by carbons: sp^3 and sp^2.

Diamond As stated before, the 4 electrons in carbon's valence shell form a tetrahedral arrangement in order to minimize electron-electron interactions, this maximizes the distance between electrons so that they form an 109.5°angle with each other and is referred to as an sp^3 bond. In such a case where each individual sp^3 carbon is arranged so that an order in three dimensions is formed, the structure is referred to as diamond. Due to its crystalline structure, diamonds are among the hardest substances known to man and are useful in cutting instruments. Diamond is also insulating, meaning that electrical currents do not pass easily through them. However, diamonds are very good conductors of heat. Diamonds are naturally formed under immense pressure within the core of the earth, but they are not the most stable form of carbon, eventually all diamonds will revert to graphite.

Graphite The most thermodynamically stable allotrope of carbon, graphite is built of sp^2 carbons which grants graphite its two dimensional layered structure. Graphite is actually layers of planar carbon stacked upon one another in an ABABAB pattern. Individual sheets of graphite are referred to as graphene. In sp^2 carbon, only 3 electrons are bonded to other atoms by hybridized sp^2 bonds, leaving a forth electron free to transfer from carbon to

carbon via overlapping p-orbitals which create a pi bond also known as a double bond. The 3 sp^2 bonds maximize the space between them and form a planar arrangement with a 120°angle, which determines the hexagonal structure of graphene and aromatic rings. The covalent sp^2 bond grants graphite strong anisotropy, but the pi bonds provide a weak Van der Waals force between layers, which allows the ease of removing individual graphene sheets. The free roaming electrons in these pi orbitals is also responsible for the high conductivity characteristic of graphite, graphene, and related carbon phases [77].

1.3.2 Amorphous Carbon

If a material is amorphous it is the opposite of crystalline; it has no crystal structure. Amorphous carbon compounds are usually a result of thermal treatments such as: combustion, pyrolysis, annealing, and chemical vapor deposition. Examples of common amorphous carbons are: charcoal, activated carbon, and soot. Amorphous carbons can consist of both sp^3 and sp^2 bonds. The 4 valence electrons in atomic carbon arrange themselves in a tetrahedral fashion and are responsible for the three dimensional structures found in carbon allotropes, however, in the case of amorphous carbon, the individual carbon atoms are not arranged in such a way as to grant order to the overall structure as in a diamond or graphite.

1.3.3 New Carbons: Diamond-like Carbon and Glassy Carbon

New carbons are classified by their non-crystalline structure at large orders of magnitude, but short range order. They are not graphitized into a stacked hexagonal lattice, but may contain short ordered layers. Nor are they compacted into a cubic diamond lattice

at large scales, but may contain a similar organization at the atomic scale.

Diamond-like Carbon Diamond-like carbon is amorphous, but consisting of a high fraction of sp^3 bonds and is considered a tetrahedral amorphous carbon. As the fraction of sp^3 bonds decreases, so too does the density of the material. This density is correlated with diamond-like carbons' thermal conductivity and Young's modulus. These carbons can range in purity from highly pure (lacking hydrogen bonds) to hydrogenated.

Glassy Carbon Though not completely crystalline like graphite, glassy carbon has short range hexagonal rings of sp^2 carbon similar to graphene. However, these sheets are limited to a few nanometers in length. These sheets layer upon each other, but instead of simply being offset by a few angstroms from the neighboring layer as in ABABAB stacking, the sheets are rotated out of phase. This rotational offset is referred to as turbostratic and the interlayer distance is 3.41Åcompared to graphite's 3.34Å. Typically glassy carbon is synthesized at high temperature, but could be converted to traditional graphite by first melting the compound. Glassy carbons appear glass-like in nature (though lacking optical transparency), have high hardness, and display gas impermeability.

1.3.4 Nano Carbons: Graphene, Carbon Nanotubes, and Fullerenes

Nano Carbon materials are defined by sp^2 carbons which shape the materials into a planar architecture. However, just as a sheet can be cut into geometries that can be rolled or folded into interesting three dimensional shapes, so too are the novel geometries of nano carbons formed from sheets of carbon. If a sheet is rolled into a cylinder, it can form a

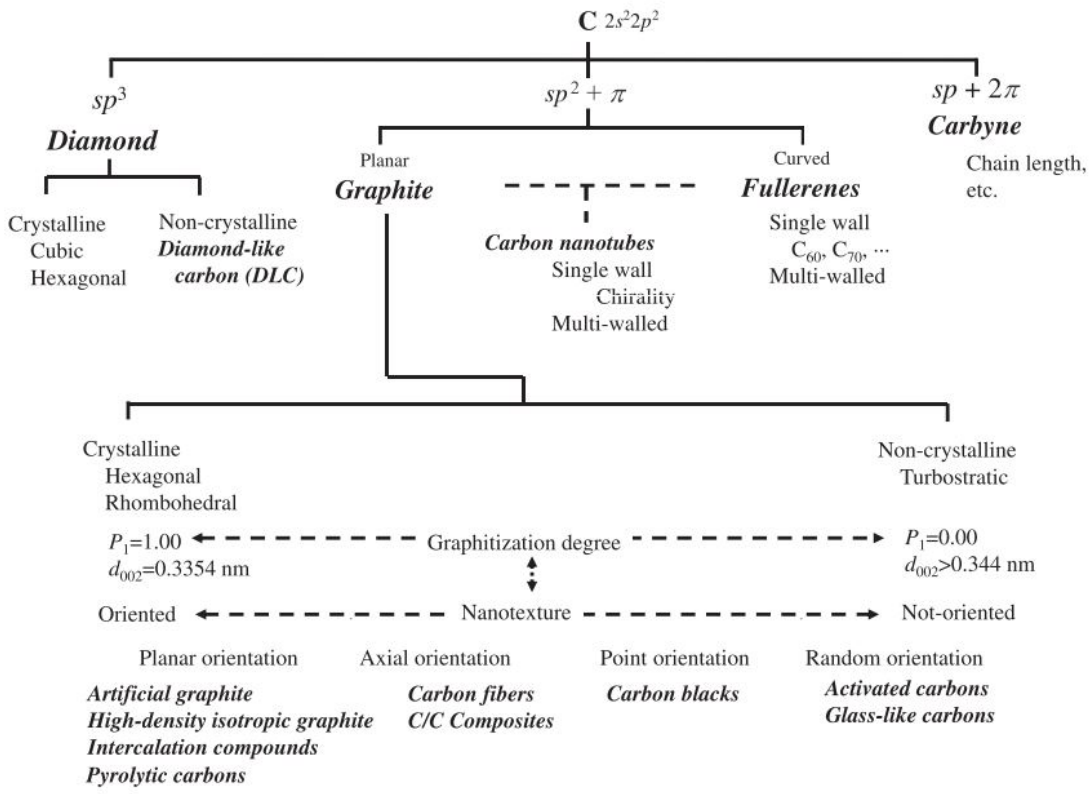

Figure 1.5: Classification of carbons phases and materials [77]

tube. In our case, graphene is used as the planar sheet. A carbon nanotube is simply a graphene sheet rolled and bonded to itself as seen in Figure 1.4. Though this is not how carbon nanotubes are grown in experimentation (they are grown from one end of the tube outward) the rolled up explanation is easy to visualize. Just as carbon nanotubes are rolled into sheets, fullerenes are graphene sheets rolled into a sphere or ball.

Graphene As stated previously, graphene is a single atomic layer of carbon with a hexagonal crystal structure of thickness approximately 3.45Å. This hexagonal lattice is determined by the 120°angle of sp^2 carbon. The pi bond, or double bond, of graphene allows for transfer of electrons into the conductance band due to a lack of a band gap. The high conductivity of graphene also allows for excellent heat conduction as well. Graphene's pi bonds are responsible for the high mechanical tensile strength which is over 100x greater than steel. Graphene is also able to absorb white light.

Carbon Nanotubes Unlike graphene, carbon nanotubes (CNTs) can be either metallic, quasi-metallic, or semiconducting depending on the chirality, or twist, of the planar graphene sheet. When metallic, CNTs offer good electronic and thermal conductivity. When semiconducting, CNTs act as though they are p-type field effect transistors, that is, they lack an electronic charge and electron holes migrate through their walls. CNTs are sensitive to charge transfer and chemical doping because of this. Like graphene, CNTs demonstrate high tensile strength and ductility.

Fullerenes Also known as "Bucky Balls", these carbon spheres range in size from 60 carbon atoms in a soccer ball arrangement to 540 carbons in an icosahedral shape. Though

the carbon atoms contain sp^2 bonds, the number of carbons in a ring can vary from 4 to 7, creating square, pentagonal, and heptagonal rings in addition to hexagonal rings. These different numbered rings place stress on the covalent bond and change the bond angle accordingly. Because of the stress of these bonds angles, fullerenes are not as conductive as carbon nanotubes or graphene. Bucky Balls can be found naturally in soot, after lightening strikes, and in deep space.

1.3.5 *sp* Carbon

A final allotrope of carbon not yet discussed it that of *sp* carbon, also known as carbyne. Carbynes contain a triple bond with other carbons atoms along with a single bond 180°angled opposite the triple bond. This leads to a linear or chain-like molecule with alternating single and triple bonds. These materials are very hard to synthesize thus making them rare. They have only been detected in space or synthesized within a CNT for stability and protection from chemical reaction [143]. Should the mass production of carbynes ever succeed, the material would be the strongest material known to man. Further research is needed to find suitable methods of synthesis.

1.4 Porous Carbons and their Applications

Porous carbons have a large surface area due to the network of void spaces fashioned by carbonization of gases, particles, and escaping gases. The pore size of these materials can range from macropores (>50nm), mesopores (50nm - 2nm), and micropores (<2nm). Porous carbons are typically amorphous in nature, but can be graphitized when

annealed at high temperatures (>1300°C). These materials can be prepared as powders, pellets, fibers and cloths. Porous carbons can be found in many applications and devices in the fields of electrochemical energy storage; liquid and gas filtration, and molecular sieving; and storage of liquid and gaseous compounds.

1.4.1 Types of Porous Carbons

Activated Carbons The collected name for a group of porous carbon materials that exhibit mostly microporous structure is activated carbon. There are several methods to "activate" the removal of carbon for the purpose of creating micropores and mesopores. Physical processes that use gaseous compounds such as CO_2 and steam are very well known and have been heavily researched [70, 73, 77, 108]. The use of chemical processes such as alkaline hydroxides or metal particles to be implanted into the surface of carbon, heated to react with carbon, and washed to remove reacted species is also well known [70, 163]. Chemical removal of carbon is less energy intensive compared to physical processes which require higher temperatures, more complicated processing schemes, and devlier lower yield [70]. However chemical activation schemes require a washing step to rinse off chemical products.

Carbon Mats and Felts Natural fibrous materials have been sourced for use in precursor carbon mats and felts. These include cotton, milkweed, fir trees and carbon pitch which are then carbonized in an inert environment, leaving behind a fibrous and porous material. A carbon pitch, or tar, is a viscous polymer resin, usually a byproduct of petroleum processing or heat treatment of woody vegetation. The heat treatment of these precursors generates

fibers that can be then woven or entangled into a mat or felt. Carbon mats and felts can also be activated to increase their surface area and porosity. The ability to manufacture fibrous materials quickly and easily is attractive to researchers looking for scalable methods and renewable starting materials.

Carbon Foams This group of macroporous and mesoporous amorphous carbons were discovered as early as 1979, but it wasn't until 1996 that a Chinese group brought the discovery to a larger audience [77, 15]. Carbon foams started as exfoliated graphite flakes but soon grew to include gas-blown and templated carbons. In gas-blown carbon foams, gases within the precursor material are heated until evaporated and the escaping vapor leaves behind empty pores and a swiss cheese-like material. In templated carbons, easily removed spheres or particles are impregnated in a polymer precursor that is later carbonized in heat. The resulting material is then treated to remove the impregnated particles by chemical or physical means and a porous structure is left behind. The materials in this work are classified as carbon foams and further background will be provided in Section 4.2.

1.4.2 Applications

Applications of porous carbons are wide and vast. Electrochemical energy storage, filtration, and gaseous storage encompass so many fields of study and industries, that only a few will be discussed here.

Sorption The ability to sorb fluids allows for a variety of applications related to filtration and storage [149]. Indeed waste water treatment, water filters, and other devices all use activated carbons to separate contaminants from the water as well as other solvents. These

materials are valuable in separating liquids from solvents and vice versa in industries like pharmaceuticals and plastics. Carbon foams and felts have shown promise in use as oil sorbents and combined with their hydrophobic properties, can easily separate water from oil. Porous carbons are also applicable in separation of gaseous compounds. Activated carbons can be used to sorb CO_2, odors in refrigerators, and can also be applied to numerous industrial processes that require adsorption of vapors for safety and separation processes. Because these porous carbons separate fluids from another, they are simultaneously providing storage. All that is needed is a method to recuperate any sorbed compounds. Techniques for recovery include centrifugation and low pressure vacuum processing. The adsorption of gaseous materials also allows for separation processes to occur within the porous carbons themselves. By controlling the porosity, size and shape of pores, a so-called molecular sieve can be fabricated.

Electrodes Activated carbons have been long been used as conductive additives in electrodes since the 1800's and carbon foams have recently been explored as well. The surface area and porosity provide sites for electrolytes to adsorb onto the surface, creating a double layer capacitance in electrochemical supercapacitors and batteries. The conductivity of these carbons also help electron transfer within the electrodes and reduces the device's internal resistance and impedance by increasing contact between the active electrode material and the current collector. Some porous carbons can also be doped to add redox reactions to increase pseudo-capacitance in supercapacitors and conductivity in batteries. Porous carbons are integral to the success of today's energy storage industry and are likely to remain so for the foreseeable future.

Chapter 2

Investigation and Proposal of Synthesis Mechanisms

In general, when one is seeking to be creative in their attempt to create a new material, chemical, or technology, it is important to first delve into the fundamental principles, mechanisms, and minutiae that govern the material in question. A review of the previous work done by the group will be presented in this chapter as well as the literature and experiments that lead to a proposed mechanism for the polymerization of oxidized sugars, the growth of the porous bulk structure, and the phase separation of carbons from metals in solid solutions. The chapter will spend time in basic organic chemistry, binary phase diagrams, and thermodynamics. Chapter 3 will build upon the insights gained from study of the latter topics. For more information regarding the organic chemistry and potential use of waste carbohydrates as feedstock for carbon foam precursors, the reader is directed to the thesis of Dr. Andrew J. Patalano titled: "Thermal Processing, Strategies and Char-

acterization of Sustainable Nanomaterials". For the origin of the project and insights into the growth of graphene on copper substrates, the reader is directed to the thesis of Dr. Hamed H. Bay titled: "Design, Synthesis and Characterization of Novel Graphene-Based Nanoarchitectures for Sustainability".

2.1 Previous Work

The work of Hamed et al described the formation of iron nanoparticles embedded within a porous graphite matrix that displayed oleophilic and hydrophobic properties. This metal graphite sponge was made through a three step process. Beginning with a heating and mixing step, equimolar amounts of sucrose and dissolved polyvinyl alcohol (PVA) were mixed in a 4:1 ratio with $Fe(NO_3)_3$ in an aqueous solution. The metal nitrate formed nitric acid and the iron cation underwent hydrolysis in solution [15]. Additional nitric acid was added to ensure a pH of 3. These were mixed and heated to 115°C where oxidation of glucose, a monosaccharide with an O-glycosidic bond with fructose to form the polysaccharide sucrose, by nitric acid formed saccharic acid [113]. These may have further formed ester linkages with PVA to create the gelatinous resin. Secondly, this resin was placed into a vacuum oven to remove water and nitrogen compounds by heating to 125°C under vacuum. Finally an annealing step was performed inside a quartz tube furnace to promote nanoparticle nucleation and growth of graphite sheets at 1000°C and 4 torr while under a 1:1 volumetric flowrate of argon and hydrogen reducing atmosphere [15].

The resulting product was a porous carbon structure of α-Fe nanoparticles with a 10-20nm diameter enveloped by graphite sheets. To analyze the growth of these enveloped

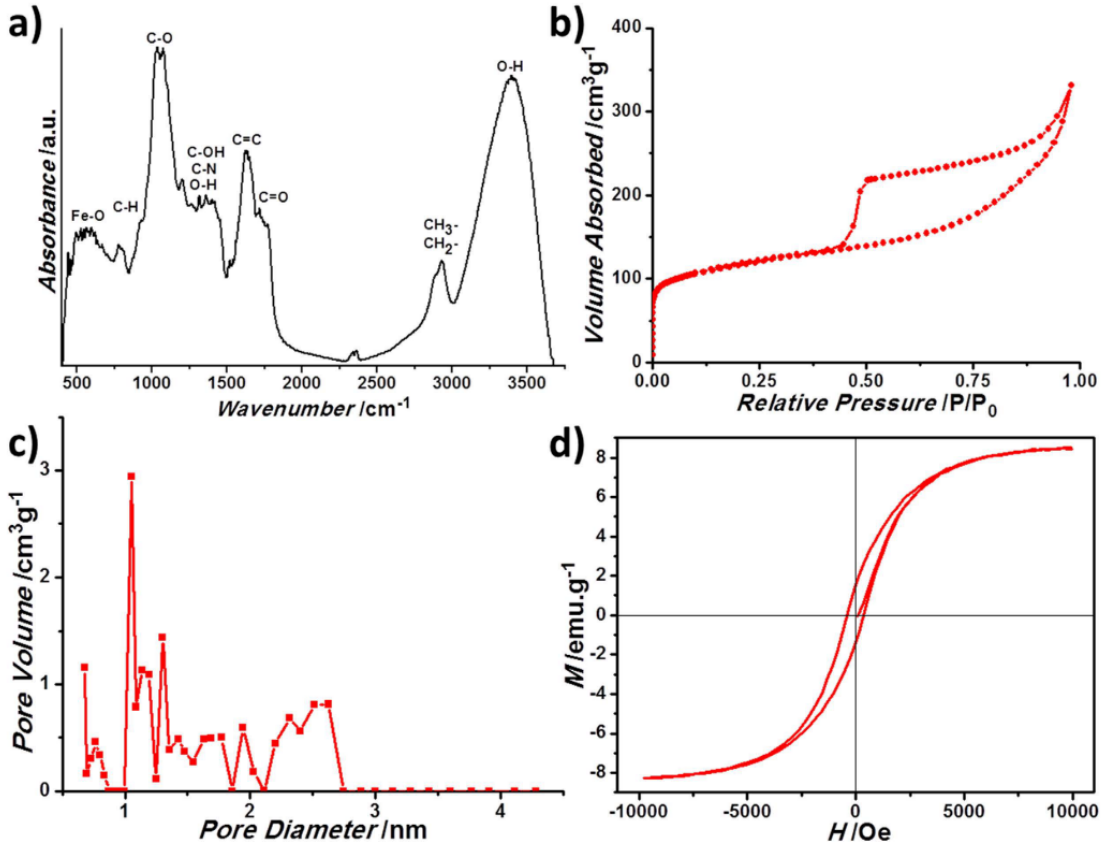

Figure 2.1: (a) FTIR spectrum of UtGS precursor after curing and before final heat treatment. (b) BET surface area measurement of UtGS with a combination of type I and type IV N2 sorption. (c) Pore size distribution of UtGS (calculated based on DFT model). (d) Magnetic hysteresis loop curve acquired from UtGS. Reproduced with permission from [15].

particles, an experiment was devised to inspect the growth at a series of temperatures with analysis by X-Ray Diffraction (XRD) to demonstrate the growth of a crystal structure. Temperatures included were: 500°C, 600°C, 700°C, 800°C, 900°C, and 1000°C as seen in Figure 2.2. At 500°C, no crystal phases were detected by XRD. However, at 600°C formation of α-Fe can be seen by a small (110) peak at the 45°Bragg angle. At 700°C, both graphite and α-Fe crystals have grown, shown by peaks at 27°and 45°, respectively. This suggests that at some temperature between 600°C and 700°C, graphite growth begins. At 800°C, Fe_3O_4 peaks are detected, suggesting at this temperature, oxidation of the nanoparticles is possible when outside of the furnace. At 900°C and 1000°C, the iron oxide peaks disappear, leaving only graphite and α-Fe peaks. The presence of C=O from carboxylic acids, esters, ketones, and aldehydes is noted by the Fourier Transform Infrared (FTIR) spectra in Figure 2.1 and leads the author and colleagues to believe esterification is the key component of polymerization, although the chemical mechanism described by Hamed et al is not believed to be accurate.

The use of Raman Spectroscopy corroborates the presence of graphite by showing the D band at 1350 cm^{-1}, G band at 1584 cm^{-1}, and the G' (2D) band at 2700 cm^{-1} [182, 56, 4] at 700°C and above. Transmission Electron Microscopy (TEM) micrographs of the enveloped particles show the interplanar spacing between graphite sheets to be accurate at 0.335nm as seen in Figure 2.3.

A goniometer was used to investigate the hydrophobic properties of the metal graphite sponge and a contact angle of 154.72°was measured; supporting the claim of superhydrophobicity. Oleophilicity was interrogated by high speed cameras and measurements

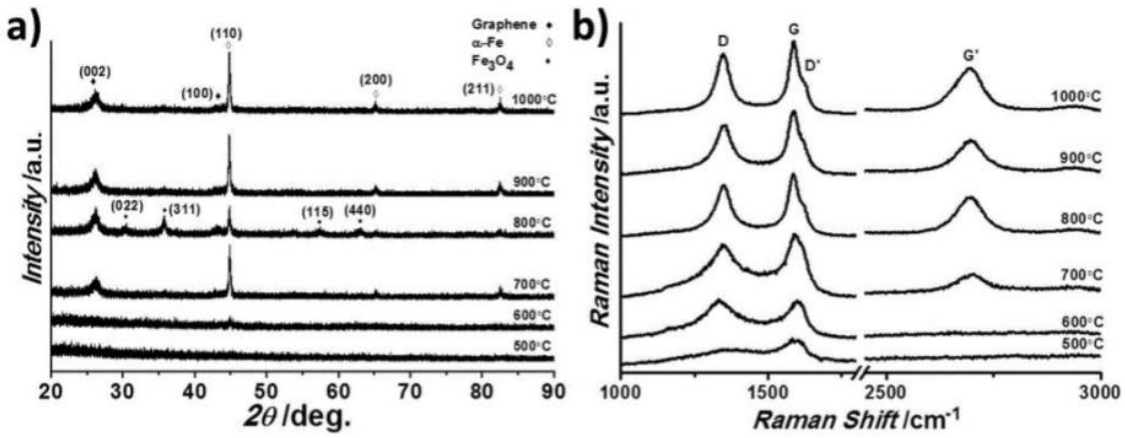

Figure 2.2: (a) XRD multiplot of UTGS heat treated at different temperatures. (b) Raman spectra multiplot of UTGS heat treated at different temperatures. Reproduced with permission from [15].

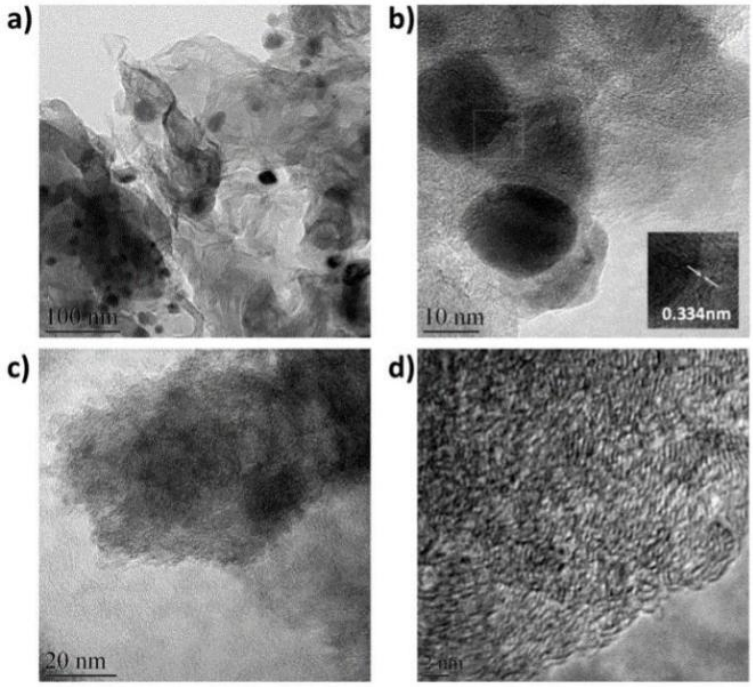

Figure 2.3: (a) Low magnification TEM image of UTGS (b) High magnification image of Fe nanoparticles encapsulated in graphene-based sheets (inset: HRTEM image showing the graphene layers with interplanar distance highlighted). (c) Low magnification image around the surface of the UTGS. (d) HRTEM image showing the microstructure of the surface of the UTGS. Reproduced with permission from [15].

of mass increase over time. Within 420ms, a 300mg drop of pump oil was sorbed into the sponge [15]. Paramagnetic properties were demonstrated with a Magnetic Hysteresis Curve showing a saturation magnetism and coercivity of 8.49emu g^{-1} and 336Oe at room temperature [15]. Hamed and company suggest single magnetic domains for each α-Fe nanoparticle considering the 10-20nm diameter of each particle.

2.2 Chemistry

The chemical mechanisms required to properly explain the growth of metal-carbon foams encompasses a wide range of disciplines. From hydrolysis of carbohydrates, metal salts, and nitrates, to oxidation and reduction of sugars and cations. A literature review is presented along with a series of control experiments which were performed in order to potentially verify the proposed mechanisms. The reader is highly recommended to review the literature, as key insights into the nature of the precursors and their behavior during hydrolysis, oxidation, and polymerization cannot be fully realized until well versed in the chemistry.

2.2.1 Hydrolysis

Sucrose is a heterooligosaccharide, meaning it produces an equimolar mixture of D-glucose and D-fructose upon hydrolysis. During mixing in aqueous solution, proton transfer between H_2O and the metal nitrate forms nitric acid, and at sufficiently low pH, can form NO_2[172], while the iron cation may undergo further hydrolysis reactions in solution[100, 120]. A review of carbohydrate chemistry suggests that when glucose is hydrolyzed, the

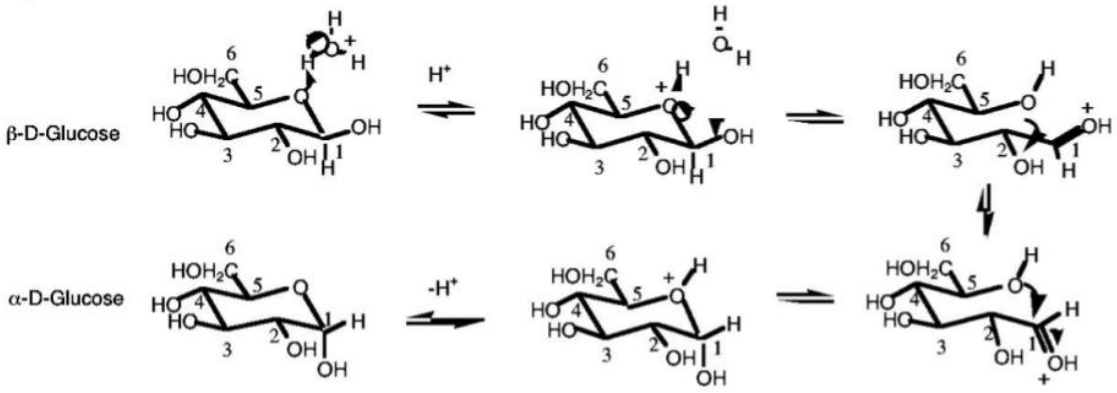

Figure 2.4: Muto rotation of glucose between the α and β orientation of the primary alcohol in aqueous condition. Reproduced from [120]

monosaccharide is free to mutarotate and isomerization between the α and β orientation of the primary alcohol produces a transitory acyclic glucose with the hemiacetal group forming an aldehyde at C1 and terminal alcohol at C6 [120] as seen in Figure 2.5. In aqueous solution, the C1 aldehyde group can undergo hydrolysis to form a geminal diol intermediate.

2.2.2 Ligands

Metal cations are known to form hydroxyl (-OH), oxo (=O), and aquo (OH_2) ligands upon hydrolysis depending on the pH of aqueous solutions [100]. These ligands also interact with carbohydrates in solution to form carboxylate ligands, but usually only at higher pH. Stable ligands with carbohydrates and alcoholic hydroxy groups can form with both the metal cation and the aquo ligands, of which the aquo ligands do form on metal cations at low pH, thus potentially opening up an opportunity for carbohydrate ligands to form. In particular, Fe(III) chelates to hexitols to a greater extent than Cu(II), Co(II), and Ni(II) [67] even at pH 2.5 and gluconic acid and galactonic acid is an especially stable

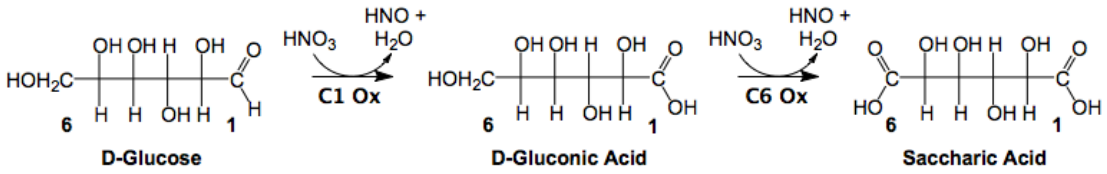

Figure 2.5: Oxidation of Glucose: Acyclic glucose in an acidic environment being oxidized to the gluconic acid intermediate, and further oxidized to saccharic acid, otherwise known as glucaric acid.

complex. Much can be learned about these complexes in literature [67, 5], although it is likely that the pH is too low for these types of ligands to be found in the aqueous environment of the carbon foam precursor solution. Still, these ligands could provide a method for metal cations to avoid reduction in solution and survive until annealing where reduction from H_2 gas can occur. On the other hand, these ligands may help in their reduction by reducing sugars like maltose, cellobiose, and lactose [5], either way, the possible metal cation-ligand complexes formed in solution should be studied further.

2.2.3 Oxidation

The oxidation of polysaccharides by nitric acid is well documented in literature[113, 120, 150, 5]. Once hydrolysis reactions cleave glycosidic oxygen linkages between monosaccharide sub units, oxidation by nitric acid is possible. Nitric acid could then form a protonated nitrate ester which then decomposes into a deprotonated nitrate ester and hydronium ion. Upon rearrangement, the nitrite ester produces a carboxylic acid at C1 and nitroxyl molecule (HNO)[172]. This is the gluconic acid structure which may or may not form lactones [5]. Next, HNO_2 can oxidize the C6 terminal alcohol in the gluconic acid by nucle-

ophilic attack at the nitrate forming another nitrate intermediate. This could decompose into a nitrite ester and produce a hydronium ion in aqueous solution. Rearrangement of the nitrite ester then produces a C6 aldehyde and nitroxyl molecule (HNO). Further oxidation of the C6 aldehyde by nitrate can proceed as discussed earlier, producing the saccharic or glucaric acid structure. The C1 aldehyde is more likely to oxidize before the C6 alcohol due to better electrophilic attraction. Simple esterification between saccharic acids polymerizes and produces the gelatinous resin and water as by product. The excess water generated from esterification is then a feedstock for the escaping gas bubbles which form the bulk structure of carbon foam in a process known as "gas-blowing".

Metal cations may also catalyze the oxidation of these sugars. For example, Cu(II) has been shown to oxidize D-galactose and D-galactonic acid at low pH [67, 138]. It is a common observation that the volumetric expansion of a carbon foam containing a metal nitrate precursor produces more volume than the polymerization of only a sugar or organic acid. An experimental study and literature review into the catalytic properties of metal cations in the oxidation of sugars and organic acids has not been undertaken, and the reader is highly suggested to do so.

Table 2.1: Successful Precursors to Polymerization

Polysaccharides	**Monosaccharides**	**Organic Acids**
Sucrose	Fructose	Gluconic Acid
Maltose	Galactose	Mucic Acid
Starch	Arabinose	Tartaric Acid
Lactose	Xylose	Malic Acid

A control experiment to confirm sugar oxidation was performed excluding metal cations and PVA and treated each of the following with nitric acid: sucrose, glucose, fruc-

tose, and gluconic acid. Each control was treated to pH 1, heated to the requisite 120°C, cured, and annealed per the procedure highlighted above. Each control produced a gelatinous resin which expanded upon curing. This provides evidence that PVA is not required for the polymerization of sugars, or the bulk morphology, and that the oxidized products can and do polymerize with each other. Still, gluconic acid and saccharic acid may form linkages with PVA by simple esterification between the carboxylic acid and alcohol groups respectively; experiments designed to elucidate this esterification mechanism were conducted using adipic acid. Adipic acid is a 6 carbon organic compound with terminating carboxylic acids but lacking alcohol groups. Experiments treating adipic acid with nitric acid to pH 1 did not result in gelled resins.

A brief table of successful precursors is shown in Table 2.1. Additional polysaccharides (lactose, maltose, starch), hexoses (galactose) and pentoses (xylose, arabinose) as well as mucic acid were successful as foam precursors, especially when metal cations are included. Less successful precursors included malic acid and tartaric acid, 4 carbon organic compounds with terminating carboxylic acids and including alcohol groups. These two precursors were observed to produce small amounts of gel, but did not exhibit volumetric expansion or porous networks. Differences in the availability of alcohol groups compared to hexoses and pentoses may contribute to lack of volumetric expansion during "gas-blowing" which depends partially upon the water byproduct generated from esterification. These experiments provide evidence that oxidation of saccharides leads to esterification with alcohol groups in other oxidized saccharides and possibly in PVA. All metal variations presented below use sucrose as the polysaccharide unless otherwise stated. For more information on

the polymerization and organic chemistry involved, the reader is referred to the work of Dr. Andrew J Patalano and his dissertation: "Thermal Processing, Strategies and Characterization of Sustainable Nanomaterials".

2.3 Bulk Morphology

By bulk morphology is meant the resultant interconnected carbon structure that foams as a result of "gas-blowing" during and after the polymerization of the oxidized polysaccharides. It can refer to the gelatinous-resin (gel-resin) macro-structure before or after it is annealed into a carbon foam. Previous work by Inagaki et al describes the nomenclature of carbon foams derived from tar pitches and the nomenclature is used in this work as well [77]. As seen in Figure 2.6, individual void space caused by escaping gases or other means are referred to as cells. The cell walls can by called ligaments and a ligament shared by two or more adjacent cells can be termed a joint or strut. Should two or more cells be connected by a pore, this is referred to as a connecting pore or "window".

2.3.1 Volumetric Expansion: "Gas Blowing" and Hydrogen Bonding

During curing, the gelatinous resin is placed inside a vacuum oven at 150°C. Water, nitrates, and NO_x compounds evaporate in this temperature and pressure range. Decreasing the pressure below atmospheric is not recommended immediately after hot plate synthesis. The polymer network is still fragile in this state and a vacuum is only recommended to be used after a few hours time has passed. Any hydrogen bonding the resulting polymeric network exhibits could constrict the volume of the resin. The loss of water vapor nullifies

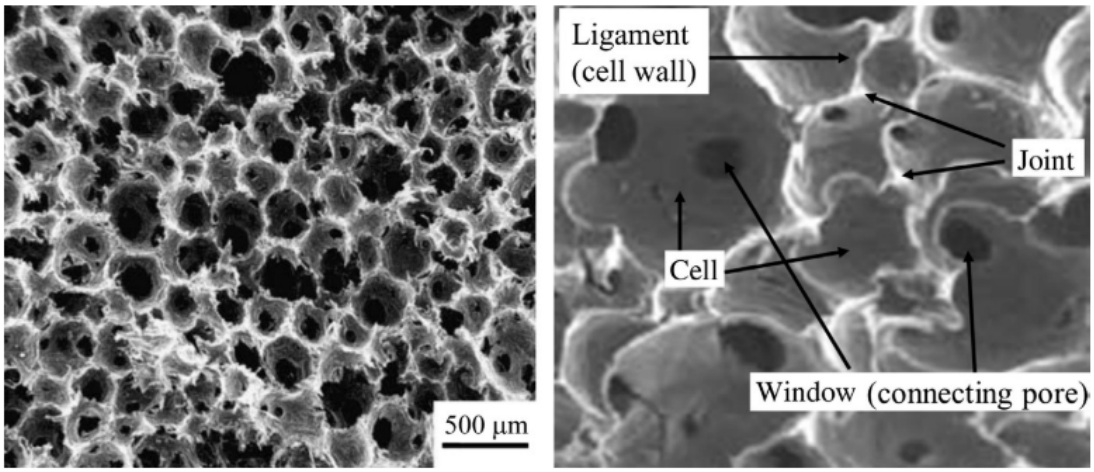

Figure 2.6: Nomenclature of carbon foams as discussed by Inagaki et al in Chapter 9 of "Advanced Materials Science and Engineering of Carbon" [77]

existing hydrogen bonds and thereby increases the volume of void spaces in the gelatinous resin. Gaseous nitrogen and carbon compounds escaping the polymeric network also leave behind void space that can increase surface area in a mechanism referred to as "gas-blowing" [163, 77]. Similar mechanisms are at play in carbon foams made from tar pitch, where increasing temperatures cause small bubbles to be released from decomposing gases; their coalescence with the neighboring bubbles form cells in the foam. One of the driving forces for the size of the cells is the surface tension of the molten pitch, or in the case of the sugar derived carbom foam, the polymeric gel-resin. As volumetric expansion occurs, shear stress forces the pitch molecules to orient their aromatic planes preferentially with the bubble wall. Oriented nanotexture is preserved in the ligaments and joints because of the viscosity of the partially decomposed pitch. This is observed in the sugar derived foams, even after annealing as seen in Figure 2.7 where a fractured cell ligament exposes the layered or lamellar sheets in the cell wall. Similar mechanisms of shear stress could be orienting

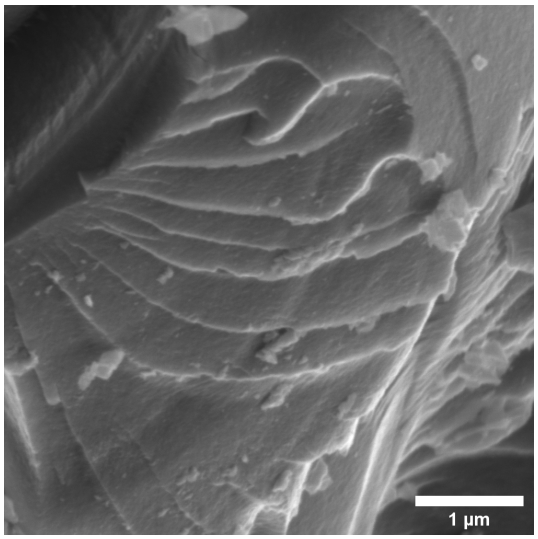

Figure 2.7: Typical fracture pattern of a joint or strut in the carbon foam after annealing

polymerized carbohydrates into a layered structure during volumetric expansion and set during annealing. Thus viscosity and surface tension of molten pitch are key factors of cell size and nanotexture of ligaments and joints; these same nanotextures could influence graphitization of the foam at high annealing temperatures (3000°C) [77].

This bulk structure is not stable in air until annealed which removes organics and forms an amorphous carbon substrate in which metal particles can be embedded if metal nitrate precursors are included. Before annealing is completed, the gel-resin is hygroscopic in nature, meaning it seeks to sorb water into it bulk structure. Should this occur, the gel-resin will begin to loose it's macro-structure and slowly collapse, forming a puddle of polymerized saccharides. Should this occur early in the synthesis, is it possible to perform the "gas-blowing" procedure once more by rehydrating the gel-resin with water and placing in 150°C oven at atmospheric pressure for approximately 4 hours.

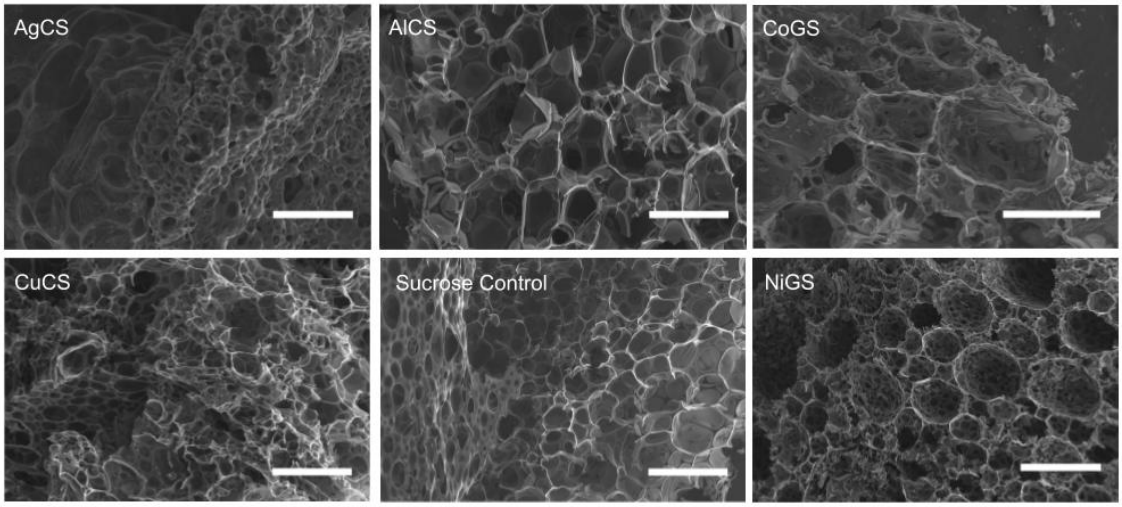

Figure 2.8: SEM Micrographs of each of the new sponge variants' porous macro-structures are depicted at 500μm including the sucrose control.

During annealing, it is possible the carbon foam experiences more volumetric expansion and merges with neighboring chunks of foam in the quartz crucible. Carbon activation procedures also note the loss of organics during the 400-600°C range which could also contribute to micro-porosity[108]. A comparison of the porous macro-structure for each of the MCFs is displayed in Figure 2.8. The bulk morphology is consistent between the metals chosen and structurally, the cells are of similar architecture; large outer "web-like" ligament structures with smaller, possibly mesoporous, cavities decorating the inner walls and connecting cells which is consistent with carbon foams in literature [77].

To explore the carbon bulk morphology as well as the cell void space and embedded metal particles, Microcomputed Tomography (micro-CT) was performed on the Ni-xylose variant and CTVox software was used to mark mid-density carbon in green and higher-density metals in red as seen in the 272μm x 176μm x 48μm section depicted in Figure 2.9. The bulk of the foam architecture is composed of carbon while metal particles are distributed

throughout the carbon structure. However, large concentrations of metals agglomerate at the joints and ligaments as seen in Figure 2.9c. This may be due to formation of the joints and ligaments during blowing. When in solution, the metal cations are thought to be mixed homogeneously, but as the polymerization takes place, bubbles form due to release of decomposition gases. The bubbles elongate the polymer-resin to create cell walls or ligaments as well as simultaneous contraction into joints, each of which are embedded with the metals, metal oxides, or metal salts. The concentration of the resultant polymer-resin into joints forces embedded metals into agglomeration at those areas during annealing.

Micro-CT was also performed on a Cu-lactose variant which is pictured in Figure 2.10. Using Amira software, a reconstruction of the foam using the micro-CT scan was segmented into 3 volumes of differing density: low-density volumes approximating the air and void space within the porous network as shown in Figure 2.10a, mid-density volumes showing a connected carbon network shown in Figure 2.10b, and high-density volumes approximating the metal particles as seen in Figure 2.10c. In the reconstruction, each colorized volume represents a volume which is not physically connected any other volume shown. For example: In Figure 2.10a, the light blue volume signifies a completely connected volume, which demonstrates that spaces within the pores and cells are connected and distinct from the green volumes depicted. In Figure 2.10b, the mid-density volume in dark blue displays the carbon structure as interconnected, with very little carbon separate from the main volume in dark blue. Figure 2.10c displays many separately colored high-density volumes, suggesting that metal particles are not highly interconnected and are instead dispersed throughout that foam's structure. The larger volumes in Figure 2.10c are not considered

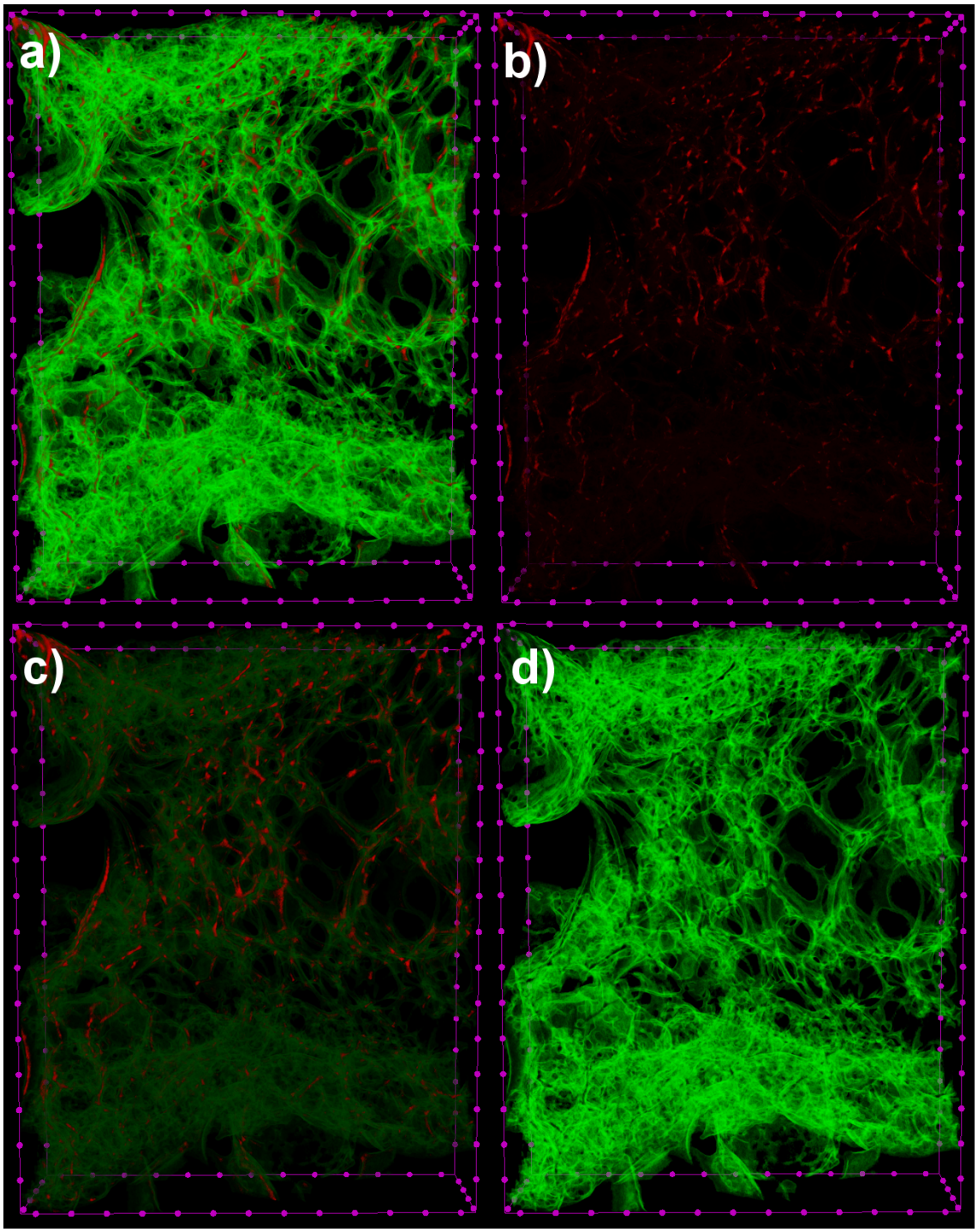

Figure 2.9: Micro-CT performed on the Nickel-Xylose foam variant which depicts a) both mid-density and high-density signal b) high-density signal showing metal particle distribution c) a combined mid-density and high-density signal with mid-density decreased to show overlay of red metal particle absorption d) mid-density carbon matrix. Each reference dot is spaced 16μm apart.

large particles. Due to the micro-CT's limits in resolution (0.351 μm voxel size), agglomerations of particles, as seen in the SEM micrograph Figure 2.10d, are detected as a single large volume. Volume fraction of each density segment was calculated to be: 73.68% low-density air and void space, 26.11% mid-density carbon, and 0.20% high-density copper metal. Assuming mid-density mass is carbon and high-density mass is copper, mass percentage was calculated to be 97.07% carbon and 2.92% copper. EDS of Cu-lactose sample records 85.58 mass% carbon, 10.76 mass% copper, and 3.68 mass% oxygen. Differences in the mass and weight between the two methods may be due to the limited resolution of micro-CT scans.

2.4 Growth of Metal Particles

The investigation into the literature to develop an origin of metal particles within the porous carbon foam is multifaceted and includes areas of study such as sol-gel synthesis, thermal-chemistry, and carbohydrate chemistry. Three methods are suggested for the growth of metal particles:

Method 1 - Sol-Gel During the mixing step, polysaccharide and metal nitrate precursors undergo hydrolysis reactions in aqueous solution. Metal cations are known to dissociate in aqueous environments and form aquo, hydroxyl, and oxo ligands depending on the pH of the solution. Solvation leads to the formation of partially covalent bonds in transition metal ions. "A partial charge transfer occurs from the filled 3a bonding orbital of the water molecule to the empty d orbitals of the transition metal ion. The positive partial charge on the hydrogen atoms then increases and the water molecule, as a whole, becomes more

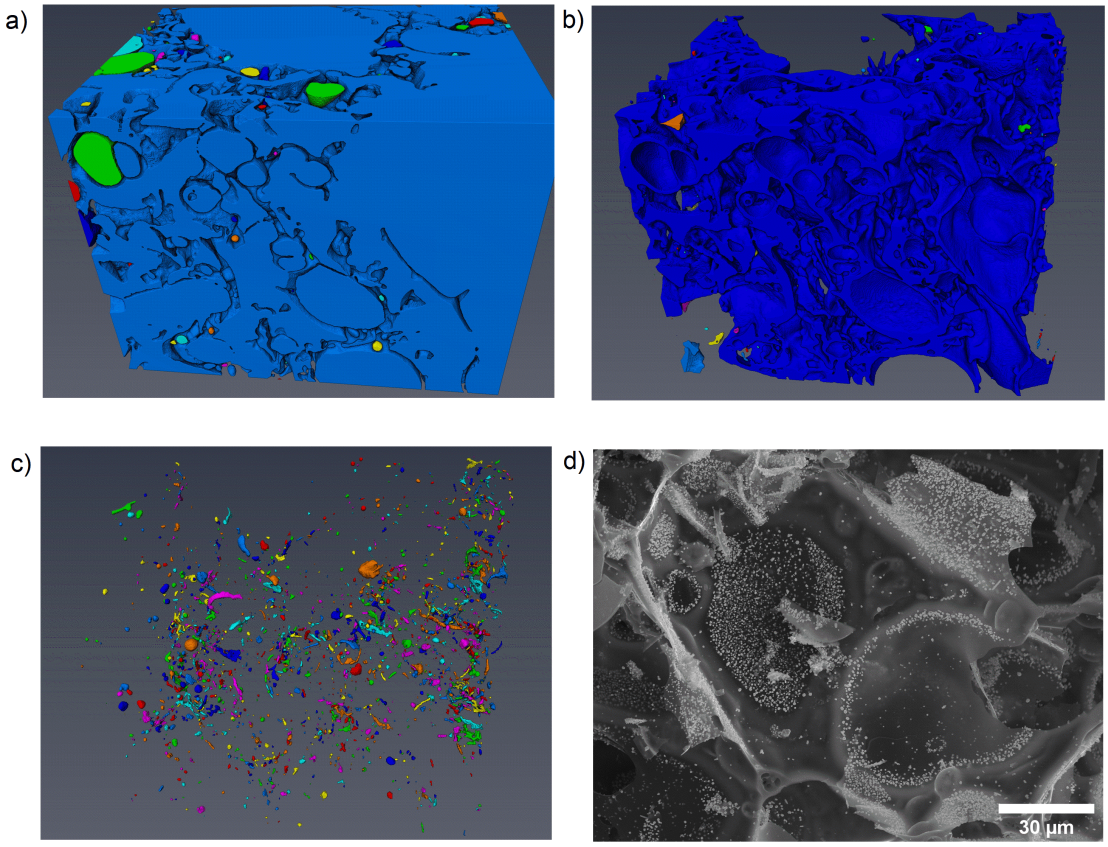

Figure 2.10: Micro-CT performed on the Cu-lactose variant where each color signifies a volume that is not physically connected to any other volume. Reconstruction of Cu-lactose foam depicts a) volumes of low-density air and void space b) volumes of mid-density showing porous carbon structures c) high-density signal displaying volumes of metal particles d) SEM micrograph of Cu-lactose showing agglomerations of particles lining the struts, joints, and cell walls.

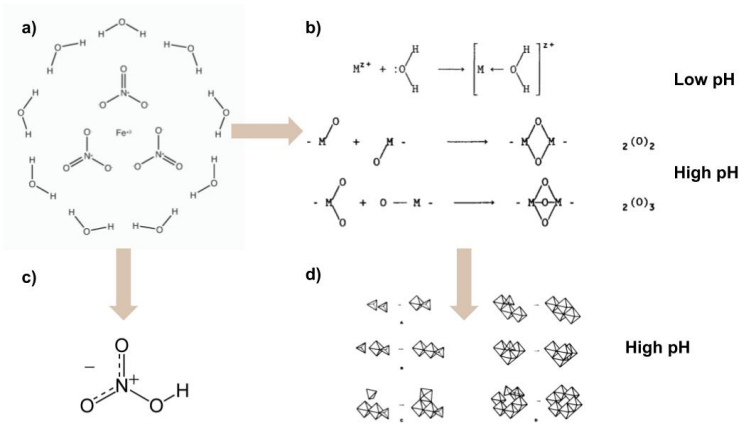

Figure 2.11: Depiction of hydrolysis products of metal nitrates: a) the structure Fe nitrate b) possible metal-oxygen bonds depending on pH c) nitric acid and d) tetrahedral and octahedral metal oxide structures [100]

acidic" [100]. At lower pH, aquo ligands (OH_2) are favored, at mid pH hydroxyl (OH^{-1}) ligands are favored, and at high pH oxo (=O) ligands can form. As seen in Figure 2.11, these metal-ligands can then precipitate metal oxides in solution upon heating or increasing pH [100]. Nitrates and nitrites are present in solution during the mixing and oxidation of glucose, which may be catalyzed by the presence of metal cations, though further studies are needed to confirm.

Method 2 - Decomposition of Metal Nitrates After curing at 150°C under vacuum nitrate groups may still be present in the gelatinous resin. During annealing it is possible that metal nitrate compounds form metal oxides as well [118, 24], but in small, amorphous quantities that are not detectable by XRD; no crystallinity was detected in our characterization of the gelatinous resin.

Metal oxides produced by Methods 1 and 2 are assumed to be present in the resin before entering the annealing furnace. While exposing gelatinous resin to a reducing

environment, H_2 gas removes oxygen through reduction, leaving reduced metal atoms that may nucleate into particles. However, the mixing of precursors in this study occurs at low pH, and the cations are therefore less prone to oxo ligand formation and metal oxide particles as in Method 1. Furthermore, a control experiment performed without the flow of H_2 gas, eliminating a reducing atmosphere, during the annealing step showed no presence of metal oxides detected by XRD for Fe carbon sponge.

Method 3 - Reduction by Carbohydrates The final suggested method of metal particle growth is the reduction of metal cations by the sugars themselves. Silver and cupric ions are mild oxidants that oxidize reducing sugars like maltose, cellobiose, and lactose[120, 124, 125, 114, 5]. This would allow elemental metal atoms to nucleate into colloids during the mixing step and grow during the annealing step into crystalline particles and may also take in place in Fe, Co, Ni, and Al variations of the carbon sponges. These metal cations do form chelate complexes with dissolved sugars [67] which may help in the reduction of the ion.

These mechanisms represent three possible routes by which metal cations are reduced to elemental metal atoms whereby they are embedded within the porous carbon matrix. For nucleation of clusters, particles, and grains solidification theory is needed.

Particle Solidification Theory Solidification occurs when the solid phase of a material has lower Gibbs Free Energy compared to its liquid phase at a certain temperature and composition. Between the solid particles and the liquid lies a interface which has greater energy than either of the two because of the need to accommodate slight structural changes

on both sides. Particles in liquid solution lower their energy by making a volume, but simultaneously gain energy because of the interfacial surface. At large radii, the volume component of the energy dominates and at small radii surface area contributions dominate the overall free energy of the particle. In homogeneous nucleation any atom can be a nucleation site, and a small cluster of atoms appear in a melt or liquid due to random fluctuations between the energy of the clusters and the melt. Clusters below a certain critical radius called embryos melt back into solution; clusters above this critical radius survive to become nuclei and grow in volume. The nucleation rate of the growing particle depends on two factors: the energy barrier of nucleation and atomic mobility, each of which depends strongly on the temperature. However in practice, the predictions made by homogeneous nucleation are not observed in experimentation [35].

In heterogeneous nucleation, solidification is initiated on a foreign surface, such as a mold, an oxide skin, or a foreign particle. This is the case for the metal particles in a carbon foam. Foreign particles have a nucleation potency (a certain thermodynamic potential to form clusters) as well as a temperature above which where no nucleation takes place and below which almost instantaneous nucleation transpires. As the temperature falls, the cluster experiences undercooling, is exposed to temperatures below its freezing temperature, and once the characteristic nucleation temperature of a foreign particle is reached, solidification begins where latent heat is liberated and where there may be an increase the temperature of the cluster, but heat content decreases overall. When interfacial energy between the foreign solid and interface is energetically favorable, the solid layer will completely cover the substrate, cutting off the liquid from the substrate. When the

interfacial energy between the liquid and the interface is favorable, the solid will not form. Assuming a hemispherical nuclei on a substrate - the wetting angle or contact angle of a nucleating particle on a substrate plays a part in lowering the number of atoms (and thus the nucleation energy barrier) required to form a critical nucleus. In heterogeneous nucleation, the rate of nucleation depends on the amount of foreign substrates and whenever easily wetted foreign particles are present in the melt, they induce heterogeneous nucleation under normal cooling conditions. As the required undercooling is reached, the number of nuclei is immediately increased from zero to saturation of all foreign particles. In practice, there are a distribution of nucleating foreign particles of varying potency. Pores or cavities can also lower the nucleation energy barrier for nuclei to form, of which the carbon foam has many, although nucleation will not proceed unless the particle is undercooled. Moreover, the morphology of the cavity completely dictates the temperature and undercooling at which stable embryo will grow out of it [35]. The temperatures applied during annealing and CVD synthesis are well below the freezing temperatures of the Co, Fe, Ni, Ag, and Cu. However, Al and Zn variants of the carbon foams have much lower melting points and potential for particle nucleation experiments may be considerable. Additionally, morphology of the Cu particles has been noted to be spherical in Cu-glucose foams where as they are more anisotropic in Cu-lactose foams. Differences in porosity may arise due to different sugar precursors and may affect particle morphologies. Much can be studied with regard to particle nucleation on the bulk structure of carbon foams. Form more material on the subject of particle nucleation, the reader is directed to “Solidificaiton” by Dantzig and Rappaz[35].

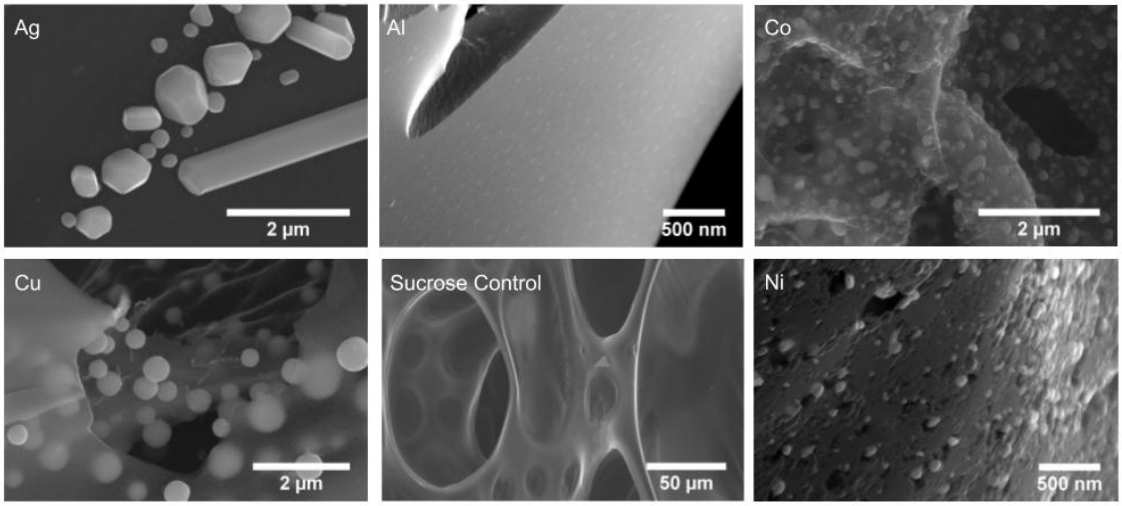

Figure 2.12: Comparison of particles generated from respective metal nitrates chosen. Sucrose control sample did not exhibit any metal particles.

2.4.1 Characterization of Metal Particles

Figure 2.12 shows the relative size of the particles grown from the metal nitrates chosen. Cu and Ag particles are on the order of 1-2 microns in size while also generating rods. Much like Fe, Ni and Co generated nanosized particles in the range of 50-200nm. The inset in a) of Figure 2.17 shows a STEM micrograph of a Co nanoparticle approximately 60nm in diameter surrounded by graphitic carbon structures. Approximate size of Co nanoparticles was determined to be 58nm in diameter by Scherrer analysis of the Full Width Half Max calculated from XRD plots of Figure 2.16 which is in agreement with the results from the STEM micrographs in Figure 2.17. Al nitrate also produced smaller sized particles, below 100nm. Elemental mapping was performed using EDS to show that the distribution of metal within the porous bulk structure is consistent as seen in Figure 2.13.

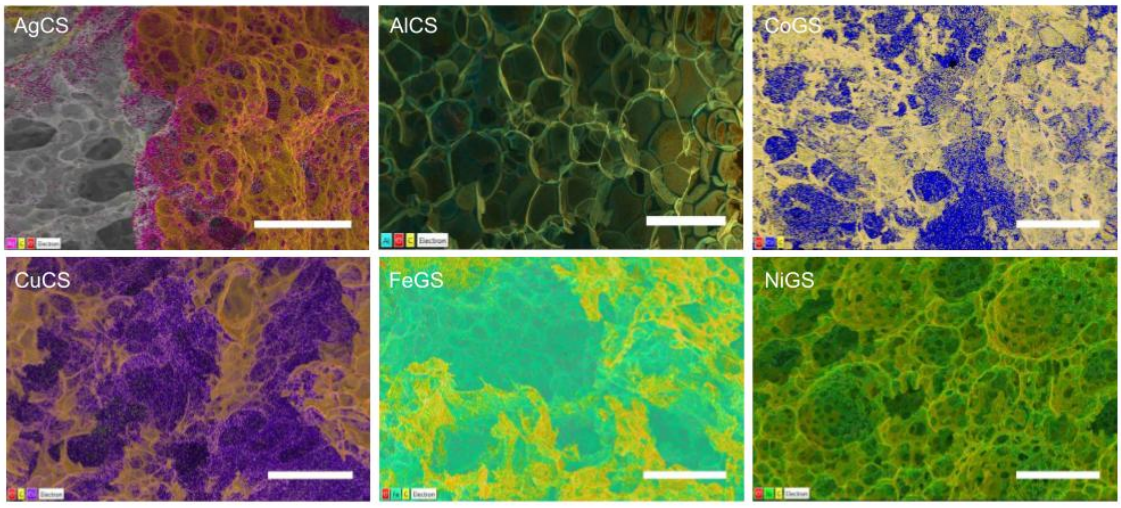

Figure 2.13: EDS Mapping of porous structures at 500μm shows the distribution of embedded metal particles synthesized from the corresponding metal nitrate precursor. A partial map of the AgCF was acquired due to the depth of field of the structure.

Particle size analysis was conducted on the Cu-lactose micro-CT sample from Figure 2.10c by two software methods, Amira and ImageJ, and compared. ImageJ was used to threshold the SEM micrograph from Figure 2.14a to produce Figure 2.14b. Particles with circularity >0.7 were counted and diameters calculated producing the histogram in Figure 2.15a. No particles with diameter >0.9μm were observed using ImageJ. We use this diameter as the upper limit of diameters calculated by Amira. Because of the resolution limitation (0.351μm voxel size), volumes calculated from Amira included large agglomerations like those seen in Figure 2.10d. Therefore, the 0.9μm limit observed by ImageJ was used to produce the histogram in Figure 2.15b. Box plots are shown to demonstrate the sample distribution in Figure 2.15c and the SEM micrograph in Figure 2.15d also agree with results found from ImageJ and Amira.

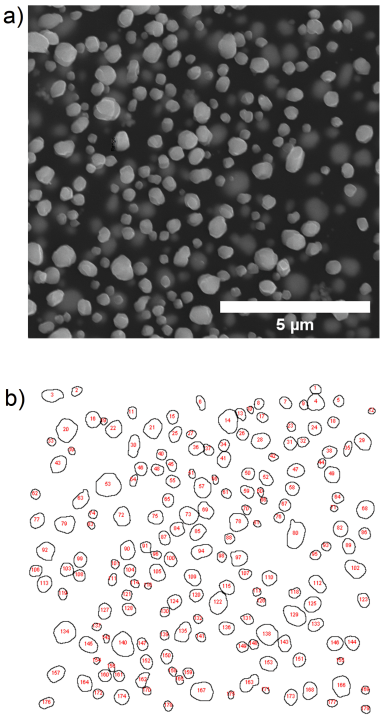

Figure 2.14:

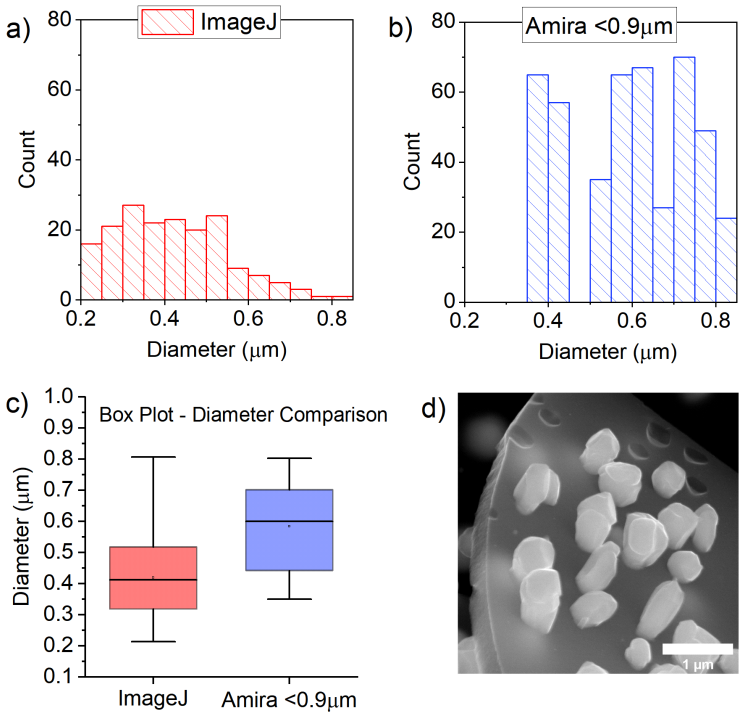

Figure 2.15: Comparison of particle size from Cu-lactose sample by Amira and ImageJ

Crystallinity of Metal Particles Ferrite α-Fe particles were shown to be grown at 600°C in XRD results from Hamed et al. Observations from iron-carbon phase diagrams [9] show that α-Fe (bcc) is stable below 740°C, and above which γ-Fe (fcc), Fe_3C, liquid iron and crystalline carbon (graphite) are stable at concentrations of carbon above 4.2%. "Ferritic iron undergoes a magnetic phase transition at 771 °C between the low-temperature ferro-magnetic state and the higher-temperature para-magnetic state" [9]. The MCFs display magnetic properties when annealed at 800°C and above.

When XRD analysis was conducted graphite was found only in the Ni and Co sponges as seen in Figure 2.16, which clearly notes the presence of the 27°diffraction peak for graphite producing a Metal Graphite Foam (MGF). This is also corroborated with Raman Spectra in Figure 2.19 and Electron Energy Loss Spectroscopy (EELS) in Figure 2.17. Cu, Ag, and Al did not grow graphite sheets, instead forming metal carbon sponges. Due to this distinction, the resulting materials will be referred to as follows: FeGF, CoGF, NiGF, and CuCF, AgCF, AlCF respectively. The XRD reflections for each respective metal particles were detected: XRD spectra of FeGF displayed both α-Fe and γ-Fe particles and possibly Fe_3C. NiGF and CoGF spectra displayed γ-Ni and γ-Co peaks respectively. CuCF, AgCF, and AlCF each displayed FCC reflections. AgCF also detected a small BCC peak. Nitric acid and sugar controls did not produce graphitic peaks during XRD analysis suggesting that metals are requisite to their growth, but only certain transition metals and localized around those same metal particles as seen in the inset of Figure 2.17.

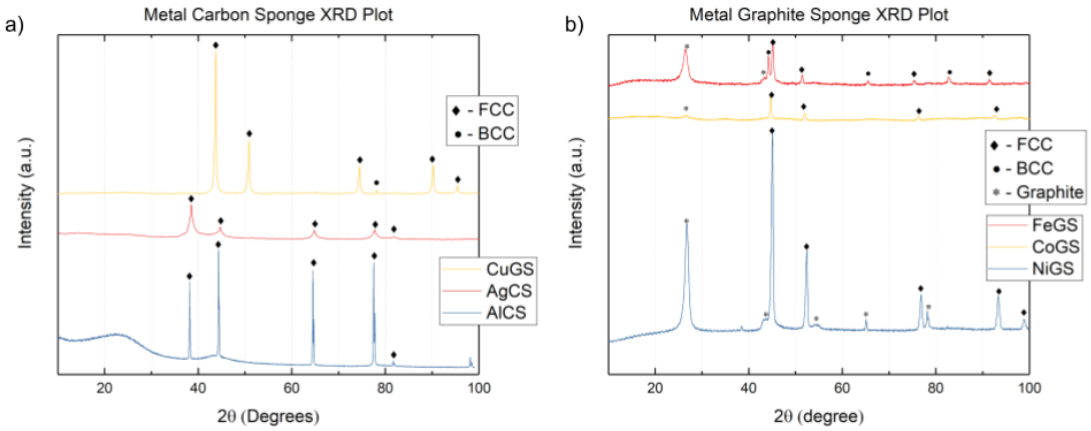

Figure 2.16: XRD Comparison: XRD Spectra showing the presence of a) crystalline Cu, Ag, and Al particles and b) crystalline Fe, Ni, and Co particles as well as graphite.

2.5 Mechanism of Graphite Encapsulation

A difference in the XRD spectra denoting that presence of graphite in some carbon foams but not in others warrants an investigation into discerning the root causes of the growth. Below is an analysis of the carbon solubility and its affect on the growth of encapsulating graphite layers in the metals used to synthesize new carbon foams.

2.5.1 Insights from CNT Synthesis

Given the nature of the constituents and temperature at which the metal carbon sponges are annealed, comparisons can be made to the growth mechanism of Carbon Nanotubes (CNTs) using catalytic metal nanoparticles, usually Fe, Ni, and Co, by Chemical Vapor Deposition (CVD). The growth of CNTs can be accomplished by CVD synthesis, which is processed at a similar temperature range (625°C-900°C), and flow of carbon feedstock gases such as ethylene[180] or methane[72]. There are several differences however;

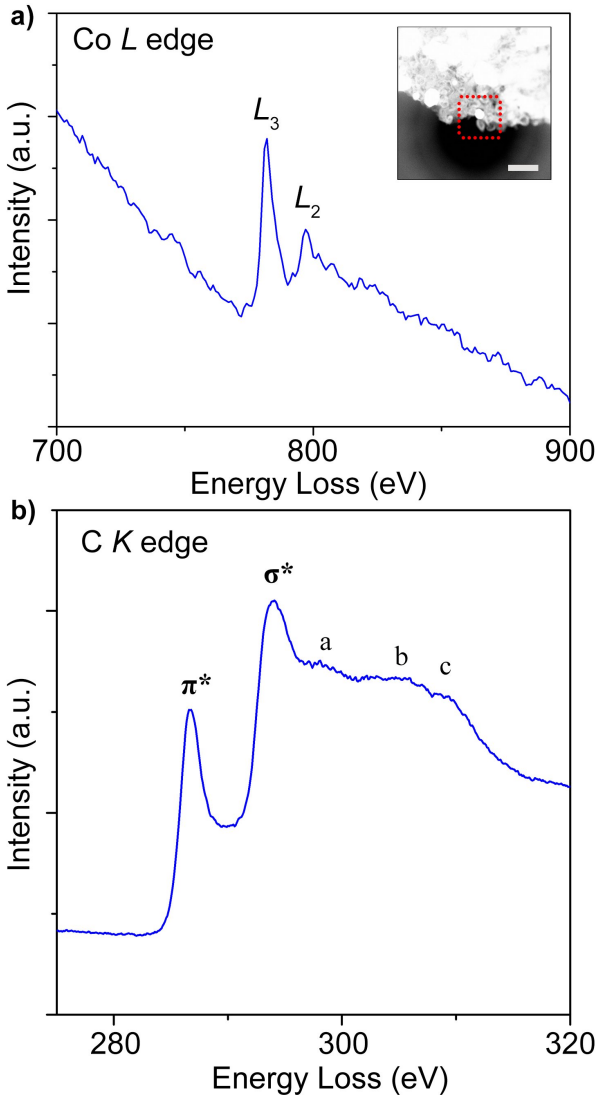

Figure 2.17: a) EELS cobalt L_{23} edge measured in the region highlighted by the dotted box in the inset STEM micrograph. The STEM micrograph is acquired from a sample of CoGF and shows a Co nanoparticle surrounded by graphitic structures. Scale bar is 200 nm. b) EELS carbon K edge with characteristics peaks denoted. Fine structure peaks a, b, and c are consistent with EELS of graphitic carbon [7]

during the annealing process orders of magnitude more carbon is present as a gelatinous resin. Additionally, catalytic metal particles are already present at the start of CVD synthesis; during the annealing of the MCF the metal particles nucleate and grow from the metal atoms or oxides present in the resin, though there are CVD methods that form particles in situ from precursors such as ferrocene [139, 36, 72]. Even with these differences, many crystal growth processes and temperatures agree with the XRD data [15].

Fe, Co, and Ni are common catalysts for CNT growth because of their ability to decompose carbon feedstocks (acetylene, ethylene, methane, soot, etc) [41, 36]. "Unlike Ni and Co, a range of different (meta)stable crystalline carbide phases have been reported for Fe upon exposure to carbonaceous precursors at elevated temperatures"[170]. In fact, Fe_3C (cementite) particles have been used as catalytic particles for CNT growth; however these may only be a subset of more complex kinetics within the phase separation process which leads to CNT growth as shown by Wirth et al[170]. Wirth and company used in situ XRD, X-Ray Reflectivity (XRR), and Environmental TEM (ETEM) to show that these iron carbide reflections were not detected during the growth of CNTs at 750°C. Instead both α-Fe and γ-Fe phases as well as graphite are detected, implying that particles of each iron phase coexist [170] and that carbon present in the carbide is dissolved into the metal particles and undergoes phase separation, precipitating the growth of a CNT. Fe_3C reflections were detected in another experiment which also produced CNTs, but the observation of CNTs grown by α-Fe and γ-Fe suggests that cementite is not a prerequisite for growth.

Metal-Carbon Phase Diagrams and Phase Separations

In any case, the particle catalyzing the eutectoid reaction is crystalline. "This is due to eutectic compound formation, and an increase in carbon content in the liquid [iron] phase causes the phase separation between graphite and the metal. This explains why the transition metals act as catalysts for nanotube growth. Fe, Co, and Ni have a phase diagram containing a eutectic compound with carbon, and the eutectic points are 1148, 1321, and 1327 °C, respectively. But because of the size effect, the eutectic point of these metal-carbon phases are reduced to 700-800 °C for nanosize particles" [72]. The low Gibbs free energy of eutectic compound phases allows the dissolution of carbon feedstock into the metal particle, however the increase in carbon content due to the dissolution (or supersaturation) shifts the phase diagram to the right, to the point where graphite precipitates out of solution as seen in Figure 2.18. However, in CVD growth the carbon feedstock (acetylene, methane) is in such low concentration that CNTs form instead of graphite layers and it is only at the end of CNT growth that graphitic encapsulation is observed. During growth of the MGF, carbon is present in excess, suggesting graphite a much more likely precipitate than CNTs.

Graphite vs no Graphite

C. Deck et al investigated some 13 potential metal catalysts. Only Fe, Ni, and Co produced CNTs and went on to investigate the phase equilibria for each metal-carbon system. "Unsuccessful catalysts typically fell into two categories: either there is no significant solubility of carbon in the metal or numerous stable carbides formed at higher carbon concentrations. In the carbon-copper, carbon-zinc, carbon-gadolinium, and carbon-cadmium

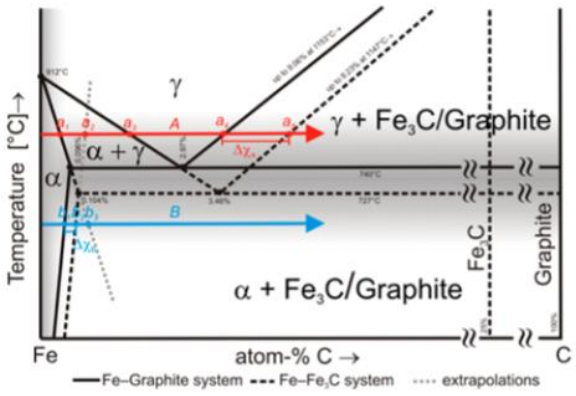

Figure 2.18: Schematic phase diagram of the Fe-graphite (solid black) and metastable Fe-Fe_3C (dashed black) systems (not to scale). Adapted from refs [43] and [9]. Linearly extrapolated phase boundaries are in dashed gray. Reproduced from [170]

systems studied, the solubility limit of carbon in the metals is extremely low"[36]. Since no carbides were detected by XRD as seen in Figure 2.16, the limited solubility of carbon in the Cu, Ag, and Al solid phases may prevent the accumulation of carbon in the particles and further prevents the nucleation of graphite in the MGFs.

Agreement with CNT Modeling

Molecular Dynamics (MD) has been used to model the phase separation mechanism and predict the temperatures at which CNTs grow. Feng et al performed MD simulations while calculating the Lindemann index of each iron and carbon atom to predict carbon dissolution and CNT formation at temperatures[55] that are in agreement with what is depicted by the XRD data for MGF [15]. By calculating the Lindemann index, a measure of thermally driven disorder, a phase change can be predicted based on the distance between atoms. Crystals melt when the average amplitude of thermal vibrations of atoms is relatively high compared to interatomic distances.

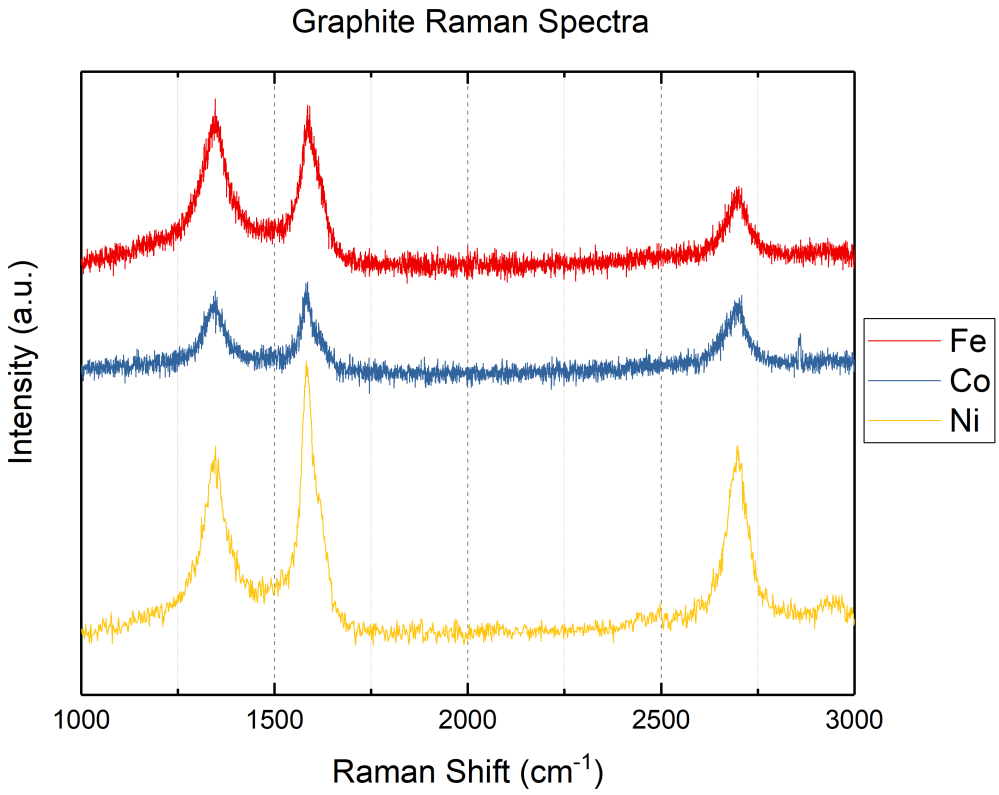

Figure 2.19: Raman Comparison: Raman Spectra confirming the presence of graphite encapsulating layers in FeGF, NiGF, and CoGF.

For example: metallic atoms would be further apart in a liquid than in a solid so the interatomic distance can be used to determine if a catalytic metal particle is a crystalline solid or undergoing a phase change to liquid. Feng and associates modeled a 300 atom Fe cluster along with separate simulations with the addition of 30 C atoms and 60 C atoms. At 627°C, C atoms in the simulation form C strands (several C atoms in a row, bonded in a string-like fashion) on and just beneath the surface of the Fe cluster. These C strands begin to combine and nucleate graphitic islands. Graphitic islands then grow in size and at 627°C, the kinetic energy is enough to overcome the attraction between the island and the cluster, permitting the islands to phase separate and form a CNT cap[55] and growth of the tube proceeds. The XRD data displays α-Fe peaks at 600°C and at 700°C graphite peaks are observed, meaning that at some point between 600°C and 700°C, graphite encapsulation begins [15]. This is in agreement with the results presented in Feng et al.

The main difference in solid and liquid clusters is the diffusion path of carbon toward the CNT cap. The distance between Fe atoms and the center of mass of the cluster shows that at 627°C, the cluster behaves more like a solid and carbon atoms stay at the surface. At 927°C the interatomic distance of the Fe atoms is greater and the cluster behaves more like a liquid. This may indicate that at higher temperatures, carbons atoms can penetrate deeper into the particle before uptake into the growing CNT[55]. The surface Fe atoms of the particle behave much like a liquid due to their rapid mobility at this temperature, lending credibility to the suggestion that a size effect lowers the temperatures at which eutectic compound phases exist. At 727–827°C, Feng et al observe the transition from solid clusters to liquid in their MD simulations.

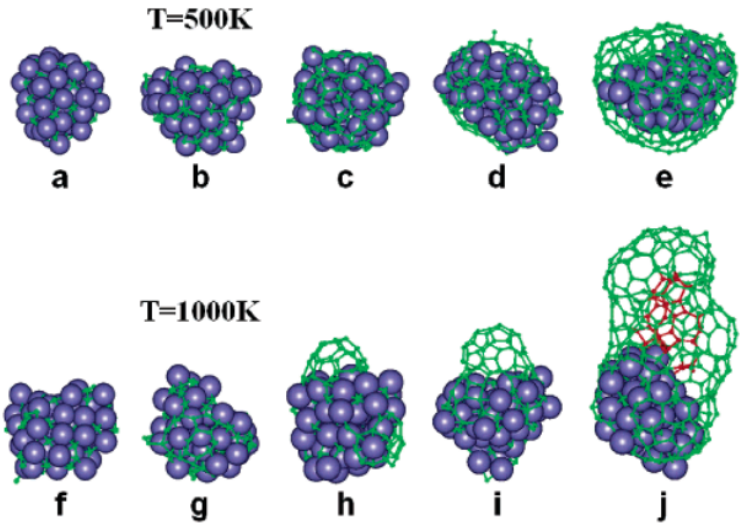

Figure 2.20: Snapshots from typical MD simulations of iron-catalyzed formation of carbon species at 500 K (a-e) and 1000 K (f-j). At low temperatures (<700 K), the particle is encapsulated by a graphitic layer whereas SWNTs are nucleated at intermediate temperatures (between 800 and 1400 K). Carbon atoms are shown as ball-and-stick and Fe as large spheres. Carbon atoms (defects) that occur on the inside of the SWNT are shown in red (j). Reproduced from [42]

The CVD growth of CNTs on Fe and Co particles by methane also indicate that a carbon-metal "liquid" particle is formed. Experiments at 800°C and 900°C with 30-100nm diameter particles demonstrated the growth of CNTs. Homma and company also measured the melting points for the nanosized particles indicating that the eutectic point of the bulk material was 390°C and 174°C lower than the melting point of Fe and Co respectively. The surface to volume ratio can affect the melting point and in nanosized particles the size effect reduces the eutectic point to 700°C – 800°C [72]. The drop of these melting points is evidence of the formation of eutectic compounds with carbon[72].

Metal–carbon adhesion is also necessary to sustain the growth of CNTs. Should the CNT separate from the particle, the instability of dangling carbon bonds leads to the closure of a CNT cap[41]. The strong bonding between carbon and Fe, Co, or Ni in

these eutectic phases give them large positive enthalpies that hinder the end cap formation, sustaining the growth of a CNT, but increasing the number of carbon-metal bonds lowers the energy of the system[41]. At some point during annealing of the gelatinous resin the graphite growth ends; this could be a point at which carbon has supersaturated the particle and lowered the enthalpy enough to end the phase separation.

Graphite Encapsulation of Metal-Particle

In CVD growth the carbon feedstock (acetylene, methane) is in such low concentration that CNTs form and it is only at the end of CNT growth that graphitic encapsulation is observed. During the annealing step, gelatinous carbon feedstock is present in excess throughout the growth of metal particles (600°C) and graphite phase separation (700°C) as verified by XRD [15]. This excess carbon present at the 600°C-700°C range may prematurely catalyze graphite formation as metal particles are growing, encapsulating the particle and thus restricting it's growth and size. This may explain why the metals commonly used in CNT synthesis (Fe, Ni, Co) typically display smaller particles sizes than those that do not (Ag, Cu) as seen in Figure 2.17 and Figure 2.12 respectively, Al being the exception. The presence of excess carbon may also prevent CNT synthesis simply due to limited space within the gelatinous matrix suggesting graphite is more likely to precipitate.

After CNT production, catalyst metal particles (Fe, Co, Ni) encapsulated in graphitic layers have been observed and "it is clear that encapsulation prevents the catalytic decomposition of carbon feedstock and hence poisons all active particles"[42]. Furthermore, MD simulations predict the encapsulation of metal catalyst particles by graphitic layers at low temperatures (625°C) [42]. When at 527°C, there is not sufficient kinetic energy to

overcome the metal-carbon adhesion strength for carbon strings to lift and form CNT caps. Instead, the carbons strings or islands remain on the surface and envelop the particles[42]. At 727°C, MD simulations predict that kinetic energy is now sufficient to form CNT caps. In contrast to the XRD spectra in Figure 2.2, α-Fe particles are not detected until 600°C, and at that temperature, no graphite has been grown yet. Feng and associates do suggest that the transition from CNT growth to particle encapsulation occurs as the particle size and melting point increases. At 600°C, α-Fe particles growing in the MGF resin may not be large enough to begin encapsulation.

The encapsulation of these particles might begin with the formation of a single layer, and each successive layer is formed between this initial sheet and the catalyst particle as seen in Figure 2.21. Phase separation of carbon atoms already supersaturated in the particles supplies the carbon feedstock for additional graphite layers as suggested by the purity of the metal particle and the observation of iron-carbide particles without encapsulating graphitic layers[42]. This agrees with TEM micrographs as seen in Figure 2.3 which display particles encapsulated by a few layers of graphite before terminating into amorphous carbon regions [15]. These particles "that are encapsulated in graphitic layers are also important magnetic materials which, due to their unique magnetic properties and high physical and chemical stability, have potential applications in high-density magnetic recording media"[42] and further research has been performed to control the size of the particles as well as the thickness of their encapsulation layer[139]. These are also known as carbon nanocapsules (CNCs) and amorphous carbon is often observed on the outer surface of these graphitic layers [42]. Methods such as arc discharge, laser ablation, plasma-enhanced CVD,

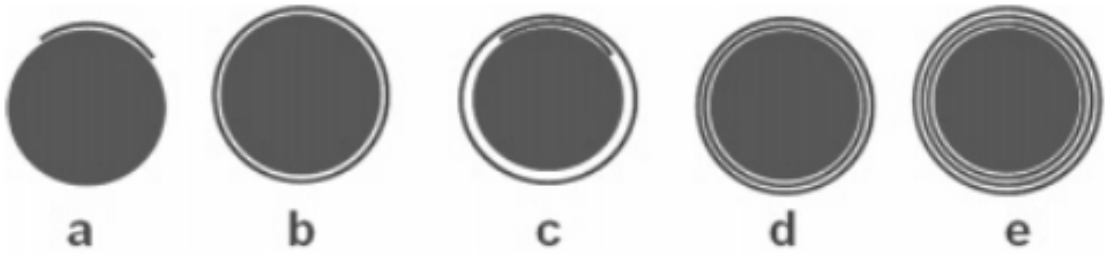

Figure 2.21: Illustration of the layer-by-layer encapsulation mechanism of catalyst particles. Atoms in the outer layers (a and b) may arise directly from carbon feedstock decomposition near the edge of the growing layer or from the precipitation of atoms in the metal-carbide particle, whereas atoms in the inner layers (c-e) originate from the metal-carbide. Reproduced from [42]

and thermal pyrolysis have been employed to synthesize these CNCs. Though the initial aim of Hamed et al was to synthesize a hydrophobic, oleophilic carbon sponge, what was also achieved was the production of CNCs by simple oxidation of polysaccharides by metal nitrate compounds followed by annealing in a reducing atmosphere. The MGF is a porous carbon matrix embedded with CNCs.

Chapter 3

Carbon Foams as substrates for the Growth of Carbon Nanotubes and Graphene

Here we present a method of growing CNTs on carbon foams via embedded metal particles and further widening their potential applications for selective oil sorption and electrochemical energy storage. Insight gained from the literature review in Chapter 2 forms the theoretical basis for the assumptions and methods used in formation of metal nanoparticles for catalytic growth of CNTs on carbon foam substrates. This chapter will present a review of synthesis techniques for CNT synthesis, catalysts with sufficient carbon solubility, and a review of Raman spectroscopy for common carbon allotropes. Afterward a study of the growth and characterization of Multi-Walled CNTs and Multi-Layer Graphene on carbon foams is presented with an emphasis on the use of Ni and Co embedded carbon

foams and the comparison of the different carbon morphologies resulting from Ni's and Co's differing carbon solubility. The knowledge gained from this project lead to the refinement of CNT carbon foams for the applications reviewed in Chapter 4 and 5.

3.1 Carbon Nanotubes and Graphene

Carbon nanotubes and graphene share many attributes because of their similar electronic structures. However differences in the morphology are between the two lead to some differences in electronic structure as well. Presented here is a brief review of the properties, synthesis methods, and catalysts for the growth of these sp^2 carbons.

3.1.1 Properties

Graphene is metallic in nature, having its valence and conduction bands overlapping [182]. Single walled carbon nanotubes on the other hand, have been observed as either metallic or semi conducting, with behavior in between due to the chirality of the CNTs [46, 34, 137]. These SWCNTs chirality can be characterized by their Raman spectra to determine the (n,m) indices, however this is not the case in multi-walled carbon nanotubes. The extra concentric layers of MWCNTs decrease the radial breathing modes associated in the Raman spectra associated with the stretching of the D mode producing phonon scattering and therefore cannot have their chirality characterized by Raman spectroscopy. Furthermore, MWCNTs are semi-conducting in nature, but doping with nitrogen and boron can increase conductivity. MWCNTs do exhibit good mechanical properties (tensile strength 45 billion pascals) [104]. In respect to the properties this research seeks to

utilize, the MWCNTs synthesized increase the surface area of the carbon foams. Additionally, graphene coated carbon foams may be useful for electrical and thermal conductivity in future applications.

3.1.2 Synthesis

Methods for the synthesis of carbon nanotubes can be divided into two methods: physical and chemical[111]. Physical methods are those that input high-energy to release carbon atoms from precursors such as graphite electrodes. Two popular methods of physical synthesis techniques are Arc Discharge and Laser Ablation. In fact, CNTs were discovered by Arc Discharge method when graphite "needles" or "whiskers" were found with a mixture of carbon blacks and pyrolytic carbon by Sumio Iijima[76]. Chemical methods are those that rely on carbon desolution or atomization via catalytic metal nanoparticles with high carbon solubility and cam be further divided into Chemical Vapor Deposition (CVD) and aerosol synthesis. Gaseous precursors such as methane, acetylene, ethylene, hexane, and ethylene glycol are used during CVD as a carbon source. Typically, CVD synthesis of CNTs occurs at temperatures between 625°C-900°C. Preheating gaseous carbon sources to 770°C can lower temperature of catalytic growth to 500°C, but this does not change the diameter of the tubes grown. In aerosol synthesis, the entire desolution of carbon precursors into transition metal nanoparticles takes place in the gas phase. Some precursors such as ferrocene are used to grow metal nanoparticles in situ while another carbon feedstock is fed into the furnace. Water vapor and alcohols are also used during aerosol synthesis to accelerate the growth of CNTs, creating "forests".

3.1.3 Catalysts

Nanosized transition metal particles are commonly used at catalytic substrates for CNT growth. Generally, Fe, Ni, and Co are widely used although Pd, Mo, and Ru have also been successful as well as alloys of these metals. The general mechanism of CNT growth on catalytic metal nanoparticles is as follows: decomposition of carbon precursor molecules on the surface of the catalyst leads to the dissolution of carbon into the particle. Diffusion of carbon into the particle's surface leads to an eventual saturation in the metal as the carbon solubility limit is reached or when temperature decreases. This supersaturation precipitates a separation of phases, the morphology of which depends on the that of the catalytic substrate. The requirements of a successful CNT catalyst are:

- Carbon solubility
- Carbon Diffusion Rate
- Equilibrium Vapor Pressure
- Melting Temperature

These metals should be in reduced form and flow of H_2 or hydrocarbon gas is usually included in CVD and aerosol synthesis methods.

Control over the diameter of a nanotube is most closely correlated with the diameter of the metal nanoparticle substrate. Smaller particles (diameter = 1-2nm) generally produce single walled nanotubes or double walled nanotubes. Larger particles typically produce double walled nanoatubes or multi walled nanotubes. It is often difficult to control particle size distributions during a CVD synthesis given the thermal driving forces involved.

Evolution of the particle size is inevitable and great care must be taken to avoid sintering which decreases yield and increases particle size and thus nanotube diameter. Evaporation of the metal particles is also a risk[111].

3.1.4 Review of Raman Spectra for Carbon Materials

The use of Raman spectroscopy is is extremely useful in the identification and analysis of CNTs as well as carbon materials in general. It is therefore useful to offer a brief review of common Raman peaks used in the characterization of carbon allotropes; for more in depth reviews and insight on Raman spectroscopy, it is suggested that the reader to seek out the work of Ferrari [58, 56, 57] and Dresselhaus [51, 129, 45, 46].

Raman spectroscopy is the measure of "inelastic scattering of photons by phonons due to the change in the polarization caused by the phonon mode" [57]. It is different from fluorescence or phosphorescence in that photons are not absorbed and emitted; it is therefore not a resonance effect. The resonant states of the material determines the energy of the photon, not the energy of the incident photon; this means that Raman scattering can take place at any wavelength of light. Electrons of all wave vectors can be excited when an incident photon energy is greater than the band gap. In the case of graphite, graphene, and carbon nanotubes, the band gap in the visible range lies within a small part of k space surrounding the K point[57]. The π states and empty π^* states form bands that touch in this region. The σ bonds of diamond-like and disordered sp^3 carbons can be approximated by short-range terms. This is not the case for π states where one π orbital interacts with conjugated π states from up to 5 carbon atoms away. This includes phonon dispersion from sp^3 carbons and is why sp^2 carbon is highly sensitive to Raman scattering in the K point.

Several varieties of carbon are discussed in literature which are defined by the relative amount of sp^3 to sp^2 carbons. Some include: diamond-like carbon (DLC) which is an amorphous carbon (a-C) with a significant amount of sp^3 content and hydrogenated carbon (a-C:H), tetrahedral amorphous carbon (ta-C) and hydrogenated tetrahedral amorphous carbon (ta-C:H). Carbon materials primarily composed of sp^2 carbons include: graphite, graphene, single walled carbon nanotubes (SWCNTs), double walled carbon nanotubes (DWCNTs), and multiwalled carbon nanotubes (MWCNTs). Table 3.1 lists the following Raman peaks for carbon that will be described in order of ascending wavenumber (cm^{-1}).

Generally, Raman spectra of carbon materials are derived from one of five sources:

- Vibrations of C-C sp^3 density of states
- Hydrogenation which replaces C-C bonds with C-H bonding
- Radial Breathing Modes (RBM) involving phonons near the K zone boundary in carbons with high orders of sp^2 density of states
- In-plane bond stretching causing translational vibration modes of the sp^2 density of states
- Double resonance of primary peaks causing second-order peaks

Radial Breathing Modes (RBM) in the 100-400cm^{-1} range are found in SWCNTs and DWCNTs, but not observed in MWCNTs. These modes depend linearly on the diameter of the CNT and particle. The RBM can be used to determine the chirality ((n,m) indices) of SWCNTs and DWCNTs[46]. This radial breathing is not detected in MWCNTs

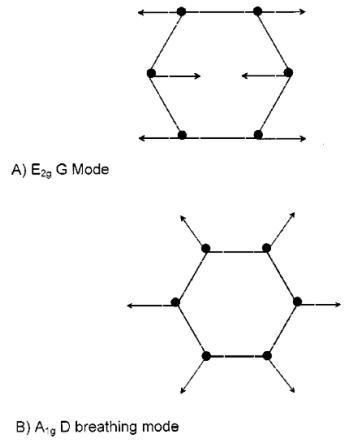

Figure 3.1: Carbon motions in the (a) G and (b) D modes. Note that the G mode is just due to the relative motion of sp^2 atoms and can be found in chains as well. Reproduced from [57]

due to the signal from the larger diameter MWCNTs being too weak to be observable and the set average of inner tube diameters broadens their signal [123, 8].

The T peak at approximately 1060cm^{-1} corresponds to C-C sp^3 vibrational density of states in ta-C simulations [58]. Due to this, the intensity of the T peak decreases with increasing hydrogenation. In addition, increasing sp^2 fraction will also decrease it's intensity and lead to the rise of a D-like peak at 1400cm^{-1} which is also present in SWCNTs[46]. The T peak can be used to broadly estimate the amount of sp^3 content in a carbon sample, hydrogenated or not, but is not as useful as other methods.

While studying DLC, Ferrari et al deduced that the trio of peaks commonly found in DLCs and other amorphous carbons belongs to that of trans-polyacetylene [58]. The first of which is the $\nu 1$ which is found at 1150cm^{-1}. It is a companion mode of the 1240cm^{-1} $\nu 2$ peak and $\nu 3$ 1450cm^{-1} peak that arises due to dispersion from the hydrogenation of carbons. It is sometimes obscured by the tail of the G peak. The 1240cm^{-1} $\nu 2$ peak from

trans-polyacetylene is very small in amorphous carbons, and difficult to detect because of the G peak [58].

The D mode around 1350cm^{-1} is a double resonance mode, associated with elastic phonon scattering close to K point of the graphite Brillouin zone. The mode is not seen in graphene or pristine graphite, and although this symmetry-breaking mode is banned in perfect graphite, it can be used as measure of structural disorder from a-C and defects in the hexagonal crystal structure. It is another type of "breathing" mode in which k wavevectors are pointing away from the middle Γ position and contributions from each 6 carbon ring add constructively because of long range polarization due to conjugation of π states [123, 8, 57]. Strain on the carbons in graphene sheets will cause the D mode to be detected in CNTs. When observed in MWCNTs, the D peak is dependent on inverse diameter of small catalytic metal particles between 5-15nm [8]. In graphite, splitting of the D mode peak can be seen at edges where dangling bonds and hydrogenation takes place. This splitting is detected at the 1340cm^{-1} and 1360cm^{-1} peaks, which are assigned to D_1 and D_2, respectively [56].

The doubly degenerate zone center E_{2g} of the G mode is non-dispersive and arises in the 1500-1600cm^{-1} range, usually localized around 1580cm^{-1}. The G band originates from the tangential in-plane stretching vibrations of the C-C bonds within the graphene, graphite, and CNT sheets [123, 8, 57]. The shape of the G peak in SWCNTs can be used to predict the electrical properties of the tubes: either semiconducting or metallic. In semiconducting CNTs, a two peaks can be observed which match Lorentzian fittings at 1565cm^{-1} and 1590cm^{-1}. In metallic SWCNTs, the 1565cm^{-1} peak is not always present, but is broad when is present and fits a Breit-Wigner-Fano (BWF) line.

The *D'* band at 1615cm^{-1} appears in MWCNTs, but not SWCNTs and DWCNTs. The *D'* band is a double resonance mode, associated with elastic phonon scattering close to Γ point of graphite Brillouin zone, and can measure of structural disorder from a-C and defects [123, 8].

The G* or D+D" mode at 2400cm^{-1} is an overtone of the power acoustic branch away from the *K* point, with a redshift with increasing laser energy [112, 57].

Located at 2700cm^{-1} *2D* or "*G'* band has the same origin of the *D* band, as explained by the double resonance theory, but it does not present the momentum conservation constraint, because it is a second order Raman feature that involves two phonon with wave vectors *q* and *-q*. In other words the elastic phonon scattering responsible for the appearance of the *D* band vectors q and -q. In other words the elastic phonon scattering responsible for the appearance of the *D* band in the presence of lattice defects is substituted by an inelastic phonon emission process for *G'* band" [8]. The *G'* band has nothing to do with the G peak, but is the second order of zone-boundary phonons. Since zone-boundary phonons do not satisfy the Raman fundamental selection rule, they are not seen in first order Raman spectra of defect-free graphite and not dependent on defects [56].

At the far end of the Raman spectrum for carbon materials, a-C:H materials can exhibit peaks at around 2800cm^{-1}. These could be due to C-H bonds or non-fundamentals rendered Raman active by symmetry reduction during laser degradation [115]. A peak at 2900cm^{-1} is sometimes seen in graphite and CNT samples which starts at 2900cm^{-1}, then splits into 3 peaks at 2400cm^{-1}, 2700cm^{-1}, and 2900cm^{-1} due to increasing crystalline structure [38]. Other peaks can be observed at approximately 3100cm^{-1}.

Table 3.1: Common Raman Peaks for Carbon Allotropes

Wavenumber (cm^{-1})	**Mode**	**Carbon Allotrope**	Reference
100-400	RBM	SWCNTs, DWCNTs	[123, 8]
1060	T	ta-C, DLC, trans-polyacetylene	[58]
1150	ν_1	a-C:H, trans-polyacetylene	[58]
1240	ν_2	a-C:H, trans-polyacetylene	[58]
1350	D	a-C, DLC, imperfect graphite,	[123, 8, 57]
1340 & 1360	D_1 & D_2	Seen at graphite edges	[56]
1450-1480	ν_3	a-C:H, trans-polyacetylene	[58]
1580	G	Found in all carbons	[123, 8, 57]
1615	D'	MWCNTs	[123, 8]
2400	G* or D+D"	a-C, DLC, imperfect graphite	[112, 57]
2700	G' or 2D	a-C, graphene, graphite, all CNTs	[8, 56]
2800	N/A	a-C	[115]
2900	N/A	a-C, DLC, imperfect graphite	[38]

3.2 Growth of Carbon Nanotube and Graphene Foam

The lessons learned while comparing graphite encapsulation in the Fe, Ni, and Co variations of carbon foams to the mechanisms for growth of CNTs on catalytic metal nanoparticles lead the author to the logical step of attempting to synthesize CNTs onto the carbon foam including these three transition metals. The procedure outlined below takes into consideration the temperatures of graphitic encapsulation and the carbon solubility of Ni and Co in particular. A systematic study of the morphology of the carbons undergoing phase separation from catalytic metal substrates is presented resulting in the production of MWCNTs using Ni catalysts and multi-layer graphene using Co catalyst at similar sugar to metal precursor ratios.

3.2.1 Synthesis of Carbon Foam with Embedded Metal Particles

Carbon foams were synthesized with procedures similar to previous studies by this group by Bay [15] and Villalobos2019. Synthesis consisted of oxidation of simple polysaccharide with metal nitrates and nitric acid to reach a pH of 1 in aqueous solution. Xylose was chosen as the sugar while $Ni(NO_3)_2$ and $Co(NO_3)_2$ were selected as precursors for metal nanoparticles. Ni, and Co exhibit enough carbon solubility to dissolve carbon feedstocks into a solid solution at high temperatures (627°C - 950°C)[41, 36]. Due to eutectic compound formation, the increase in carbon content in the semi-liquid state of nano-sized particles causes the separation of phases [72] and the precipitation of carbon allotropes such as graphite, graphene, and carbon nanotubes. For this reason Ni and Co were chosen for embedding into carbon foams. Ratios of 4-1, 8-1, 20-1, 200-1, 2000-1 sugar-metal molar ratios were used for comparison.

Graphite encapsulation within carbon foams has been observed and predicted above 627 °C [15] and Villalobos2019. To avoid graphitization while promoting the growth of catalytic metal nanoparticles carbon foams were annealed at 600°C for 1h. Prior to CVD synthesis of CNTs, annealed carbon foams were ground with mortar and pestle to reduce the size of particulate foam and sieved under $20_m u$m. This decrease in particle size increases surface area and exposes more embedded metal nanoparticles to the gaseous carbon feedstock during CVD synthesis. For hierarchical CNT foam for oil sorption and hydrophobic properties, annealed carbon foam pieces were milled until sieved between 500μm and 100μm mesh.

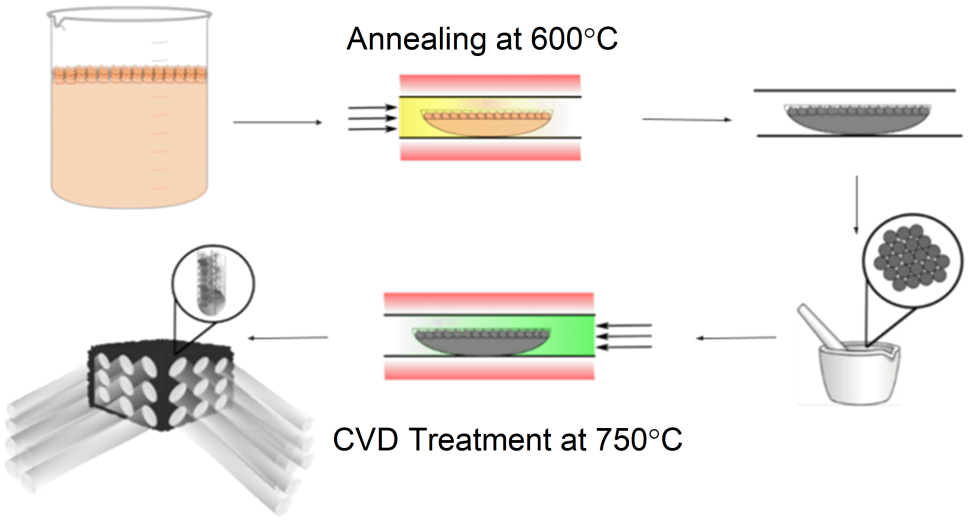

Figure 3.2: Synthesis Schematic: Top left: Mixing and foaming step, Top Middle: annealing for particle growth step, Top Right: annealed particles embedded within carbon foam, Bottom Right: milling by mortar and pestle and sieving to control carbon foam chunk size, Bottom Middle: CVD treatment for CNT and Graphene growth, Bottom Left: final growth of CNTs or graphene

3.2.2 Growth of Carbon Nanotubes

Crushed, <20μm carbon foam was placed into a tube furnace for carbon nanotube growth by Chemical Vapor Deposition. Crushed carbon foam was exposed to an equimolar ratio of H_2 and Ar atmosphere while ramping up from 25°C to 750°C in 30 min. This allows any oxide layers coating the metal nanoparticles to be reduced. Carbon foam was held at 750°C for an additional 30min while H_2 gas was shut off and acetylene gas was used as carbon source in excess. Cool down ramp was 45min. An attempt was made to use methane as a carbon source, but carbon removal from the foam was observed in the same temperature range. Residual metal particles were instead sintered together in the same morphology as the carbon foam, leaving behind a metal foam possibly using the carbon matrix as a scaffold or mold. Adjusting the temperature can drive the sintered metal into a wired network or a foam. This metal foam can subsequently be used as a substrate for CNT growth when using acetylene as gaseous carbon source at the conditions above. More information regarding metal foams synthesized from carbon foams can be found in Section 3.4.

3.3 Results and Discussion

Due to the differences in carbon solubility, different sized metal particles are expected to nucleate during the 600°C annealing step. This should lead to differences in CNT diameter and additionally, different morphologies of carbon materials are synthesized when switching from Ni to Co, even at the same ratio. Methods used to characterize these carbon morphologies include SEM and the use of ImageJ software to measure the CNT diameters,

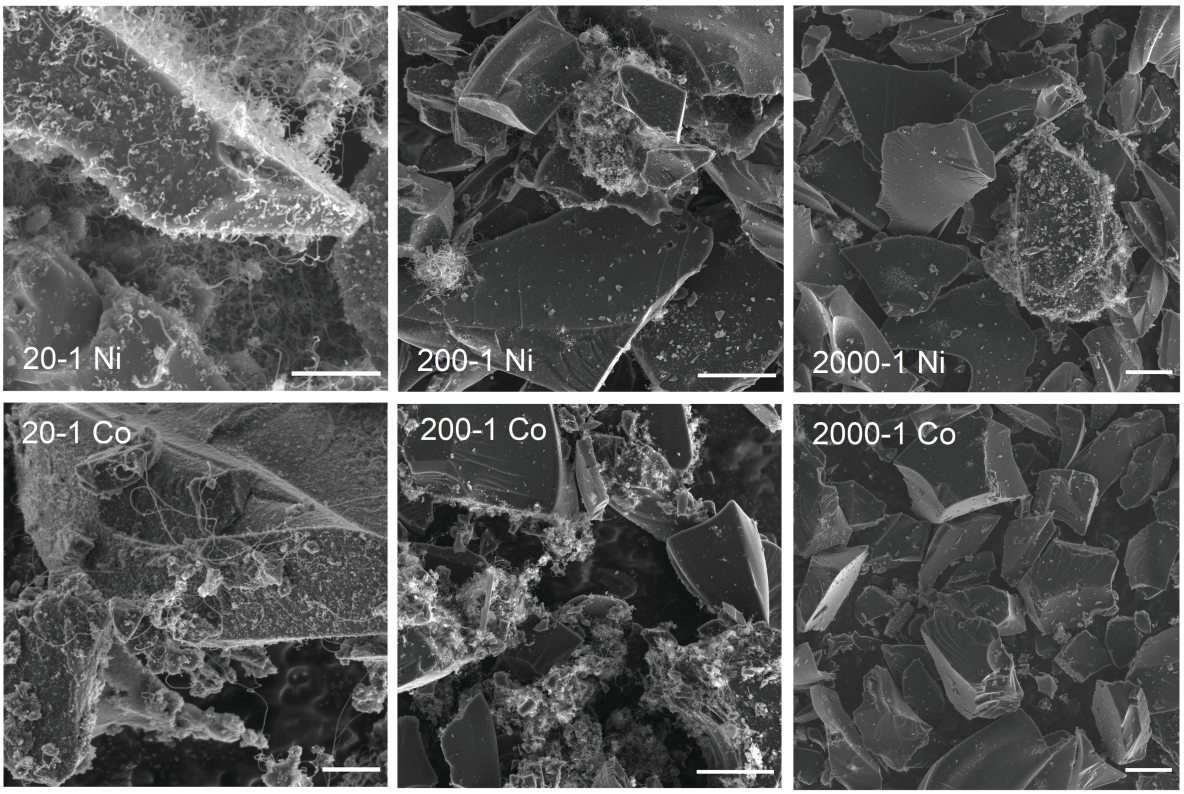

Figure 3.3: 20-1 is at 5μm, 200-1 is at 10μm, 2000-1 is at 10μm,

SAS statistical software to calculate data sets and normality of the data, as well as traditional methods like XRD and Raman. Lorentzian peak fitting is used to analyze the Raman spectra to discern the electronic structure as well as analyze the XRD spectra to calculate the Ni and Co grain sizes used during CVD treatment.

3.3.1 Characterization of Carbon Foam Substrate and Carbon Nanotubes

SEM A comparison of 3 sugar-metal ratios (20-1, 200-1, 2000-1) between Ni and Co is presented in Figure 3.3. Comparing the 20-1 ratios shows that both Ni and Co produced nanoparticles that are available for CNT growth at their surface. However, Ni promotes

growth of longer CNTs than Co. In the Co 20-1 sample, shorter CNTs are more common than those that are longer, although CNT diameter does not change much between the ratios. As the xylose content is increased to the 200-1 and 2000-1 ratios, Ni and Co particles become more sparse, being found in small, dense agglomerations where the particles then nucleate CNT growth during CVD synthesis. This is demonstrated in Figure 3.3. At the 8-1 ratio, CNTs successfully coat the Ni-carbon foam. At the 4-1 ratio, CNTs are less prevalent than at 8-1, while also measuring larger in diameter on average. Both the 4-1 and 8-1 Co-carbon foam did not produce a significant amount of CNTs when undergoing CVD. Instead, small pseudo-graphitic crystallites formed on the surface of the porous foam as seen in Figure 3.7. Differences in carbon solubility may be responsible for these contrasting morphologies.

XRD Figure 3.4 indicates the crystallinity of the metal nanoparticles embedded in carbon foam chunks sieved through a 20μm mesh to then undergo CVD treatment (a and b) as well as pretreatment annealing to 600°C (c and d). Due exposure to air, metal oxides are detected in all ratios. The (311), (400), (440), and (533) reflections are assigned to Co_2O_3 [27]. However, Figure 3.4 demonstrates that at higher metal ratios (4-1, 8-1, and 20-1), the (111), (200), (220), and (311) reflections for FCC Ni and Co are detected. The (222) reflection is also detected for Ni as seen in Figure 3.4a. Due to the multi-walled nanotube's concentric graphene sheets, the XRD spectra strongly resembles those for graphite. The (002) diffraction peak at 27°for graphite is clearly produced at the 4-1, 8-1, 20-1, and 200-1 ratios in the CNT Ni-carbon foam. The (101) graphite peak maybe present at the shoulder

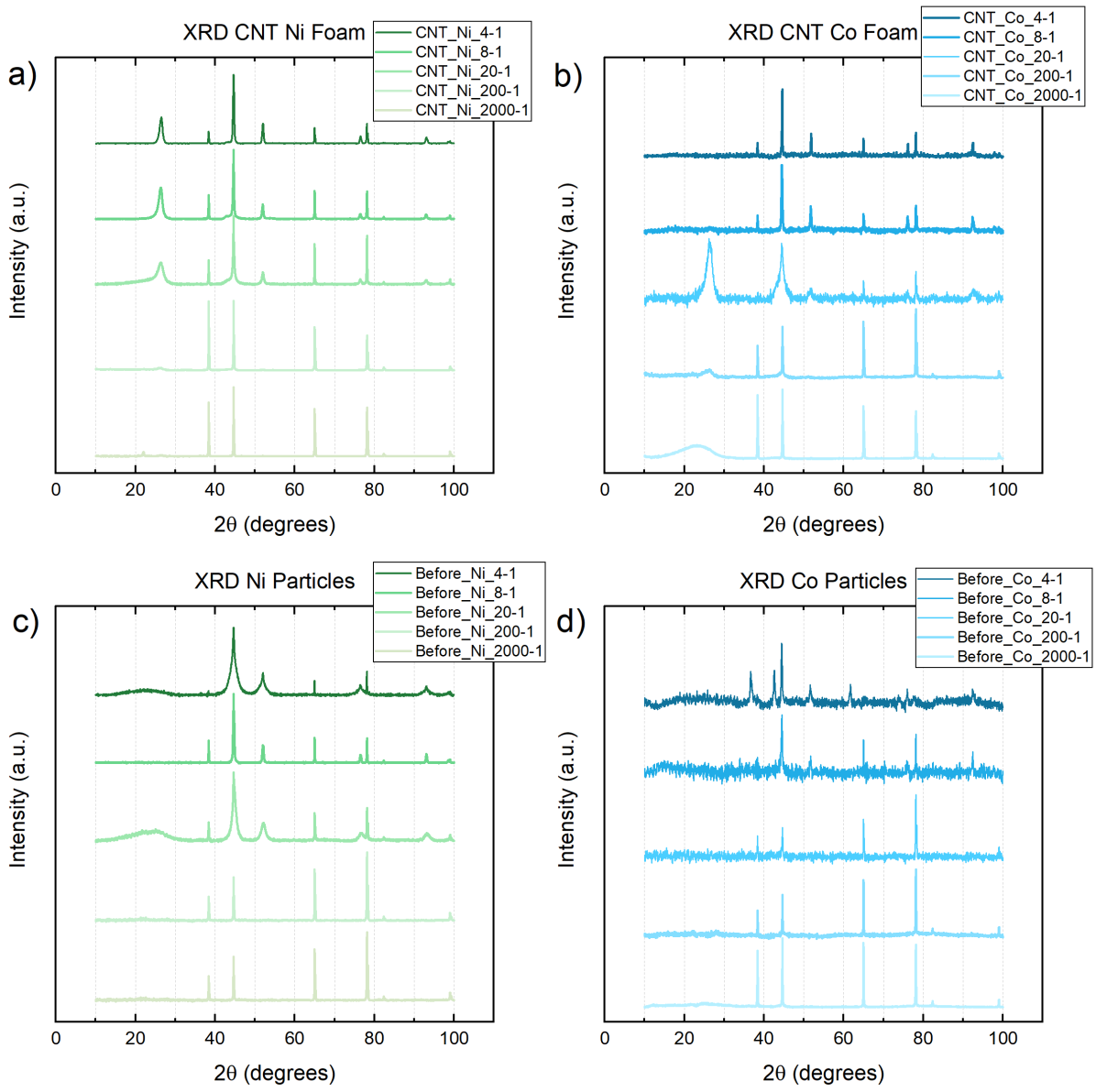

Figure 3.4: XRD spectra for sugar-metal ratios 4-1, 8-1, 20-1, 200-1, 2000-1 are depicted for a) CNTs grown on Ni carbon foam substrate b) CNTs grown on Co carbon foam substrate c) Ni carbon foam pieces treated at 600°C for 1hr d) Co carbon foam pieces treated at 600°C for 1hr

of the (111) Ni peak at approximately 44°in the 4-1, 8-1, and 20-1 ratios. In the CNT Co-carbon foam, graphite is prominent at the 20-1 and 200-1 ratios. Specifically, at the 20-1 ratio, a broad (002) graphite peak is present with a broad Co (111) peak, suggesting that as graphitization of the carbon nanotubes increases, crystallinity of the Co nanoparticles decreases. This may be due to differences in carbon solubility at the nanoparticle scale. At the 2000-1 ratio, amorphous carbon (a-C) is likely detected for the CNT Co-carbon foam. Curiously, the graphite peak is absent in the 4-1 and 8-1 ratios for Co. Grain size diameter for Ni was calculated using full width half max (FWHM) and Scherrer's Eq. for each sugar-metal ratio. Grain sizes were calculated to be: 53.51nm, 50.91nm, 39.03nm, 27.99nm, and 30.03nm for the 4-1, 8-1, 20-1, 200-1, and 2000-1 ratios, respectively. Grain sizes for Co 2000-1 and 200-1 were not able to be calculated due to the Absence of significant intensity of Co peaks. FWHM peaks for Co_2O_3 is not able to be used because CNT grow from pure Co nanoparticles. The process of carbon phase separation during CNT growth encapsulates catalytic Co particles, preserving their crystallinity. Any oxides present would therefore not have taken part in the growth of CNTs and therefore should not be used to estimate catalytic particle size diameters. Peak analysis and fitting were able to estimate the diameter of Co grains in 20-1, 8-1, and 4-1 ratios to be 25.62nm, 81.48nm, and 54.99nm, respectively.

CNT Stats The diameters of CNTs are observed to be dependent on particle diameter, as is commonly noted in literature [28, 111]. A study of CNT diameter was undertaken to compare the diameters of CNTs between Ni and Co, and between the sugar-metal ratios chosen in this study. Approximately 100-200 CNT diameters were measured for each of the

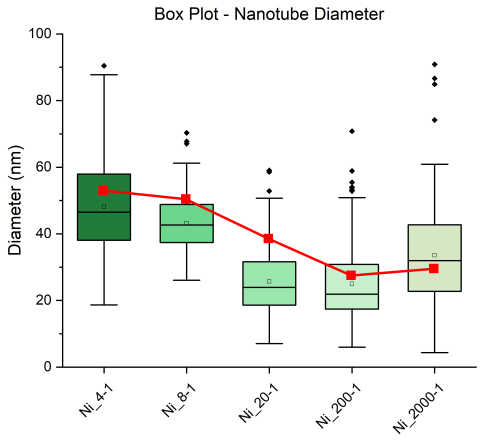

Figure 3.5: A compilation of the average MWCNT diameter as measured by ImageJ. Red line indicates the Ni grain size diameter calculated by Scherrer's Equation using FWHM of XRD Spectra in Figure 3.4

3

Ni and Co foams that produced CNTs after CVD synthesis. The 4-1 and 8-1 Co-carbon foams exposed to CVD synthesis did not produce a significant number of CNTs and did not produce a large enough sample size to measure. Normality was tested using a PrcoGLM test. If distribution was not normal, a Satterthwaite fitting was used. Comparisons between Ni and Co and ratios were done using a ProcTTest to test for significance. Average CNT diameters from Ni for the 4-1, 8-1, 20-1, 200-1, and 2000-1 were calculated to be: 48.13nm, 43.19nm, 25.68nm, 24.99nm, and 33.54nm, respectively. Average CNT diameters from Co for the 20-1, 200-1, and 2000-1 ratios were calculated to be: 32.64nm, 33.83nm, and 32.37nm, respectively. A summary of the histograms collected from the data is presented in Figure 3.5. Average diameters of the Ni CNTs calculated by SAS agree with diameters of the Ni grain size calculated by Scherrer's Eq. using FWHM from Figure 3.4.

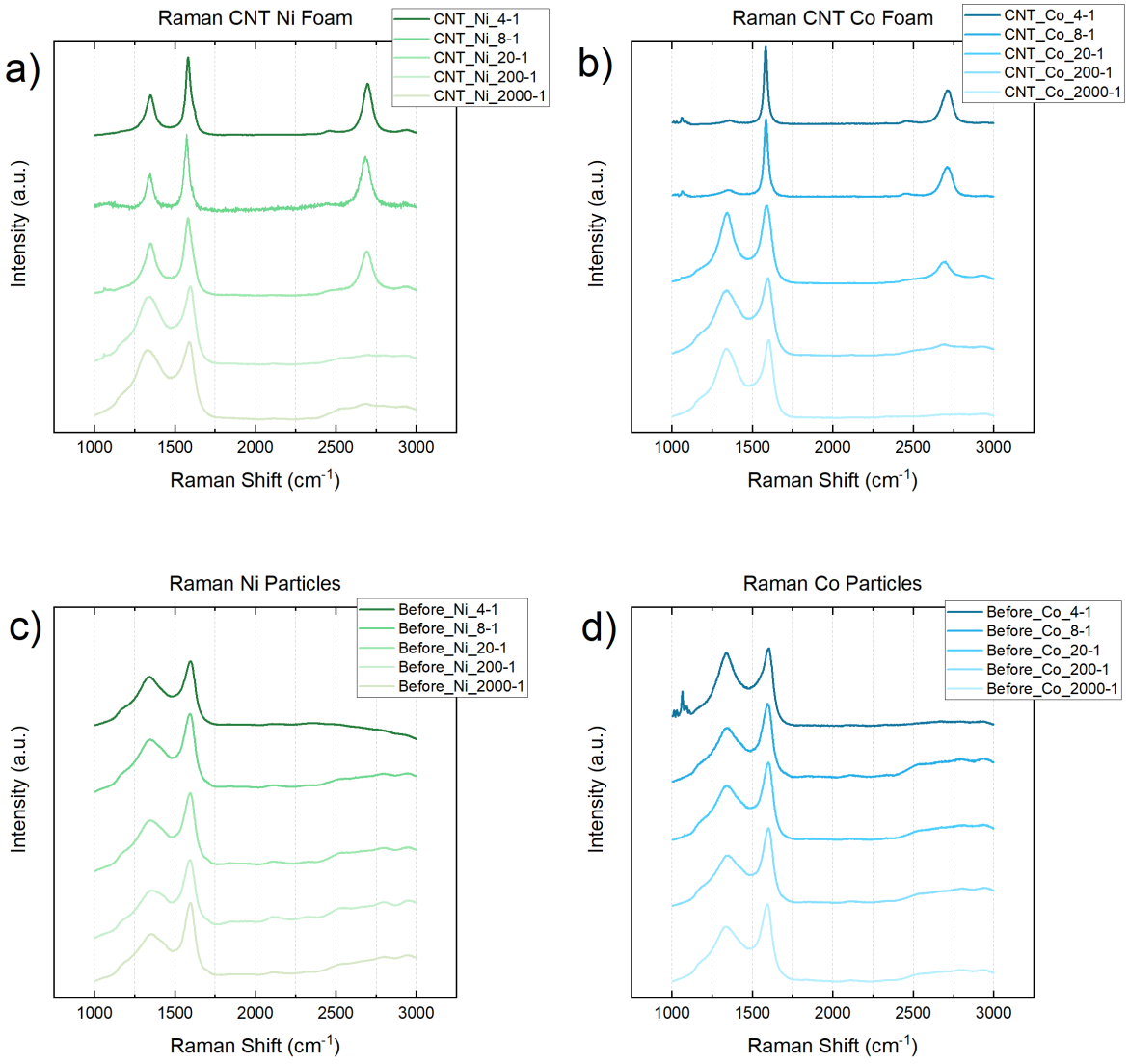

Figure 3.6: Raman spectra of a) CVD treated Ni-carbon foam, b) CVD treated Co-carbon foam, c) Ni-carbon foam post annealing and before CVD treatment, d) Co-carbon foam post annealing and before CVD treatment

Raman Raman spectra of the CNT foam was taken for each ratio of the Ni and Co samples as seen in Figure 3.6. Samples exposed to CVD treatment are shown in Figure 3.6a and b, while samples annealed to 600°C are shown in c and d. All samples annealed at 600°C display a similar spectra analogous to a-C. In conjunction with the XRD data in Figure 3.4, the Raman spectra suggests nucleation of crystalline nanoparticles without graphitization of carbon is achieved. The 4-1, 8-1, and 20-1 samples which underwent CVD treatment show characteristic graphitic peaks in the Raman spectra. Spectra for the 200-1 and 2000-1 ratios for both Ni and Co also show amorphous shape that may be due to hydrogenation. Lorentzian peaking fitting was used to demonstrate the appearance of ν_1 and ν_3 peaks assigned to trans-polyacetylene [58] in the 1100-1250cm^{-1} and 1400-1550cm^{-1} ranges, respectively. The detection of a-C is expected as the SEM micrographs in Figure 3.3 attest to the increasing scarcity of CNTs in both the Ni and Co samples as metal concentration decreases as well as the decrease in intensity of the (002) graphite peak in Figure 3.4. The increase in D peak intensity for 200-1 and 2000-1 ratios is attributed the increasing sp^3 carbon content which also contributes to sp^2 radial breathing modes (RBMs).

A closer look at the peak fitting for 4-1, 8-1, and 20-1 ratios for Ni and Co treated by CVD is shown in Figure 3.7. The presence of the ν_1 and ν_3 peaks is indicative of the relatively high ratio of carbon to metal still present at the 20-1 ratio for both Ni and Co. The appearance of the D' peak signals the presence of MWCNTs in both Ni and Co 20-1 samples, as it does not appear in the Raman spectra of SWCNTs [123, 8]. However, the decrease in the relative intensity of the D peak to the G peak (I_D/I_G) may be indicative

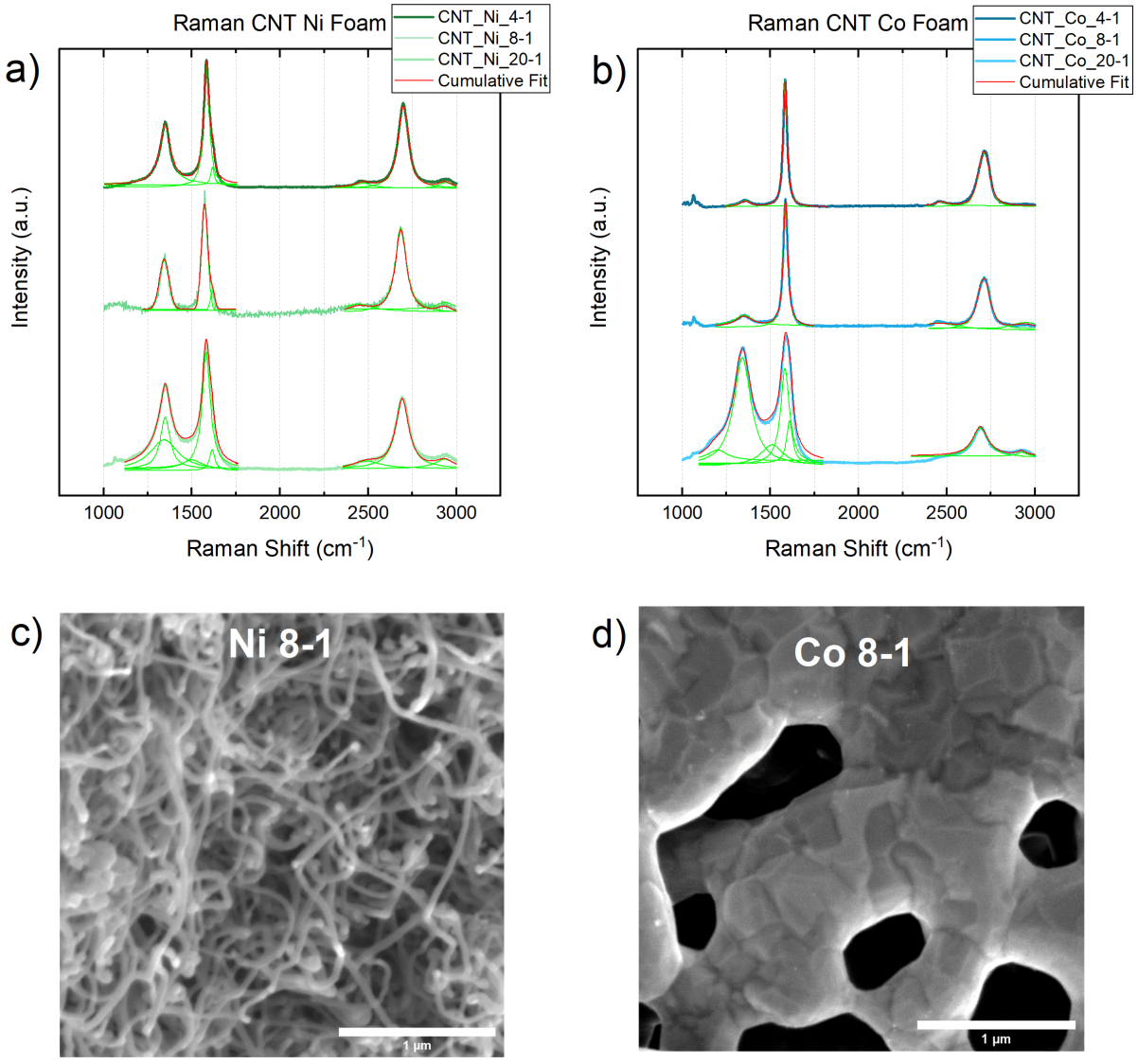

Figure 3.7: Raman peak analysis by Lorentzian fitting is used to characterize the elctronic structure of the carbon materials synthesized using the 4-1, 8-1, and 20-1 ratios for a) Ni and b) Co. SEM micrographs of the carbon morphologies precipitated at the 8-1 ratio for c) Ni and d) Co

of the splitting of the D peak into D_1 and D_2 peaks in Ni 20-1 spectrum which emerge at graphite edges [56] where defects exist. Similar defects may be present in Ni 20-1 MWCNTs. A larger D is measured in the Co 20-1 which indicates the potential for greater sp^3 than Ni 20-1. This is also observed in the micrographs in Figure 3.3, where CNTs are generally shorter in length more sparse. Double resonance causes the *2D* to be found in both Ni and Co 20-1 samples at approximately 2700cm^{-1} [8, 56] along with a peak at 2900cm^{-1} that can be associated with hydrogenation [38]. An overtone of the the power acoustic branch away from the K point leads to the detection of the G* or D+D" at 2400cm^{-1} [112, 57]. At the 8-1 and 4-1 ratios a significant difference is spotted in the Raman spectra between Ni and Co CVD treated foams. In Ni 8-1 and 4-1, characteristic MWCNTs peaks such as the *D*, *D'*, and *G* peaks are detected. At smaller catalytic Ni particle diameter, the behavior of I_D/I_G, $I_{D'}/I_G$, and $I_{G'}/I_G$ is known to scale with reciprocal diameter (1/d) and therefore diameter of the catalytic nanoparticles. This was not observed in the Ni MWCNT as seen in Figure 3.8; neither SAS nor Scherrer diameter produced a linear fit. This behavior may only hold for particles 20nm or less, as observed by Antunes et al [8]. Behavior of the *G* and *G'* FWHM was observed to fit linearly with both SAS and Scherrer estimated diameters, although Scherrer analysis measured better R^2 fit compared to SAS. Raman spectra for the Co 4-1 and 8-1 ratios see a reduction in the *D* peak, suggesting less distortion in the electronic structure of the carbon. The $I_{G'}/I_G$ of 0.43 suggests that for 4-1 and 8-1 Co samples, multi-layer graphene is present [126, 65]. Lack of a (002) graphite peaks in Figure 3.4b as well as SEM micrographs seen in Figure 3.7d agree with the notion that carbon enveloping the porous foam structure is multi-layer graphene, or at least an sp^2 carbon

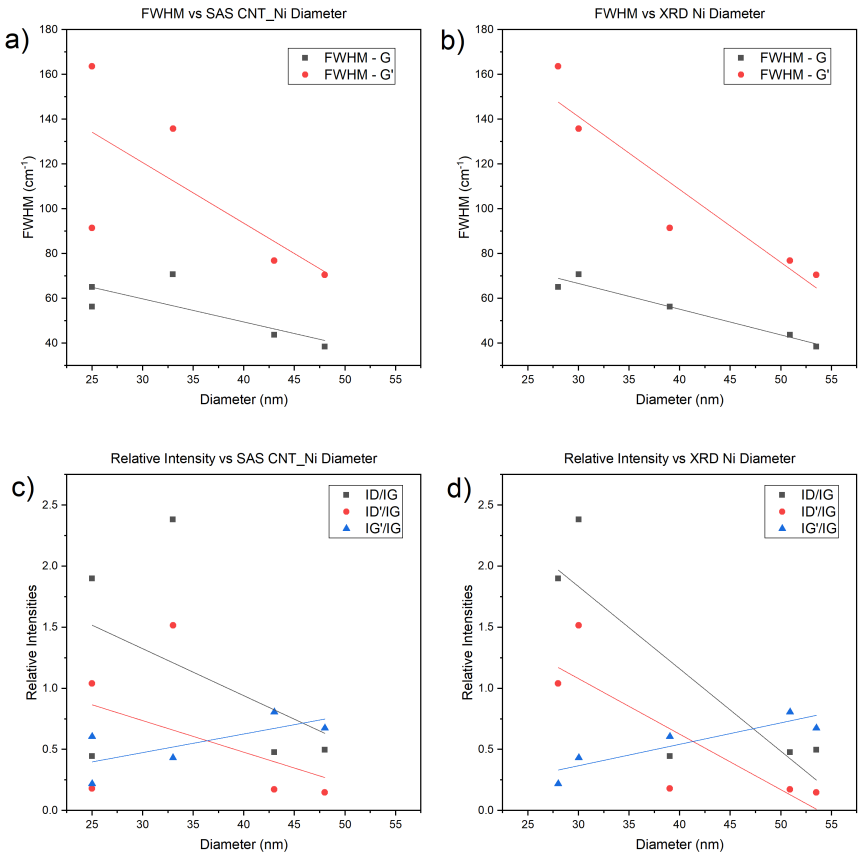

Figure 3.8: Comparison of CNT diameter calculated using SAS statistical software versus Ni grain size diameter calculated by Scherrer's Eq. using FWHM of XRD Spectra in Figure 3.4 to investigate the scaling of Relative Intensities and FWHM with catalyst diameter. a) plot of FWHM vs SAS b) plot of FWHM vs Scherrer Eq. c) plot of Relative Intensities vs SAS d) plot of Relative Intensities vs Scherrer Eq.

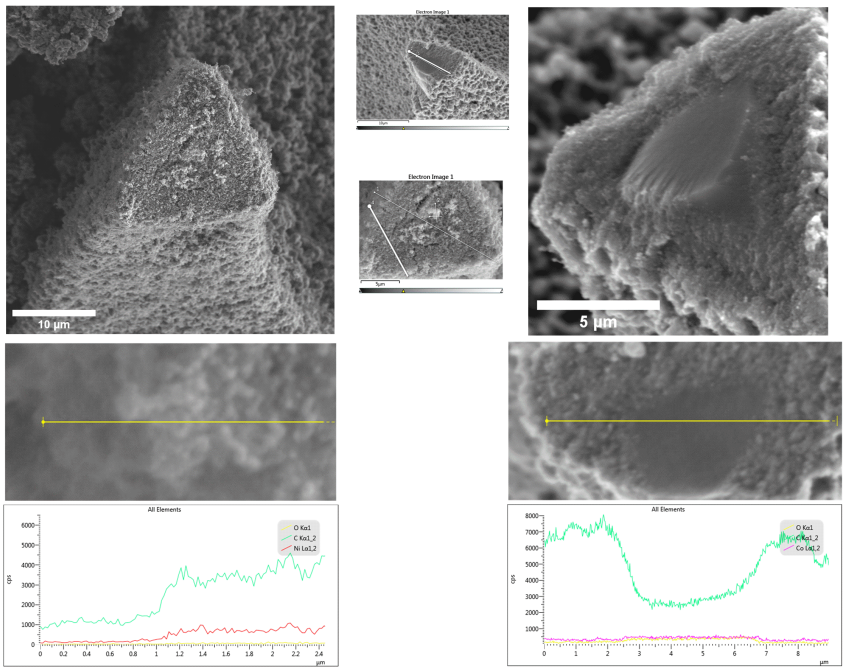

Figure 3.9: EDS line scans were taken at exposed joints or struts in the CVD treated Ni (Left) and Co (Right) carbon foams

lacking hexagonal crystal structure and AB stacking such as turbostratic graphite [95]. In any case, MWCNTs are not observed in Co 4-1 ratio, and are rare in 8-1 ratio.

Carbon "plates" with diameter approximately 100-300nm are pictured in Figure 3.7d. Estimation of Co grain size by Scherrer Eq. calculates diameters of 81.48nm and 54.99nm for 4-1 and 8-1, respectively. These grains may be in close enough proximity to form a substrate whereby carbon phase separation takes place. To investigate internal structure of the metal carbon foam substrate, EDS linescans were performed on exposed cross sections of carbon foam joints or struts as seen in Figure 3.9. The line scans for the 4-1 Ni sample joint show a consistent presence of carbon and Ni. MWCNTs can be seen in the SEM micrograph as well. This suggests that the carbon solubility of Ni is not so low that separation of Ni is so much so that clusters of Ni atoms during annealing

agglomerate into particles greater than 54nm, as estimated by the XRD spectra for the Ni 4-1 ratio. The micrograph for the 8-1 Co sample treated with CVD synthesis exposes a core shell structure of the foam joints. Line scans of the region show a decline in carbon content with a simultaneous rise in Co signal, though only slightly. This suggests the core is significantly lower in carbon content than the shell. In contrast with the Ni 4-1 sample, the carbon solubility of crystalline Co is lower than that of crystalline Ni, between 0.2-0.3% and 0.29% (atomic % C), respectively at the temperatures at which CVD synthesis takes place [154, 147, 39, 71, 36, 80, 64, 2]. Larger Co grains could be agglomerating into plates between 100-300nm in diameter, creating a substrate for graphene growth. The slightly higher carbon solubility for Ni grains may be above the threshold for platelets to form, keeping their spherical shape and nucleating CNTs. The difference in crystalline carbon solubility may affect the diameter at which these nanoparticles and grain sizes nucleate.

These carbon solubilities must be balanced by the carbon solubility of liquid Ni and Co, which are an order of magnitude higher reversed: Co having higher carbon solubility (15%) than Ni (12%) in the liquid state. If we are to take into account the MD models of F. Ding et al., we must consider a catalytic metal particle with a crystalline core and a shell which behaves as a liquid because of its greater atomic distances than allowable for a crystalline solid as detailed by the Lindemann Index[55]. This liquid behavior of the shell is due to two components: the carbon diffusion into the catalyst particle and the size effect. Because the interface between phases is defined as being at equilibrium, phase diagrams can give insight into the behavior of the metal particles during CVD. Larger Co particles (estimated grain size between 55-82nm by XRD for 4-1 and 8-1 ratios, respectively)

have a higher crystallinity, and therefore a larger fraction carbon solubility between 0.3-0.8%. The liquid shell of these larger Co grains would also have smaller fraction to the crystalline Co, having a smaller fraction of higher carbon solubility in this liquid state. In contrast, the smaller Ni particles (between 51-52nm in the 4-1 and 8-1 ratios, respectively) would have a larger fraction of liquid shell to crystalline cores. This means that a larger fraction of the catalytic Ni nanoparticle would have liquid behavior and thus higher carbon solubility overall compared to a larger Co particle. Differences in the solubility of carbon may explain the differences in particle size, and therefore, morphology of the graphite allotropes separated from solid solutions of carbon and metal at the nanoscale.

3.4 Carbon Foam as Sacrificial Substrate for Synthesis of Metal Foams

During the course of searching for a gaseous carbon feedstock for CVD treatment of carbon foams, methane was explored and interesting results were recorded. The use of methane at 1000°C resulted in the decomposition of the carbon matrix leaving behind an interconnected metal foam wire matrix. Subsequent experiments were performed and the viewing the metal foam in SEM, it was decided to attempt to purposely synthesize a metal foam. This small experiment and characterization are presented below.

3.4.1 Synthesis and Procedure

A Ni-carbon foam at 8-1 ratio was chosen as sacrificial substrate for the nucleation of particles during annealing at 600°C. After review of carbon activation procedures [108,

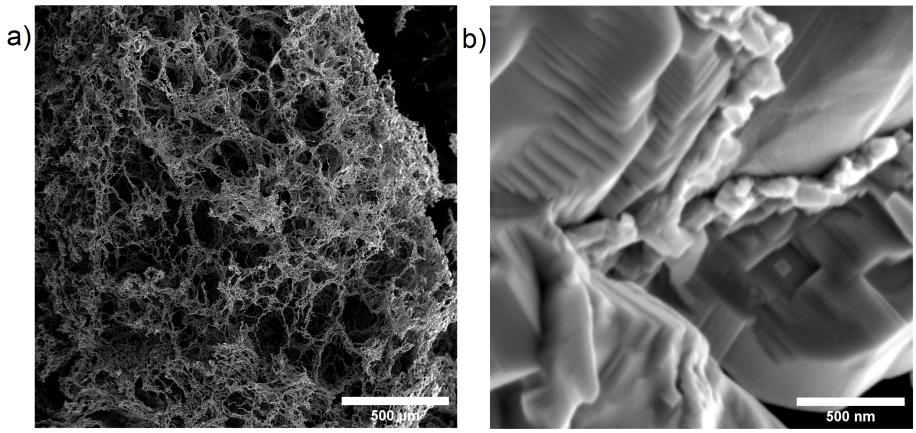

Figure 3.10: SEM micrographs of the synthesized Ni foam at a) macro-scale morphology and b) nano-scale morphology

73], CO_2 was chosen for its proven ability to decompose carbon particles into CO. Carbon foam containing annealed Ni particles was then placed into tube furnace and heated to 800°C from of 25°C over a 50min period in a 1:1 volumetric flowrate of Ar (200mL/min) and H_2 (200mL/min) environment. At 800°C, the H_2 gas was turned off and CO_2 was flowed at 100mL/min for 3 hours. Tube furnace was cooled back to room temperature over a 45min period. To probe the crystallinity, additional HCl etching was performed and to explore potential use as a CNT or graphene growth substrate, CVD treatment using the same procedures as Section 3.2.1 were carried out.

3.4.2 Characterization

Brief investigation of the resultant metal foam was performed using simple characterization of the morphology by SEM and EDS as well as crystallinity by XRD. The morphology of the metal foam at the macro-scale very much resembles that of the carbon foam from which it came as seen in Figure 3.10a. It is thought that the slow decomposition

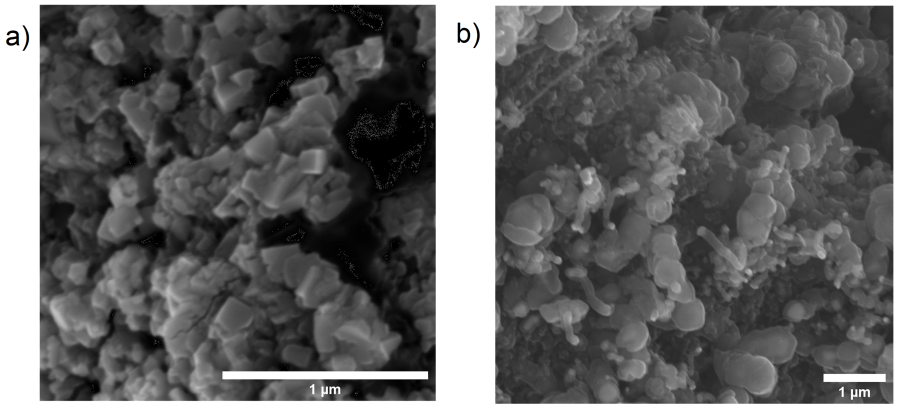

Figure 3.11: SEM micrographs of a) Ni foam etched by HCl and b) carbon nanostructures precipitated after CVD treatment

of the carbon bulk structure allows the steady removal of carbon and the migration of Ni particles towards agglomeration. As the Ni particles come into contact, sintering takes place and a network of Ni particles in the same orientation of the carbon sacrificial substrate takes shape. The carbon matrix is essentially a mold from which the Ni foam can precipitate. These Ni particles retain their crystalline faces as seen in Figure 3.10b. This may serve as a preferential growth face for graphene or other planar morphologies in future CVD treatment experiments. Etching by HCl reveals these cubic faces in more detail as seen in Figure 3.11a. A quick experiment to gauge the potential of the Ni foam as a substrate for CNTs was performed and is featured in Figure 3.11b. Pictured in Figure 3.11b are a mixture of CNTs and encapsulated metal particles. These may be graphitic sheets and if so, are referred to as carbon nanocapsules in literature [42]. If graphitic sheets are present but not encapsulating a Ni particle, these would be referred to as onion-like carbon [51, 137, 77, 42]. The crystallinity of the Ni-foam shows the presence of both Ni and NiO reflections. This is confirmed by the EDS mapping as seen in Figure 3.12 which detected 71% Ni, 20.8% O,

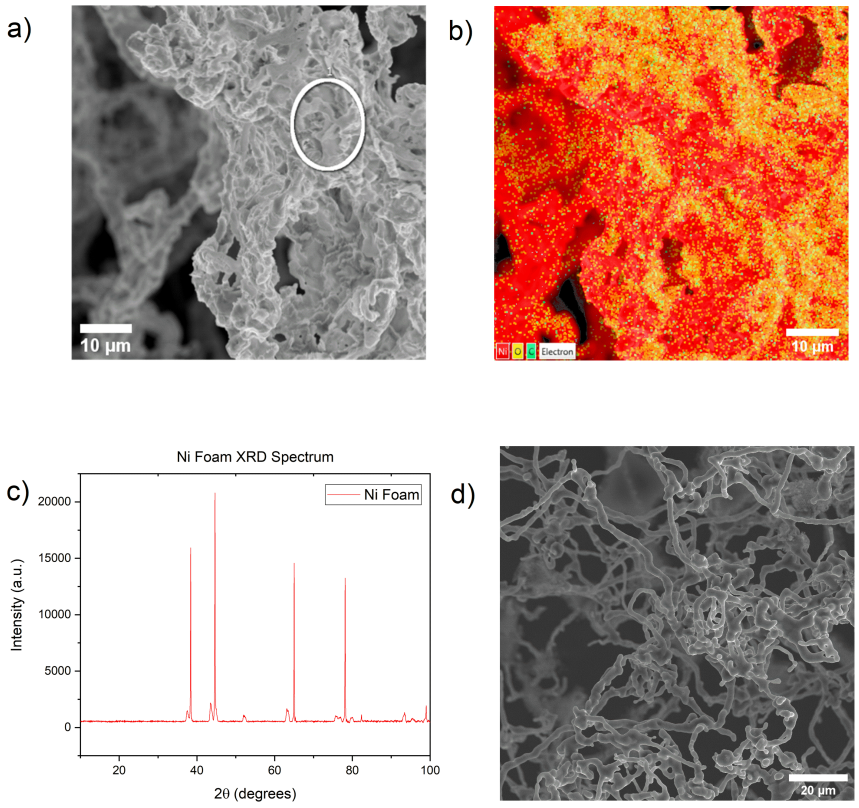

Figure 3.12: EDS was taken from the Ni foam at a) the enclosed circle and EDS mapping shows the presence of Ni, O, and C in b). XRD spectra of the Ni-foam is presented in c) and d) shows a thicker Ni-foam wire morphology

and 8.3% C. This indicates that improvements to the synthesis process are necessary. Two recommendations are suggested: first, the presence of O in both the oxide can be reduced by following CO_2 activation procedures with additional exposure to H_2 gas during cooling or for a set time; second, the presence of carbon in the EDS suggests that CO_2 activation can be improved, this can be achieved at higher temperatures (up to 1000°C) or for longer periods of time. Still, the use of carbon foams as sacrificial substrates may show promise as a cheap and easy method of metal-foam synthesis and should be further pursued.

Chapter 4

Selective Oil Sorbent CNT Foam

As stated previously, fundamental insights from the governing principles of material science, chemistry, and physics can be exploited in order to develop new molecules, materials, and technology. Data from earlier experiments is used to ascertain the functionality of carbon foams for their use in selective oil sorption in this chapter. A review of oleophilicity and hydrophobicity is presented along with a review of other sorbent materials. Finally a hierarchical CNT carbon foam is designed and tested for oil sorption and hydrophobicity using contact angle goniometry.

4.1 Properties of a Selective and Efficient Material

As news of the BP oil spill spread, the public responded with suggestions for oil adsorbing materials. These included: straw or hay, wool, and even hair. These materials did in fact display oil adsorbing properties [181], with the added benefit of having low cost, renewable sources, and being environmentally benign. However, these materials did not

display additional properties that would be preferable; such as high surface area, selectivity, and efficiency. Researchers suggested zeolites, activated carbons, and organoclays [181]. Again, these materials lack the cost effective, environmentally benign attributes of those suggested by the public and there lies an opportunity to seek a middle ground.

To evoke the desired sorption capabilities, the material would most likely be highly porous to achieve high surface area. Realizing high selectivity for oil meant the material would need to be oleophilic and hydrophobic. Oleophilicity describes a material's propensity to adsorb oil from a solvent while hydrophobicity describes a material's ability to repel liquid water. A material with both these attributes would be able to sorb oils and nonpolar solvents without wasting pore space by sorbing water and other polar liquids.

4.1.1 Oleophilicity

Oleophilicity is a result of intermolecular forces such as the dispersion effect[18], a negative interaction energy which acts as an attractive force on non-polar molecules to aggregate as can be seen in simple molecules (H_2, N_2, CH_4), some long chain polymers, and hydrocarbons [103]. This can be analogous to the development of instantaneous dipoles as molecules approach each other causing electrons to repel each other, in a quantum mechanical explanation the coulombic interactions between electrons and nuclei cause fluctuations in the electron density creating regions of attraction between molecules[102, 103]. Measurements of oleophilicity in porous materials are relatively simple as demonstraed by Equation 4.1; time-lapse video is recorded of an oil droplet which is released onto the adsorbing material. The frames from the time of initial contact to disappearance of the droplet into the material are counted and time calculated using the frames per second (FPS) of recording to

give the adsorption time of the uptake. Additionally, a scale is used to determine the mass of oil adsorbed into the material, together with the adsorption time, a rate of adsorption is attained. It is more common in literature to report the ratio of the mass of oil sorbed to the mass of the sorbent material. This is what we report in Section 4.3.

$$AdsorptionTime = (Frame_{Final} - Frame_{Inital}) \times FPS \tag{4.1}$$

4.1.2 Hydrophobicity

Hydrophobicity arises one of two ways: firstly, from a molecule or structure's nonpolarity, robbing a water molecule's ability to form hydrogen bonds with the molecular surface and secondly, from the morphological structure of a surface, where pockets of air pressure between grooves in a rough surface prevent any contribution of intermolecular forces and repels water droplets [164]. The second type is not from water's disaffinity to the chemical composition of a surface[106] is only due to physical means, an example of which is shown in Figure 4.1.

Quantification of hydrophobic surfaces are recorded by the use of contact angle goniometry. Contact angle is the angle θ, measured as a result of a droplet's spherical shape in contact with the surface in question as seen in Figure 4.2. The hydrogen bonds of water molecules shape the droplet which has a surface tension $\boldsymbol{S}$ between the liquid droplet and the air which is proportional in magnitude to its surface energy. This can be related to the surface energy between the liquid and surface interface, $\boldsymbol{A}$, otherwise known as the adhesion

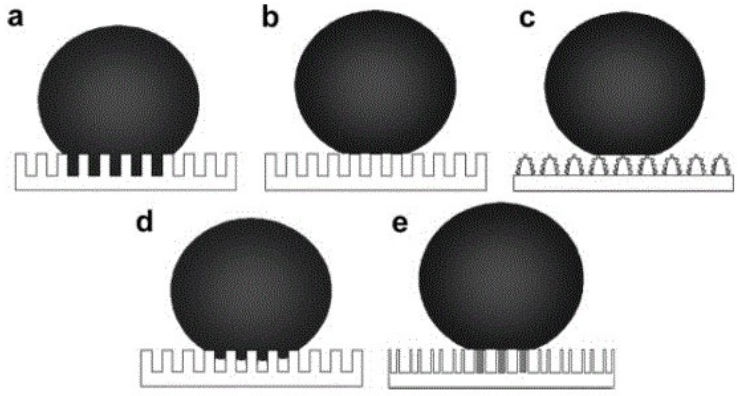

Figure 4.1: Different states of superhydrophobic surfaces: a) Wenzel's state, b) Cassie's superhydrophobic state, c) the "Lotus" state (a special case of Cassie's superhydrophobic state), d) the transitional superhydro- phobic state between Wenzel's and Cassie's states, and e) the "Gecko" state of the PS nanotube surface. The gray shaded area represents the sealed air, whereas the other air pockets are continuous with the atmo- sphere (open state). Reproduced from [164]

tension, by the Equation 4.2:

$$r \times A = S \times cos\theta \tag{4.2}$$

where $\boldsymbol{r}$ is the roughness factor of the surface [167]. The roughness factor is directly related to the morphology of a surface with higher $\boldsymbol{r}$ correlating to a higher contact angle θ. A "change in surface energy and adhesion tension may result from (1) a difference of crystal structure, (2) a difference in the amount of adsorbed impurities, and (3) the formation of a highly roughened or pitted surface" [167]. For example, another crystallographic plane would differ in surface energy; an new crystal would alter adhesion strength, and adsorbed impurities could decrease the surface area and surface energy, these impurities could also potentially subject the droplet to polar or nonpolar interactions [167]. Ma et al showed that decreasing an electrospun fiber's diameter, within a nanofiber mat, changes the roughness factor and can monotonically increase the contact angle up to 155°[106].

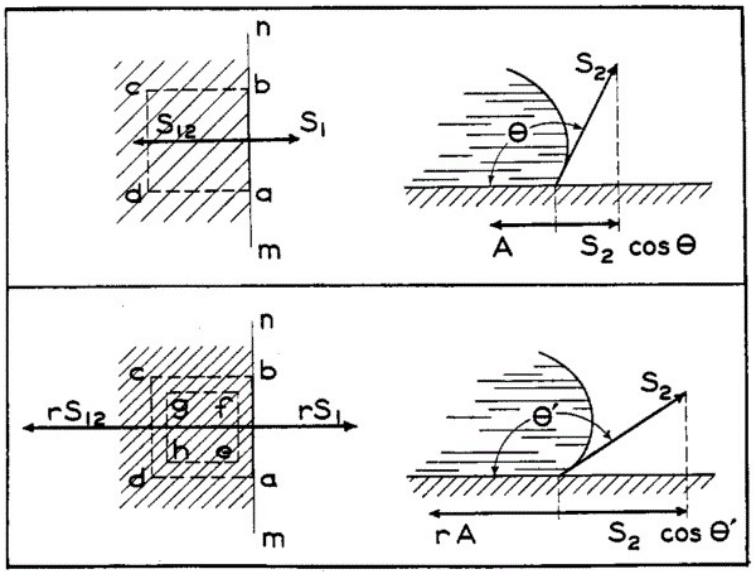

Figure 4.2: Vector Relations of Surface Forces. (*Above*) Solid surface smooth. (*Below*) Solid surface rough. Reproduced from [167]

The most widely used method of measuring contact angle is the use of optical recording equipment such as a goniometer which takes a high resolution snapshot and uses image processing software to calculate a contact angle based on sessile drop method [84]. The measurement is taken at the Young's contact angle; the point at which the solid surface, liquid droplet, and air meet as seen in Figure 4.1.

Other contact angle measurements include sliding angle (the angle at which a droplet on a tilted surface will become mobile) and contact angle hysteresis (comparing the advancing and receding contact angles when adding and subtracting liquid) [106].

The last property fitting a proper adsorbent material is the ability to recover or destroy the sorbent, depending on the circumstances. Recovery can include a variety of methods. Heating and "distillation is suitable for removal of valuable pollutants or those with low boiling points" [21]. "On the other hand, for precious or non-flammable

pollutants with high boiling points, squeezing is an attractive alternative method" [21]. To permanently remove "flammable and useless pollutants, combustion is a good choice" [21].

4.1.3 Other Types of Materials

Some example materials that display selectivity using oleophilic and hydrophobic surfaces are carbonized fir fibers[77], MnO2 nanowires, mesh films, carbon nanotube sponges, filter paper, and conjugated polymers [181]. Though they achieve efficiency using their selective surfaces, these materials often require costly precursors and complex synthesis methods that impact their potential for scalability.

4.2 Carbon Foams and Sponges

Here, a brief review and history of sorbent materials and techniques used in the synthesis of porous carbons used in oil sorption is presented for the reader.

4.2.1 History and Synthesis Techniques

Graphite was recognized as a sorbent material for oils beginning with the work of Masahiro Toyoda and Michio Inagaki [159, 161, 77]. By etching alpha stacked graphite with sulfuric acid for exfoliation, the increase in surface area allowed the sorption of heavy oils, such as crude oil, as well as less viscous class A and Class B oils [161]. The exfoliated graphite (EG) is also referred to as expanded graphite due to the increase in interplanar distance between the graphene sheets from 3.35Å to 4.3Å [166] which may be responsible for the growth in surface area. These expanded graphite sponges were also capable of

compression to recover the sorbed oil and achieved a sorption of oil equal to as high as 86x the mass of expanded graphite used [159]. Toyoda et al also noted that with increasing bulk density of the material, a decrease in sorption was observed. To increase the sorption then, a lower bulk density would be required, however the experimenters approached a limit of 5 kg/m^3 using the sulfuric acid method of exfoliation. Although the exfoliated graphite could recover the oil by compression, retrieving a maximum of 80% of the oil sorbed, the material deteriorated quickly and could not be used more than once. The BET surface area of the EG was 60 m^3/g. When comparing pore sizes of the material, it was found that 0.02 m^3/kg was the optimum size, below this volume the mesopores (<50nm diameter) and micropores (<9nm diameter) were too small to contain the large and bulky polymer chains characteristic of oils [159] and in fact heavy oil sorption occurs most regularly in pore sizes 1-600μm in diameter, but also dependent on the viscosity of the oil [77]. However, by switching to a suction method using a pump and filter, up to 60-70% of the oil was recovered, permitting the material to be reused without degradation with the exemption of heavy C-grade crude oil.

Graphite Oxide Reduction Hengchang Bi and company reduced graphite oxide to graphene oxide, producing a "spongy graphene" [20] with a contact angle of 114°and were the first to show that other petroleum products and organic solvents could be sorbed by these carbon foams. Their success was an example to later researchers[20, 66, 174] who used commercially available polyurethane sponges as substrates to coat layers of graphite oxide and reduce the sheets to graphene, an example of which is shown in Figure 4.3. Other researchers [20, 75, 109, 182, 26] have utilize Hummer's method.

Hummer's Method Starting with graphite flakes, sodium nitrate and sulfuric acid are mixed at freezing temperature (0°C). While stirring, potassium permanganate is added to the suspension, and after enough time passes, water is slowly added to the resulting paste "causing a violent effervescence" [75] during dilution. The solution is treated with hydrogen peroxide to reduce any residual permanganate and manganese dioxide to manganese sulfate. Thus, from graphite oxide, graphene oxide flakes can be produced.

4.2.2 Types of Carbon Foams

Since Toyoda and Inagaki's initial experiments with expanded graphite [160], their findings inspired researchers to look into other carbon structures as sorbents as well as methods of synthesizing graphite sponges by the "top-down" and "bottom-up" approaches. Top-down methods include the use of common polyurethane sponges as substrates for growth of hydrophobic materials while keeping their inherent flexibility and ability to be reused over many cycles as seen in Figure 4.3. Materials like carbon nanotubes were explored and displayed promising oleophilic properties [106, 92], along with graphene [20]. Researchers eventually began to synthesize carbon nanotubes or graphene onto pre-existing substrates in an effort to provide easy methods to implement and scale up production for later manufacturing. Chee Huei Lee et al grew vertically aligned CNTs onto prefabricated stainless steel mesh substrates which exhibited superhydrophobic and superoleophilic selectivity [92]. Another top-down methods include the decomposition of sponges in order to introduce hydrophobic properties. Reticulated Vitreous Carbon is one such material which is made from carbonized polyurethane impregnated with phenol and furfuryl alcohol and exhibits a honeycomb-like structure [77]. A separate methods is the impregnation of polyurethane

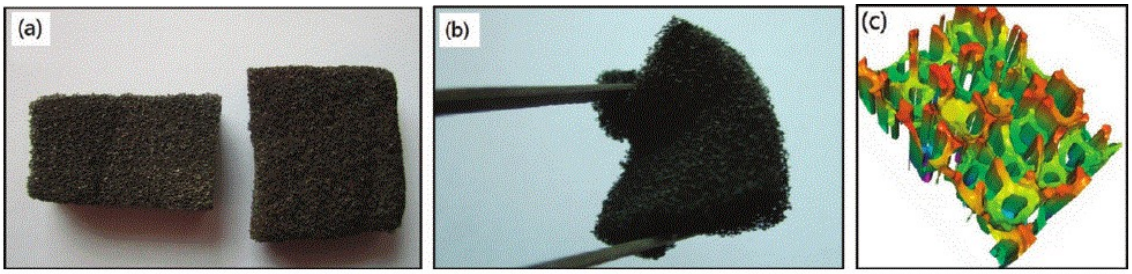

Figure 4.3: An example of polyurethane as substrate for hydrophobic and oleophilic functional groups. (a) Optical image of the as-prepared sponges. (b) A piece of sponge deformed by tweezers. (c) Three-dimensional configuration of the sponges. Reproduced from [181]

with poly(amic acid) which leads to imidization to create a polyimide, polyurethane is burned away, leaving the polyimide with a polyurethane structure. Lastly, the templating of tar pitches and other highly viscous polymers with impregnated particles can be used to control the cell size of the bulk structure. An example is the impregnation of tar pitches with SiO_2 spheres of known size, the subsequent carbonization of the precursor and molds the carbon foam around the spheres, which can then be etched away later [77].

Bottom-up methods refer to growth of a porous substrate from precursor monomer units such as the carbon foam explored in this work. It is thought that by exhibiting control over polymerization, greater control can be gained over the bulk morphology and properties such as porosity and specific surface area. Natural polymers and carbohydrates such as cellulose, starch, and chitin have also been investigated as potential precursors for these porous carbon materials [47, 181, 163]. In these types of materials, pore volume correlates with sorption mass [77]. Oil will displace water already sorbed into expanded graphites, but not completely, water might block smaller pores that oil cannot get into, therefore micro and meso pores with higher volume are desired [77].

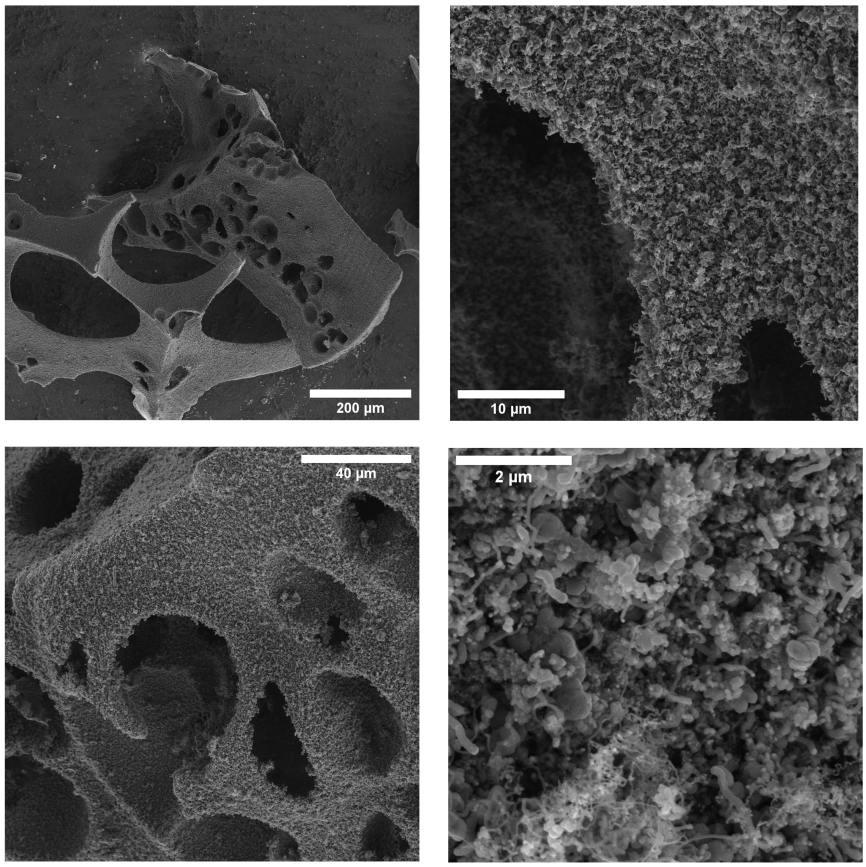

Figure 4.4: Hierarchical Carbon Foam designed to retain oil capacity as well as repel water sorption. All SEM micrographs are of the same sample, albeit at different magnifications

4.3 Oil Sponge

A hierarchical carbon foam was designed in order to provide enough capacity in the foam for oil sorption as well as synthesize MWCNTs on the surface of the foam in order to include hydrophobic properties in the foam.

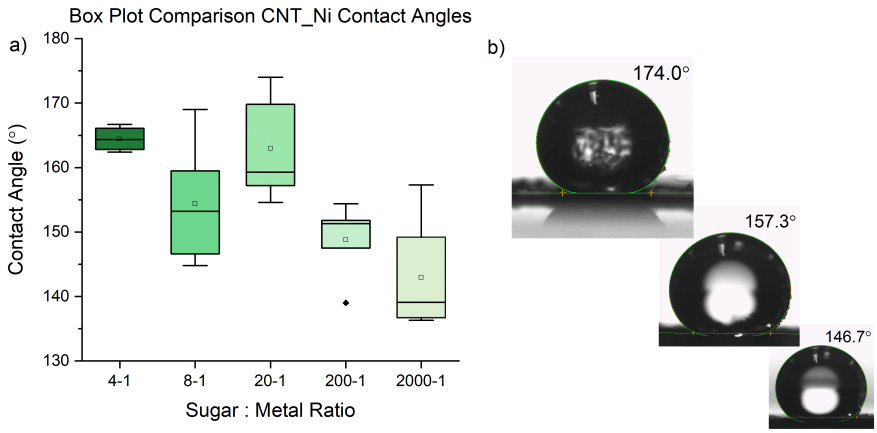

Figure 4.5: Box plots in a) show the distribution of contact angles measured for 4-1, 8-1, 20-1, 200-1, 2000-1 sugar to Ni ratios. b) demonstrates the variety of contact angles measured by goniometer

4.3.1 Synthesis and Procedure

Hierarchical carbon foams were designed by annealing Ni carbon foam as in Section 3.2.1. However, when milled using mortar and pestle, crushed powder was sieved between a 500μm and 100μm mesh. The carbon foam chunks that were milled to this specification were then exposed to CVD treatment for the growth of MWCNTs in the same conditions as Section 3.2. The same sugar to Ni ratios were chosen to test the affect of CNT growth on hydrophobicity. This size was chosen as small enough to maximize the surface area of hierarchical foams as well as large enough to retain oil.

Contact Angle CNT coated carbon foams were used to coat a glass slide and contact angles measured using goniometry. Water was dropped in 10μL increments onto coated slides and angles recorded using Sessile Drop fitting. Figure 4.5a shows box plot comparisons of the contact angles measured for increasing ratio of Sugar - Ni. Low ratios of Sugar - Ni

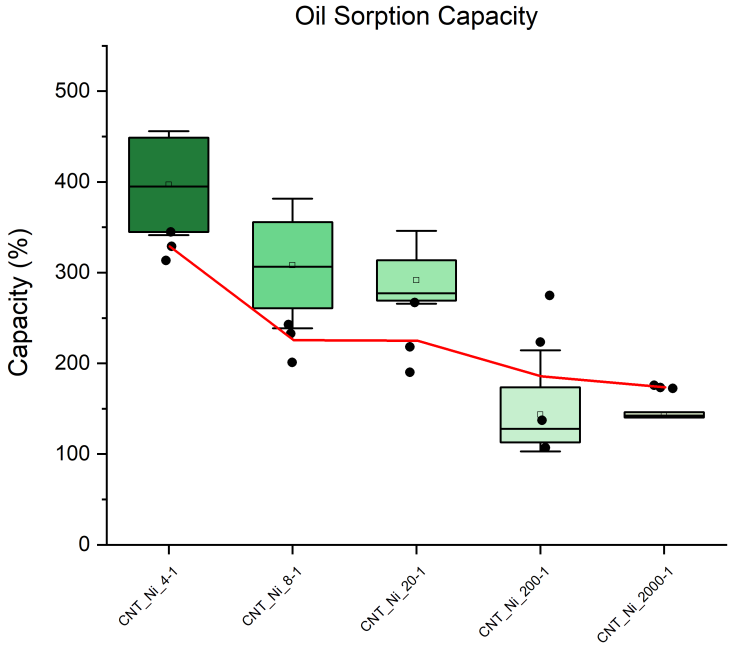

Figure 4.6: Oil sorption measurements of the hierarchical CNT carbon foam. Box plots of the measurements are presented. The red line denotes the average of the oil sorption for annealed foam chunks with particles, before CVD treatment

contain more metal content and produce CNT's with diameter ranging from 25nm - 48nm. Higher ratios of Sugar - Ni contains CNTs of similar tube diameter, but frequency of CNT growth and availability is significantly decreased. This is suggested in Figure 4.5a where a negative trend follows increasing Sugar - Ni ratio. Contact angles for 4-1, 8-1, and 20-1 ratios demonstrate superhydrobicity, displaying average contact angles of 164.5°, 154.4°, and 162.9°respectively; all of which exceed the definition of >150°[164].

Oil Sorption Capacity The oil sorption capacity for Ni-carbon foams treated with CVD synthesis was tested with a vacuum filtration set atop an Erlenmeyer flask with vacuum nozzle.Filter paper was placed in the filter holder and saturated with oil. Mass of the

oil saturated filter paper was measured and subtracted from the mass with carbon foam particles, as well as from carbon foam particles saturated with oil. Figure 4.6 displays a box plot chart of the mass percent the CVD treated carbon foam can absorb. The red denotes a baseline oil sorption of carbon foams without CVD treatment. It should be noted that the size of the sieved carbon foam is important to the oil capacity, and larger particles sieved in the 2mm to 500μm rage would retain more oil. A systematic study to find an optimal carbon foam particle size is suggested in order to maximize oil sorption with hydrophobicity.

Chapter 5

CNT Foam Electrode

In this chapter, the potential use of MWCNT coated foams for use in electrochemical double-layer capacitors (EDLCs) is presented. Starting with a brief review of electrochemistry, care is taken to explain the differences between EDLCs and batteries. Particular attention is paid to carbon materials for electrochemical energy storage and finally a MWCNT coated carbon foam is used in the construction of a symmetrical cell. Electrochemical characterization by cyclic voltammetry is used to describe the potential for carbon foams to be used as EDLCs.

5.1 Electrochemistry

Electrochemistry is the science of electron transfer across a solution-electrode interface and refers to all chemical reactions where electrons are reactants or products of the reaction, thus requiring or producing current, respectively. Most energy storage devices rely upon electrochemical reactions to store charge within their active materials; batteries and

capacitors are governed by these principles. An electrochemical device consists of parallel metal plates used as current collectors, active electrode materials to store charge, and an electrolyte medium which allows ions to travel from one electrode to the other. Additional components include a separator to keep electrodes from making contact and creating a path for electrons to travel directly from electrode to electrode, shorting the device; additives are used to increase the electrolytes wetting ability, safety, and cycle life. Charges are carried across the device by electrons and ions and the flow of electrons is called current. A positive potential bias, or voltage, is applied to one electrode (cathode) and a negative bias to the opposite electrode (anode). Negatively charged electrons are attracted to the positive electrode and travel from the negative electrode, through the metal current collector, and to the cathode. At the cathode they are stored at the surface of the active material where they attract positively charged ions in the electrolyte solution. The positively charged holes, or empty electrons orbitals, in the anode attract negatively charged ions in the electrolyte. These charged ions layer onto the surface of electrodes (inner Helmholtz layer) and can attract ions of the opposite charge creating a second layer (outer Helmholtz layer); this mechanism is called double layer capacitance, and this storage of charge is through electrostatic forces only.

Another form of electron transfer is through reduction and oxidation, or Redox, reactions. In this case, chemically active molecules or solids react with electrons to reduce (gain electrons) or oxidize (lose electrons). The electrons lost during oxidation at the anode's active material are then conducted through the metal current collector and travel to the cathode where another molecule or material is reduced, storing the charge. As ions and

electrons travel from one electrode to another, they are enacting the equations developed by Nernst, Butler-Volmer, and more to explain the relationship between the kinetics of the electrochemical reactions, current, and voltage.

The difference between these two methods of electron transfer is the difference between the inner workings of capacitors and batteries and will be further developed below.

5.1.1 Thermodynamics

Thermodynamics can help predict if, and at what potential, a reaction will take place. A thorough understanding of thermodynamic principles is thus required for expertise in electrochemical systems and will be explored here. Imagining two metallic species, a chemical reaction between materials A and B is represented by the expression:

$$A + B \longrightarrow AB \tag{5.1}$$

The thermodynamic driving force of this reaction is the difference between the sum of the formation product's Standard Gibb's Free Energy $\Delta G_f{}^\circ$*(prod)* and the sum of standard free energies of the formation reactants $\Delta G_f{}^\circ$*(react)*:

$$\Delta G_r^\circ = \sum \Delta G_f^\circ(prod) - \sum \Delta G_f^\circ(react) \tag{5.2}$$

where $\Delta G_r{}^\circ$ is in Joules (J) per mole and $1J$ is the product of 1 Coulomb (C) and one Volt (V). For an electrochemical reaction to take place within an electrochemical cell, flow of ions and electrons must take place. For a flow of ions to proceed, there must be a concentration gradient within the cell. If there is a blockage of either ions or electrons, the reaction will cease. If the external circuit is open, reactions will also cease because electrons cannot

travel through the circuit. When a circuit is open there must be a force balance upon the chemical driving force of the charged ionic species in the electrolyte. This balancing force is an electrostatic driving force in the opposite direction. The chemical driving force is known as the Gibbs free energy per mol of reaction ΔG_r° and is the difference in chemical potential of the two electrodes. This is determined by the difference of the Gibbs free energies of the products and reactants if a hypothetical reaction between the electrically neutral materials in the electrodes were to react chemically. The Gibbs free energy of species i in phase j can be defined as:

$$\Delta\mu_i = \Delta G_j \tag{5.3}$$

where $\Delta\mu_i$ is the chemical potential of species i which is inherent due to the concentration gradient in the cell. Because the chemical driving force is balanced with an electrostatic force, the following expression is satisfied:

$$\Delta\mu_i = \Delta G_j = -n_i F E \tag{5.4}$$

where n is the charge of the ion, F is the Faraday constant (F=96500 $C/$mol) or the charge of a mole of electrons, and E is the electric potential also known as the electromotive force. Denotation of a superscript indicates the standard state conditions:

$$\Delta\mu_i^\circ = \Delta G_j^\circ = -n_i F E^\circ \tag{5.5}$$

The equilibrium constant of the reaction is given by:

$$RTln(K_{rxn}) = \Delta G_j^\circ = -n_i F E_{rxn}^\circ \tag{5.6}$$

R is the Gas constant, and T is the temperature, K_{rxn} is the equilibrium constant and is the ratio of the chemical activity of the oxidative to the reductive species i:

$$K_{rxn} = \frac{a_i^r}{a_i^o} \tag{5.7}$$

The free energy of the reaction is related to the equilibrium constant by:

$$\Delta G_j = \Delta G_j^\circ + RTln(K_{rxn}) \tag{5.8}$$

and is equivolent to:

$$\Delta G_j = -nFE_{rxn}^\circ = \Delta G_j^\circ + RTln(K_{rxn}) \tag{5.9}$$

which can be rearranged and simplified to the Nernst equation:

$$E = -\frac{\Delta G_f}{nF} = E^\circ + \frac{RT}{nF}ln(K) \tag{5.10}$$

$$E = E^\circ + \frac{RT}{nF}ln\left(\frac{[Ox]}{[Red]}\right) \tag{5.11}$$

where E°is the standard redox potential, measured at standard state. The Nernst equation directly relates the cell voltage to the concentrations of the reduced and oxidized species. Furthermore, it can relate the cell voltage to the Gibbs free energy of formation of products of electrochemical reactions and their chemical activity.

In any Faradaic cell, two reactions are taking place: reduction and oxidation which take place at the cathode and anode, respectively. We can therefore define a potential for the reduction and a potential for the oxidation:

$$E_c = E_c^\circ + \frac{RT}{nF}ln\left(\frac{[Ox]_c}{[Red]_c}\right) \tag{5.12}$$

$$E_a = E_a^\circ + \frac{RT}{nF}ln\left(\frac{[Ox]_a}{[Red]_a}\right) \tag{5.13}$$

where E_c and E_a is the potential in the cathode and anode, respectively. The total cell potential E_{cell} can then be determined by:

$$E_{cell} = E_c - E_a \tag{5.14}$$

E_{cell} is a relative potential, not absolute, meaning a researcher who is communicating a cell voltage reading must also communicate its reference electrode. The use of a reference electrode in an electrochemical cell is commonly referred to as half-cell testing. The standard hydrogen electrode (SHE) is a common reference electrode, though in the case of lithium ion battery research, Lithium chips are also commonly used during half-cell testing. The electrode of interest is referred to as the working electrode (WE) and the opposite can also be referenced to as the counter electrode (CE). When paired with an electrode with more positive potential, an electrode will be oxidized, and vice versa; when an electrode is paired with a more negative electrode, it will be reduced.

5.1.2 Kinetics

The rate at which chemicals are reacting is referred to as kinetics and is usually measured with reference to the quantity of reactant being consumed or product being produced per unit time (mol/s). In the case where electrons are considered a reactant or product, the reaction can also be evaluated by measuring charge (C=coulombs) per unit time, otherwise known as amps ($1A = 1C/\text{s}$). Here we consider the simplest case with a single electron transfer reaction between two species O and R in a reducing step and oxidizing step, respectively:

$$O + e^{-1} \xrightarrow{k_{\text{red}}} R \tag{5.15}$$

$$R \xrightarrow{k_{ox}} O + e^{-1} \tag{5.16}$$

The current which is produced by oxidation i_O and the current produced by reduction i_R can be modeled by the following expressions:

$$i_O = FAk_{ox}C_R \tag{5.17}$$

$$i_R = -FAk_{red}C_O \tag{5.18}$$

These expressions relate the respective currents to the electrode area (A), concentration of reactant (C_O or C_R), rate of electron transfer (k_{red} or k_{ox}) and Faraday's constant F. It is in this way that the rate of electron transfer can model the rate of oxidation. The oxidative current i_O is positive and the reductive current i_R is negative by definition. This allows researchers to identify in which direction current is flowing across an interface.

5.1.3 Batteries

Batteries use electrochemical Redox reactions to transfer and store charge, a method referred to as Faradaic. Molecules in the electrolyte solution react with and transfer electrons across the double layer to the electrodes. When electrons transfer from one molecule to another, there is a change in oxidation state; when this happens in a solid or crystalline material, there is a change in phase. These Redox reactions can involve 1-3 electrons per atom in a phase or molecule and is the reason battery materials can store more charge and have more energy density (mAh/g) than a capacitor. Like capacitors, batteries also exhibit a double layer capacitance, however this only contributes 2-5% of the total charge stored in a battery[31]. Furthermore, this dependence on electrochemical reactions means the overall current generated is also dependent on the kinetics of these reactions

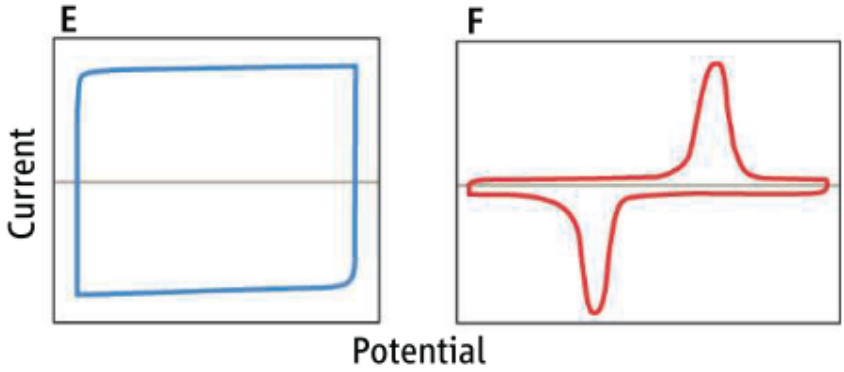

Figure 5.1: Cyclic voltammograms distinguish a capacitor material where the response to a linear change in potential is a constant current (E), as compared to a battery material, which exhibits Faradaic Redox peaks (F). Modified from [146]

and the diffusion of reactants towards each other and products away from each other. This slows down the electron transfer or current, and limits the specific energy (Wh/g) of a battery. The electrons taking part in these Redox reactions are typically from the valence shells or outer orbitals of the participating reactants, but travel through the conduction band of the supporting current collectors. The applied voltage raises the Fermi-Level of metal current collectors above that of the Lowest Unoccupied Molecular Orbital (LUMO) allowing an electron that was in a conduction band with too low energy, and thermodynamically blocked by the Highest Occupied Molecular Orbital (HOMO), to now transfer to the reactant molecule or crystalline material. Batteries also require more energy to reach the same voltage as a capacitor because they require an Overpotential. An overpotential (η) is the voltage applied to a chemical past the standard potential (E°) at which an electrochemical reaction takes place. This additional voltage is required to produce a large amount of reactions and current to flow. With the exception of intercalation compounds,

the Gibbs Free Energy, the thermodynamic equivalent to voltage, remains the same for a battery at all states of charge. Because of the reliance upon Redox reactions, molecules and phases of materials are constantly undergoing irreversible chemical processes and this leads to a battery's short cycle life compared to a capacitor. Intercalation compounds are usually crystalline materials with a layered structure. The phase transformation undergone occurs when an ion inserts itself between these layers, changing the chemical composition of the crystal and altering the size of the unit cell, but not disastrously so. But because the chemical composition of the intercalation material changes over time, the voltage is variable as in the case of Lithium Ion battery materials [110, 83, 97]. Electrons are stored either in the conduction band of the intercalation material or in the valence band of an atom in the crystal by a Redox reaction. Fortunately the unit cell of the crystalline material is not altered too drastically, resulting in their cycle life usually being longer than that of non-intercalation or "alloying" electrode materials [74].

These characteristics are also reflected in the battery's Cyclic Voltammetry (CV) profile. A certain voltage, or standard potential, will enable reactants to overcome the energy barrier to proceed with a reaction and produce current. The plotting of voltage on the abscissa and the corresponding current on the ordinate produces a CV profile. These CV profiles are unique to electrochemically active molecules and materials, thus leading to their use in identification and characterization. The CV profile of a battery material will be characterized by peaks and valleys where a standard potential will correspond with a current, signaling the onset of an electrochemical reaction. When an overpotential is applied, the reaction kinetics increase, creating a peak in current. The peaks and valleys

are also usually separated by 0.1V-0.2V [31]. When an oppositely charged potential is applied, the voltage switches. However, while at a standard potential, that reaction will still take place, and produce current, take oxidation for example. It is not until the voltage sweep passes the standard potential that anodic current stops being produced and cathodic current of the opposite reaction can be produced, or reduction in our case. This is not the case in capacitors.

5.1.4 Capacitors

Investigation into electrochemical supercapacitors is popular because of their large power density and long lifetime (up to 10kW/kg) compared to lithium-ion batteries and their energy density when compared to dielectric and electrolytic capacitors [179]. Although they are sought after for their power density, capacitors are also ideal for low energy use cases like memory and backup energy. There are three main capacitor systems which include: double layer capacitors, pseudocapacitors, and hydrids of the two.

Traditional double layer capacitors use non-Faradaic charge transfer to store electrochemical energy, in other words, they do not rely on Redox reactions like batteries. This inherently limits the amount of charge stored to the number of ions that can be adsorbed onto the surface of an electrode material. These ions layer onto the electrodes' surface creating the Helmholtz double layer and are held in place by a balancing electrostatic force. The electrostatic force is the charge of the electrons in the electrode when positively charged ions are used or electron holes when a negatively charged ion is used. The electrons or electron holes are stored in the delocalized metal or carbon conduction band of the electrodes. This

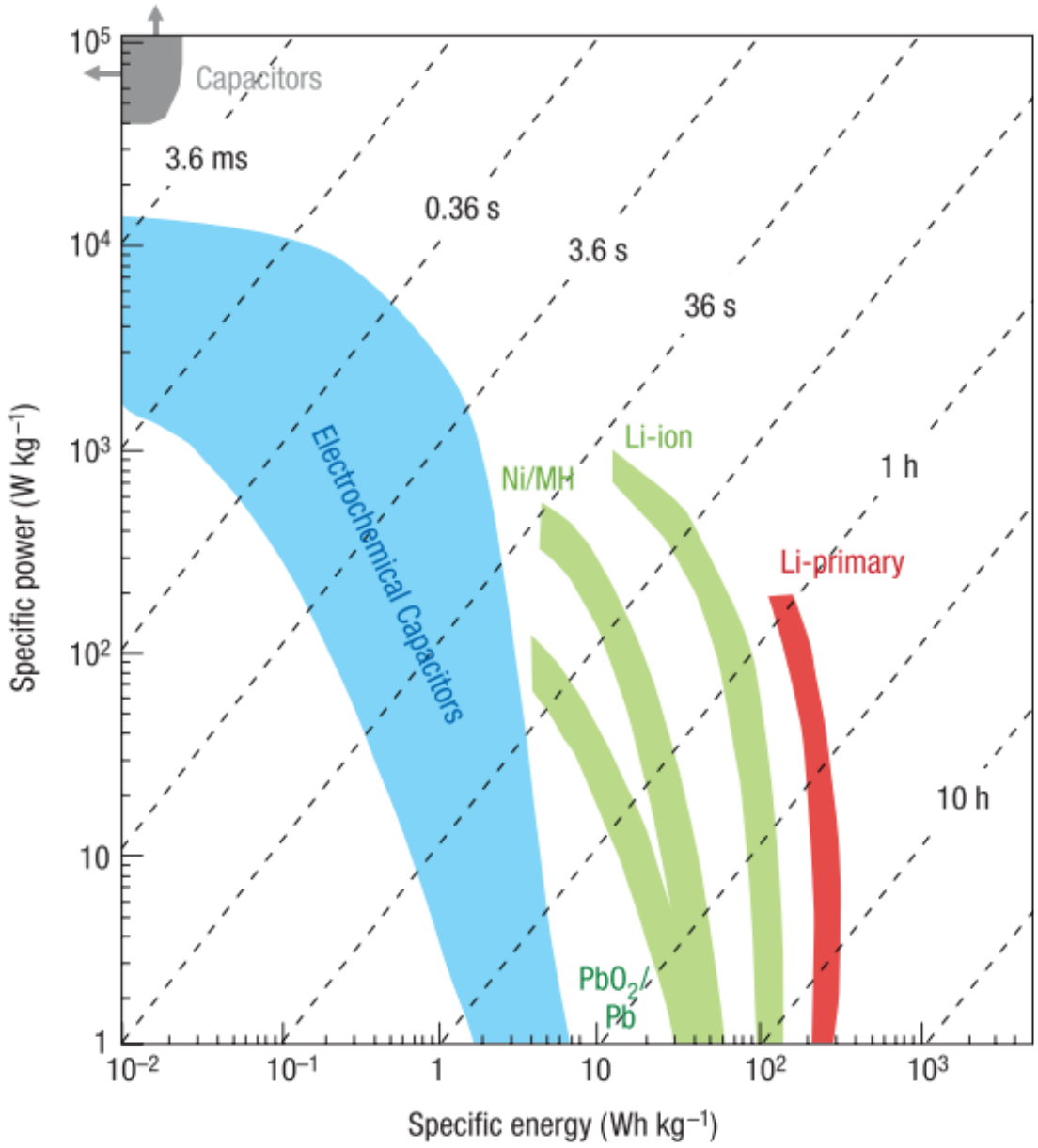

Figure 5.2: Specific power against specific energy, also called a Ragone plot, for various electrical energy storage devices. If a supercapacitor is used in an electric vehicle, the specific power shows how fast one can go, and the specific energy shows how far one can go on a single charge. Times shown are the time constants of the devices, obtained by dividing the energy density by the power. Reproduced from [133]

simple system of balancing forces is responsible for capacitors' long cycle life. All that is required of a capacitor is the diffusion of charged ions from the bulk electrolyte to the surface of the electrode, so no phase, compositional, or chemical changes take place. Unlike battery electrodes that undergo mechanical stresses upon intercalation or "alloying" reactions, virtually no mechanics are to be considered. Mesopores contribute the most to capacitance in electrical double-layer. The absence of mechanical, chemical, and thermodynamic stresses leads to a highly reversible system.

Since there is no electron transfer from ions through the electrolyte to the electrode due to Redox reactions, capacitors have faster kinetics than battery materials. It is also the reason capacitors enjoy higher power density than batteries. The electrons stay outside the double-layer and do not react with the electrolyte. Because of this, it takes only half the energy to charge a capacitor to the same voltage in a battery where the voltage changes with the state of charge. When the voltage switches in a capacitor, the current immediately switches sign, from cathodic to anodic or vice versa.

However the lack of Redox reactions is also detrimental to a capacitor's energy density. Only an average of 0.18 electrons per atom of the metals or carbons in an electrode will be used to balance the charge of an ion. This pales in comparison to the 1-3 electrons per atom which take part in Redox reactions that define a battery's electrochemistry.

To combat this effect and bridge the gap, pseudo-capacitors have been employed. In pseudo-capacitors, Redox reactions take place in the capacitor, though the materials are usually small nanoparticles of battery materials, where the bulk of the electron transfer takes place. Compared to batteries the power density increases, but they have slower

kinetics and less power density than double layer capacitors. Porous carbons do exhibit a small, but significant pseudo-capacitance due to surface impurities such as oxygen [31, 146]. Double-layer capacitance still takes place though the contribution to overall capacity is lower.

5.2 Carbon Electrodes

Various carbon materials have been utilized in the production of electrochemical energy storage devices. Carbons provide a high surface area conductive additive that is produced from a readily available precursor in the form of coconut shell waste and selected woods. Activation procedures are implemented in order to increase the micro-porosity and the meso-porosity of the carbon allowing the control over pore size and shape by careful selection of cellulosic precursors, temperature, CO_2 flow rate, and impregnation of salts for post treatment etching. Presented here is a brief review of the electrochemistry and variety of carbon electrodes.

5.2.1 Carbon Electrochemistry

The surface properties and functionalities of carbon materials are largely determined by the residual valencies or dangling bonds which lead to adsorbed or chemisorbed oxygen. These terminal valencies can lead to several O-surface functionalities. In the context of graphite, carbon's electronic conductivity is asymmetric in nature, having good conductivity along the basal plane and therefore high conductance because of delocalized conjugated pi-bonds, but not so great conductivity normal to the layered structure and

therefore less conductance. This is why graphite usually has better than amorphous carbon powders. However, dangling bonds give rise to a surface free-radical character, and therefore edges are more reactive to oxidation than the conjugated carbons and these edges create O-surface functionalities, as well as others [31, 22]. Because these functionalities are at edges, their contributions to the electrochemistry tend to scale with particle size or specific surface area of the active carbon material. They also gives rise to pseudo-capacitance/redox reactions. These surface functionalities can be detected by means of titration with acids and bases depending on the type of terminal group as well as Electron Spin Resonance (ESR).

Quinonoids are oxidized derivatives of conjugated, benzene-like compounds. They exhibit moieties such as phenols, ketones, carboxylic acids, and lactones among others as seen in Figure 5.3 [144, 22]. The presence of these polar surface functionalities can also influence the wetting angle, or contact angle, of the carbon with an electrolyte, as in the case of aqueous electrolytes. Electrochemical oxidation of carbons increases their wettability due to the increase in hydrophilic O groups. Electrochemical reduction has the opposite effect. Studies suggest that as voltage is increased from 0.5V-3.0V, an increase in carbon oxidation takes place, concurrent with the detection of quinone type moieties [31]. Other edge groups can form as well, for example: when exposed to F_2 gas or intercalation materials with Li, Br_2, and K.

The capacitance, or charge stored at a surface when a voltage is applied, depends on pore accessibility but surface moieties can alter them. Generally, graphite have a capacitance between 12-70μF/cm^2, carbon blacks have low capacitance between 5-10μF/cm^2, and activated carbons have 10-15μF/cm^2. Porosity is extremely important for EDLCs. Highly

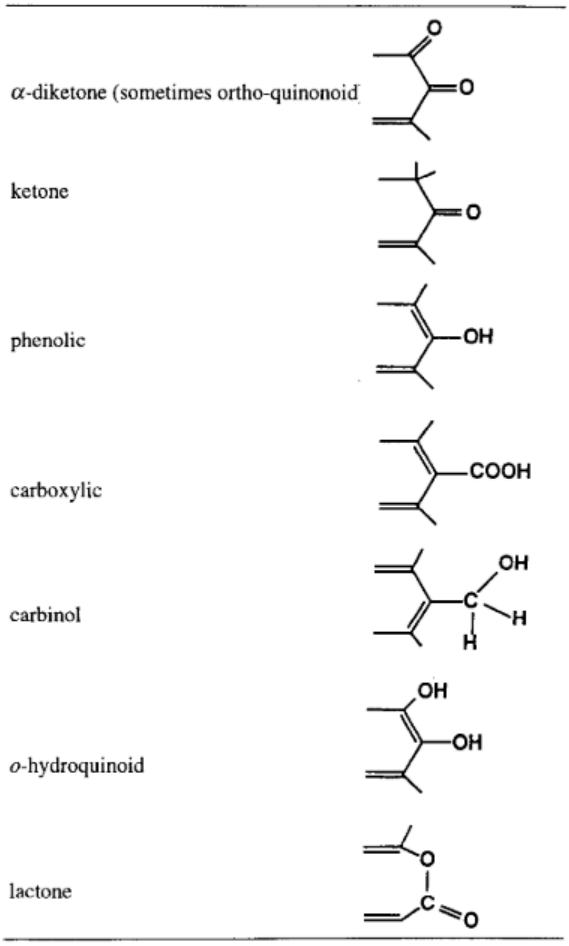

Figure 5.3: Summary of Surface Functionalities at Carbon Materials. Modified from [31]

oxidized, ultramicroporous (<1nm) carbon materials show substantially lower double-layer capacitance at positive voltage than non-porous carbon surfaces. Ions can only penetrate the smallest pores after the depletion of their hydration shells [31]. Therefore, micro- and mesopores are desirable.

Semiconducting properties can be seen in carbon materials with low electronic conductivity because there is a distribution of charge carrier concentration (charge density) within the bulk of the carbon material, giving rise to a space charge inside the carbon-solution boundary. This leads to a drop in potential within the material, and a space charge capacitance is developed because the electrode potential depends on the space charge density. It behaves like an ionic diffuse-layer capacitance outside the carbon-solution interface, except for the dielectric constant of the medium in which the charges reside. Graphitic carbons would not be expected to exhibit semiconducting behavior, since free electron density is sufficiently large for such materials and their behavior ends up being is metallic, but semiconducting behavior has been seen on graphitic basal planes before [31]. Of course, differences in standard potentials between the graphite basal planes and the edges should arise which lead to differences in anion adsorption and this influence is scales with particle size and specific surface area. The state of oxidation can also determine the capacitance on a mass basis and influence self-discharge characteristics [116].

The carbon surface morphology can have multiple influences on electrochemical behavior. Intrinsic surface properties of a crystal face of the electrode material, along with the surface functionalities, determine the electronic work function, or minimum thermodynamic work needed to move an electron from a surface to a vacuum, with zero kinetic energy,

from the Fermi level of the electron energy distribution in the bulk material. Changes in the work function are related to changes in the surface dipole potential. The affect of the surface morphology can also have slight influences on the double-layer capacitance, especially with adsorbed anions. These forces must balance in order to store the charge. Heat treatments at high temperatures can induced graphitization in "soft" sp^3 carbons, changing the crystal structure and thus causing changes in specific surface area. Heat treatments can also reduce the oxygen quinonoid groups at the carbon surface. The removal of amorphous carbons goes a long way in increasing the cycle life of the capacitors and limiting self-discharge by reducing the amount of valencies that are present with sp^3 carbons.

Intercalation is both cations and anions is relevant to EDLCs, especially with graphitic carbons. The general oxidation takes place by forming a delocalized positive charge in the benzene-like rings of the graphene sheets with intercalation of anions. The sorbed anions retain some degree of solvation. A combination of phase change and electron transfer from the anions stabilizes the lattice.

5.2.2 Carbons for Lithium-Ion Batteries

In Lithium-Ion Batteries (LIBs), carbons are used for two purposes, first as a conductive additive to ensure contact with the active Redox material is attained, and second, as an active anode material itself [110, 83, 33, 11, 97, 74]. Carbons used for conductivity reduce the first cycle irreversible capacity loss. This is achieved when the carbon is heat treated at lower temperatures (500-700°C). This also improves the cyclability of the cell over time by minimizing surface functionalities that may react with the electrolyte. The conductive additive can be mixed in as a slurry, or coated onto an electrode material by

CVD synthesis. This is seen in cathode materials such as: lithium cobalt oxide (LCO), lithium manganese oxide (LMO), and lithium iron phosphate (LFP); in anode materials CVD coating by activated carbons is seen in: graphite, mesocarbon microbeads (MCMBs), and lithium titanate (LTO). In Si and SiO_2 anodes, graphene sheets have been used to encapsulate the particles in order to help with stress fractures associated with the large volumetric expansion of these high energy density materials in addition to increasing their conductivity.

As an anode material, graphite is routinely used for its ability to intercalate Li^+ ions between its graphene sheets. Upon lithiation, the interplanar distance between graphene sheets expands, and an overall charge balance is achieved with the Li^+. The solvated Li^+ must depart from its solvated electrolyte ligands at the edge sites of graphite, this in turn leads to the build up of the solid-electrolyte interphase (SEI), which has two main consequence. The first is the loss of electrolyte on the surface of the graphite. This can lead to internal resistance in the cell due to diffusion constraints through the SEI layer and a decrease in available solvent which decreases contact with the electrodes. The second consequence is beneficial. The build up of the SEI layer protects the graphite edges from constant expansion and reduces stress in the crystal structure at the same preventing more electrolyte from reacting with the surface functionalities present of the graphite edge. Overall this leads to an irreversible first cycle capacity loss and stability upon subsequent cycling. A decrease in the coulombic efficiency gradually robs the electrode of its capacity, mostly due to the break up and recreation of SEI layers[110, 83, 33, 11, 97, 74]. Additional carbon materials used as anodes include: graphitized materials prepared from cokes, car-

bon fibers, and MCMB, and also non-graphitic carbons derived from different resins. These materials have high charge rates (C-rates) and are desirable as LIB anode materials. For a more in depth study of carbon interactions with Li^+ ions, the reader is directed to the work of J.R. Dahn [33].

5.2.3 Carbons for Capacitors

Generally, the carbons to be considered for double-layer capacitors should have:

- 1) High surface area (>=1000m^2/g)
- 2) Good intra/inter particle conductivity
- 3) Good electrolyte accessibility to intrapore surface area
- 4) Free of impurities (Fe, peroxides, O_2) and surface quinonoid structures to minimize self-discharge

In order to obtain high capacitance, microporous carbon is recommended as the electrode material, but high rate performance cannot be expected; in other words, microporous carbons are suitable for use at a low current density. At increasing discharge density the capacitance of conventional carbon electrodes will decrease gradually. The current may be too large and the ionic resistance may block the entrance to the micropores [104, 179]. To have high rate performance, mesoporous carbon is desired, mainly because of the low diffusion resistance of electrolyte ions in the electrode, but micropores are needed to attain usable capacitance. Unfortunately, there has been no systematic study to optimize the combination of microporous and mesoporous surface areas for obtaining high capacitive performance.

The electrode precursor material is highly influential on the morphology, porosity, and surface functionalities that will be present in the carbon. Some precursors include: peach stone, furfuryl resin, saran, mesophase pitch, phenol-formaldehyde, cypress chip charcoals, seaweed, and coconut shells. Activated carbon fibers (ACFs) can be fabricated from pitches and phenol-resins. Polyacrylonitrile (PAN) PAN-ACFs compsites with a relatively large amount of mesopores show good rate performance with much smaller reduction in capacitance with increasing current density. For most zeolite-templated microporous carbons, very good rate performance is observed. They exhibit a high and almost constant capacitance of 160F/g even at a current density as high as 2A/g. This excellent rate performance was thought to be due to the three-dimensionally ordered and highly connected pores, giving a low ion-transfer resistance in micropores. Sugars and polysaccharides have been shown to polymerize and produce highly porous and graphitic structures with good conductivity for electrochemical supercapacitors as well [165, 163, 105].

Carbon nanotubes have been fashioned into capacitor electrode due to their high surface area. "CNTs have a relatively lower specific surface area but a higher electrical conductivity, higher charge transport capability, higher mesoporosity, and higher electrolyte accessibility. It is then desirable to combine activated carbons with CNTs to fabricate composites having the combined advantages from these two components. The resultant nanocomposites would possess an improved conductivity and an appropriate balance between the specific surface area and the mesoporosity, resulting in a higher capacitance than CNTs and a higher rate capability than activated carbons" [104]. In the case of SWCNTs, high conductivity is observed. When a "forest" of SWCNTs, usually grown from metal

nanoparticles deposited on a substrate, the tubes are close packed and microporosity is good. This can also be the case for mesoporosity in disorderly arrangements of CNTs. If the CNTs are intertwined and entangled with one another, porosity is naturally present in the void space between the tangled tubes and the surface of the tubes is accessible to the electrolyte. This is also the case in MWCNTs. However, for MWCNTs, the ease of synthesis come at the cost of conductivity. Semiconducting properties can be exhibited in MWCNTs. Fortunately, MWCNTs can cleave their caps upon nitric acid treatment, exposing the inner shells to intercalation processes that can further increase capacitance. For a comprehensive review on the use of CNTs as EDLC electrodes, the reader is directed to [104].

Currently available commercial supercapacitors are fabricated in a symmetric configuration where two identical capacitative electrodes (usually activated carbon) are used as both the positive and negative electrodes (Fig.1). In this design, the capacitor utilizes only one half (on an area basis, F/cm^2) or one fourth (on a mass basis, F/g) of one electrode's capacitance, resulting in a low energy density for the capacitors [104].

Typically, an asymmetric supercapacitor is constructed by replacing one of the capacitative carbon electrodes of a symmetric capacitor with a Faradic electrode made of electroactive materials including: electroactive polymers [179, 104], metal oxides (Bélanger et al., 2008 in [104]), or battery electrode materials (Pasquier et al., 2003 in [104]). Due to the infinite capacitance of the Faradic electrode comparing to that of the capacitative electrode, an asymmetric capacitor utilizes all (on an area basis) or half (on a mass basis) of the capacitative electrode's capacitance [104].

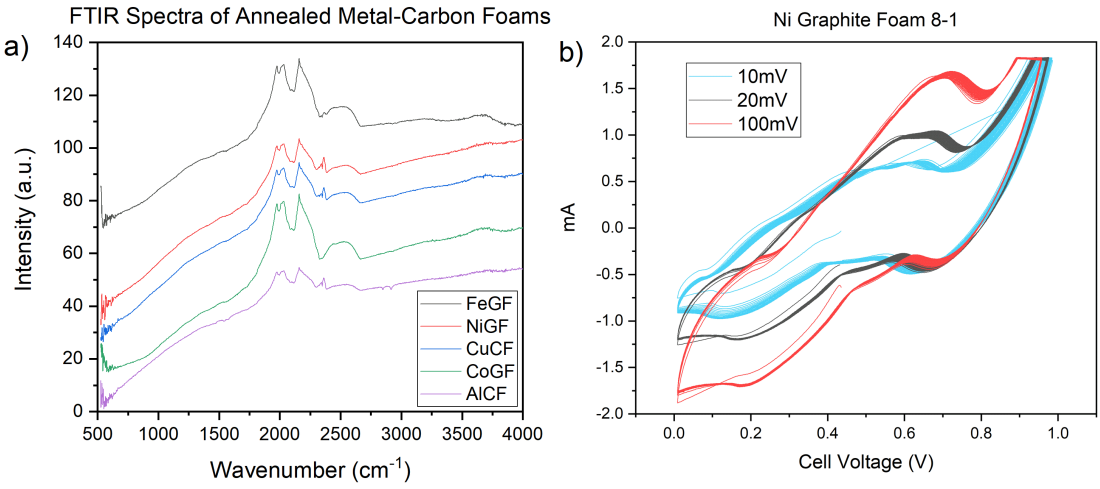

Figure 5.4: Cyclic Voltammagram of NiGF as active carbon material in an EDLC

5.3 Capacitor CNT Foam

The procedure described in Section 3.2 was co-opted for use in synthesizing <20μm sized carbon foam chunks with embedded Ni particles for the growth of MWCNTs. Pressure of the CVD process was increased from 100torr to 250torr to increase length of MWCNTs. Annealing pressure was held the same at 100torr during flow of Ar and H_2. The abundance of MWCNTs when using the 8-1 sugar to Ni ratio increases the surface area of the foam chunks and also creates porosity within the MWCNT matrix.

5.3.1 Capacitor Electrode

To test energy storage applications of the CNT foam, electrochemical double layer capacitor (EDLC) electrodes were constructed using CNT foam as active material. A slurry was made using 80% CNT foam derived from xylose and Ni nitrate in a 8-1 molar ratio, 10%

acetylene black, 7% polyacrylic acid (PAA) and 3% polyvinylpyrrolidone (PVP) by weight and dissolved in n-methylpyrrolidone (NMP). Electrodes were dried in oven at 100°C for 24 hours. Symmetrical cells were constructed using 1M $NaSO_4$ aqueous electrolyte and PVP was introduced into electrode slurry as wetting agent, without which the electrolyte was repelled by the electrode due to the hydrophobicity of the CNT foam. For comparison, another symmetrical cell was synthesized from NiGF without post processing CVD as in the case in Section 2. However this NiGF was made using xylose as the sugar, without PVA, and annealed at 1000°C. Electrode slurry components were kept the same as the CNT foam electrode.

5.3.2 Electrochemical Characterization

Cyclic Voltammetry is implemented to characterize the CNT carbon foam as an EDLC. For the NiGF, the CV profiles for 10mV/s, 20mV/s, and 100mV/s scan rates are presented in Figure 5.4b. In an EDLC, the CV profile should be rectangle in nature, reflecting the fast kinetics of the cell, and without peaks. Clearly Figure 5.4b displays electrochemically active peaks due to oxidation of the surface carbon. Cycle life of the cell was low, lasting only 10 cycles before falling below 80% coulombic efficiency or shorting at each scan rate. EDS spectra of the NiGF detected the presence of O as it did with each of the other metal-carbon foams. The nature of these O groups is still uncertain. FTIR spectra of the annealed metal-carbon foams shows the broad peak of COOH from 3000-2500cm^{-1} as seen in Figure 5.4a. The presence of carboxylic acid groups is expected due to the nature of the precursors and their oxidation during polymerization. However, these COOH groups may also be responsible for the oxidation in the NiGF cell. The use of carbon

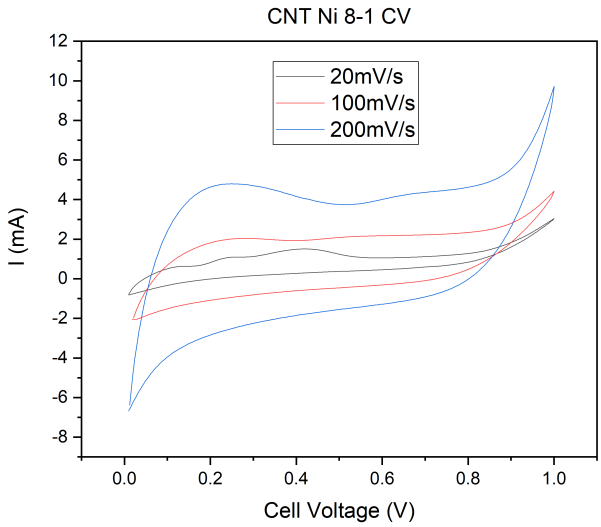

Figure 5.5: CV comparison of foam, before and after CNTs, with different electrolytes

activation procedures may also reduce the O content in the cell. Hydrogen gas can be used as well, but the hydrogenation of these carbons is not strongly bonded and these dangling bonds may react with electrolytes while in the cell.

Figure 5.5 displays the CV profile for the CNT foam synthesized from Ni-xylose carbon foam. A much more rectangular profile is exhibited and there is a decrease in the number of peaks. Peaks at the 0.01V and 0.9-1V range are still visible and may suggested there is still some O content present. The additional CVD synthesis to promote the growth of MWCNTs may contribute to a decrease in the O content of the carbon foams. During the process of CNT growth, acetylene may react with O-surface functionalities to decrease the content. FTIR is needed to confirm this hypothesis and should be conducted. The addition of the MWCNTs should also increase the specific surface area of the carbon foams and create additional porosity. The entangled MWCNTs do not create pores in the traditional sense,

however they do provide a porous network which is available for electrolyte to inhabit and a surface onto which the electrolyte can electrostatically adhere. BET surface area measurements are planned and will be included in the manuscript of this work. The use of Electrochemical Impedance Spectroscopy (EIS) is also planned in the electrochemical characterization of CNT carbon foam capacitors. In summary, the rectangular CV profile demonstrates the potential use of CNT carbon foams as a stable electrode material.

Chapter 6

Conclusions and Recommendations

Porous carbons have been used for a variety of applications and carbon foams represent an opportunity to begin utilizing bottom-up methods to design a macro-structured carbon from simple, cost-efficient precursors. The use of metal nitrates allows for the tailoring of these composites for specific applications. In this work we demonstrate the ability to synthesize metal-carbon foams by a simple oxidation and esterification process. The growth of metal particles originates from the nucleation of reduced metal cations in solution as in the case of Cu and Ag. For Fe, Ni, and Co, other methods of metal-oxide formation may preserve the cations in the gel-resin until exposed to a reducing atmosphere. In either case, metal particles are produced which can be further functionalized for specified applications.

In this work, the use of Ni and Co variations of the metal-carbon foam are used as substrates for the growth of MWCNTs and multi-layer graphene. The CNT-foams derived from Ni-carbon foams are further utilized as materials for oil spill recovery and electrochem-

ical capacitors. The CNT-foam showed high selectivity for oil sorption as demonstrated by the high hydrophobicity as measured by contact angle goniometry. The use of CNT-foams as electrochemical capacitors is also demonstrated by the CV profiles measured. These are only two applications derived from one metal being functionalized with MWCNTs. This same metal-carbon foam, along with the other variants can be co-opted for an enumerable amount of applications. Some of these will be listed below.

6.1 Recommendations

These recommendations will be presented based upon the potential applications. One or more metal-carbon foams may be able to provide a scaffold for these applications.

6.1.1 Catalyst Substrates

The use of Fe in ammonia catalysts is well documented and the temperature range for ammonia synthesis is between 400-500°C. This is below the graphitization temperatures found in literature and experimentation. The FeCF could potentially be used as a porous scaffold for ammonia synthesis without encapsulating the Fe particles. Carbon activation procedures could potentially be utilized to increase the specific surface area of the Fe-carbon foams while simultaneously exposing more Fe nanoparticles to reactant gases.

Copper particles have been utilized in the catalytic conversion of CO_2 to ethanol [152] using a graphene substrate. Perhaps a combination of the Co- and Cu-carbon foams could be used to synthesize a graphene-Co sponge coated with catalytic Cu nanoparticles.

6.1.2 Antibacterial Coatings

Cu, Ag, and ZnO nanoparticles have been demonstrated to disrupt the reproduction of microbial cells [10, 29, 37, 94, 124, 148, 176, 177]. Zn- and Cr-carbon foams have been synthesized by the group, though the work has not been presented here. ZnO-carbon foams should be easily procured. However, control over the particle size will be a deciding factor as to the viability of metal-carbon foams as antibacterial coatings or sorbent materials. The nucleation of micron-sized particles in Cu and Ag-carbon foams has been observed and several factors could be adjusted to study the effect of particle size including: sugar-metal ratio, annealing temperature, and annealing time.

6.1.3 Electrochemical Capacitors

The growth of MWCNTs on Ni-carbon foams for EDLC applications was presented in this work but can be further pursued. The hydrophobicity of the CNT-foam presents wetting problems with the electrolyte, so a change to organic electrolytes can be attempted. This would increase the voltage at which the capacitors operate, and completely change the chemistry in the device.

NiO nanoparticles have been shown to add pseudo-capacitance to a cell and increase the energy density. The use of nickel nitrate could be used to first anneal Ni nanoparticles and subsequent oxidation and carbon activation could be used to develop nano-sized NiO particles with good exposure to the electrolytes. Similarly, the use of manganese nitrate may also be used to nucleate MnO_2 particles within a carbon foam substrate.

Alternative methods of CNT fabrication could also be utilized to impregnate the

carbon foams with SWCNTs. The use of aerosol methods is commonly used in SWCNT synthesis and could be used to grow the CNTs in the gas to be carried into the bulk morphology of the carbon foams. This could be combined with carbon foams with NiO or MnO_2 particles embedded within the bulk macro-structure to increase surface area, pseudo-capacitance, and conductivity.

Electrical conductivity of carbon materials for use in batteries and capacitors is also an important factor. Chemical doping by nitrogen or boron could increase the conductivity of the foam to reduce internal resistance.

6.1.4 Metal Foams

Metal foams have a variety of applications, however their manufacturing cost is often high and the process complex. Simply by having a cheaper alternative to the current methods of production makes the use of carbon foams as a sacrificial scaffold a valuable process. Applications include: thermal heat sinks and heat exchangers; energy absorption during mechanical stress as in automotive dampening during a crash; and medical prosthetics. Metal foams also have uses as three-dimensional electrochemical current collectors for both batteries and capacitors.

6.2 Concluding Remarks

Carbon foams have the potential to impact our world in a variety of ways and their applications are numerous. A great deal of time and persistence is required to master the organic chemistry, thermodynamics, and metallurgy needed simply to explain the synthesis

processes. I wish luck upon anyone who dares to try their hand at it, much less pursue the potential applications. Thank you reading my work and good luck.

Bibliography

[1] Aaaaaa. Carbon - Cobalt. *Proceedings, 4th International Conference on Earthquake Geotechnical Engineering, Paper 1454*, 257(1990):16014, 2007.

[2] Aaaaaa. Carbon - Nickel. *Proceedings, 4th International Conference on Earthquake Geotechnical Engineering, Paper 1454*, 20(1970):16014, 2007.

[3] Aaaaaa. Iron - Carbon. *Proceedings, 4th International Conference on Earthquake Geotechnical Engineering, Paper 1454*, 228:16014, 2007.

[4] Matthew J Allen, Vincent C Tung, and Richard B Kaner. Honeycomb Carbon : A Review of Graphene. pages 132–145, 2010.

[5] Thorsten Allscher, Peter Klüfers, and Peter Mayer. *Carbohydrate-Metal Complexes: Structural Chemistry of Stable Solution Species*. 2008.

[6] I. Alstrup. A new model explaining carbon filament growth on nickel, iron, and NiCu alloy catalysts. *Journal of Catalysis*, 109(2):241–251, 1988.

[7] Mkhoyan K Andre, A W Contryman, J Silcox, D A Stewart, G Eda, C Mattevi, S Miller, and M Chhowalla. Atomic and electronic structure of graphene-oxide. *Nano Letters*, 9(3):1058, 2010.

[8] F Antunes, O Lobo, J Corat, and J Trava. Influence of diameter in the Raman spectra of aligned multi-walled carbon nanotubes. *Carbon Nanotubes*, 45:913–921, 2007.

[9] ASM International. *ASM Handbook: Vol 03, Alloy Phase Diagrams*, volume 7. 2004.

[10] Azam Azam, Arham S Ahmed, Mohammad Oves, Mohammad S Khan, Sami S Habib, and Adnan Memic. Antimicrobial activity of metal oxide nanoparticles against Gram-positive and Gram-negative bacteria: a comparative study. *Ijnm*, (7(7)):6003–6009, 2012.

[11] Perla B. Balbuena and Yixuan Wang. *Lithium-Ion Batteries - Solid-Electrolyte Interphase*. Imperial College Press, London, 2004.

[12] Joyita Banerjee and Kingshuk Dutta. Materials for Electrodes of Li-Ion Batteries: Issues Related to Stress Development. *Critical Reviews in Solid State and Materials Sciences*, 42(3):218–238, 2017.

[13] Galen Barbose, Naim Darghouth, and Dev Millstein. Tracking the Sun IX: The Installed Price of Residential and Non-Residential Photovoltaic Systems in the United States. *LBNL*, (August), 2016.

[14] T. P. Barnett, J. C. Adam, and D. P. Lettenmaier. Potential impacts of a warming climate on water availability in snow-dominated regions. *Nature*, 438(7066):303–309, 2005.

[15] Hamed Hosseini Bay, Daisy Patino, Zafer Mutlu, Paige Romero, Mihrimah Ozkan, and Cengiz S Ozkan. Scalable Multifunctional Ultra-thin Graphite Sponge: Free-standing, Superporous, Superhydrophobic, Oleophilic Architecture with Ferromagnetic Properties for Environmental Cleaning. *Scientific reports*, 6:21858, jan 2016.

[16] Hosseini Bay. Design, Synthesis and Characterization of Novel Graphene-Based Nanoarchitectures for Sustainability. *UCR PhD*, 2015.

[17] François Béguin, Volker Presser, Andrea Balducci, and Elzbieta Frackowiak. Carbons and electrolytes for advanced supercapacitors. *Advanced Materials*, 26(14):2219–2251, 2014.

[18] M. Beltzer and S. Jahanmir. Role of Dispersion Interactions Between Hydrocarbon Chains in Boundary Lubrication. *A S L E Transactions*, 30(1):47–54, 1987.

[19] Bruce a Jr. Benner, Nelson P Bryner, Stephen a Wise, George W Mulholland, Robert C Lao, and Mervin F Fingas. Polycyclic aromatic hydrocarbon emissions from the combustion of crude oil on water. *Environmental Science & Technology*, 24(9):1418–1427, 1990.

[20] Hengchang Bi, Xiao Xie, Kuibo Yin, Yilong Zhou, Shu Wan, Longbing He, Feng Xu, Florian Banhart, Litao Sun, and Rodney S. Ruoff. Spongy graphene as a highly efficient and recyclable sorbent for oils and organic solvents. *Advanced Functional Materials*, 22(21):4421–4425, 2012.

[21] Hengchang Bi, Zongyou Yin, Xiehong Cao, Xiao Xie, Chaoliang Tan, Xiao Huang, Bo Chen, Fangtao Chen, Qingling Yang, Xinyang Bu, Xuehong Lu, and Litao Sun. Carbon Fiber Aerogel Made from Raw Cotton : A Novel , Effi cient and Recyclable Sorbent for Oils and Organic Solvents. pages 5916–5921, 2013.

[22] M. J. Bleda-Martínez, J. A. Maciá-Agulló, D. Lozano-Castelló, E. Morallón, D. Cazorla-Amorós, and A. Linares-Solano. Role of surface chemistry on electric double layer capacitance of carbon materials. *Carbon*, 43(13):2677–2684, 2005.

[23] L. Bokobza and J. Zhang. Raman spectroscopic characterization of multiwall carbon nanotubes and of composites. *Express Polymer Letters*, 6(7):601–608, 2012.

[24] Wolfgang Brockner, Claus Ehrhardt, and Mimoza Gjikaj. Thermal decomposition of nickel nitrate hexahydrate , Ni (NO 3) 2 · 6H 2 O , in comparison to Co (NO 3) 2 · 6H 2 O and Ca (NO 3) 2 · 4H 2 O. 456(3):64–68, 2007.

[25] William D. Calliester. Iron-Carbon Phase Diagram. *Materials Science and Engineering: An Introduction*, pages 1–34, 2007.

[26] Victor Chabot, Drew Higgins, Aiping Yu, and Xingcheng Xiao. Environmental Science material synthesis and applications to energy. pages 1564–1596, 2014.

[27] X. Chen, J. P. Cheng, Q. L. Shou, F. Liu, and X. B. Zhang. Effect of calcination temperature on the porous structure of cobalt oxide micro-flowers. *CrystEngComm*, 14(4):1271–1276, 2012.

[28] M. Chhowalla, K. B K Teo, C. Ducati, N. L. Rupesinghe, G. A J Amaratunga, A. C. Ferrari, D. Roy, J. Robertson, and W. I. Milne. Growth process conditions of vertically aligned carbon nanotubes using plasma enhanced chemical vapor deposition. *Journal of Applied Physics*, 90(10):5308–5317, 2001.

[29] Dagmar Chudobova, Simona Dostalova, Branislav Ruttkay-Nedecky, Roman Guran, Miguel Angel Merlos Rodrigo, Katerina Tmejova, Sona Krizkova, Ondrej Zitka, Vojtech Adam, and Rene Kizek. The effect of metal ions on Staphylococcus aureus revealed by biochemical and mass spectrometric analyses. *Microbiological Research*, 170:147–156, 2015.

[30] R. G. Coltters. Thermodynamics of binary metallic carbides: A review. *Materials Science and Engineering*, 76(C):1–50, 1985.

[31] B. E. Conway. *Electrochemical Supercapacitors - Scientific Fundamentals and Technological Applications*. Kluwer Academic / Plenum Publishers, New York, Chichester, Weinheim, Brisbane, Singapore, Toronto, 1st edition, 1999.

[32] Timothy J Crone and Maya Tolstoy. Magnitude of the 2010 Gulf of Mexico oil leak. *Science*, 330(October):634, 2010.

[33] J. R. Dahn, T. Zheng, Y. Liu, and J. S. Xue. Mechanisms for Lithium Insertion in Carbonaceous Materials. *Science*, 270(5236):590–593, oct 1995.

[34] Hongjie Dai. Carbon nanotubes: Synthesis, integration, and properties. *Accounts of Chemical Research*, 35(12):1035–1044, 2002.

[35] Jonathan Dantzig and Michel Rappaz. *Solidification*. EFPL Press, 2nd edition, aug 2009.

[36] Christian P. Deck and Kenneth Vecchio. Prediction of carbon nanotube growth success by the analysis of carbon-catalyst binary phase diagrams. *Carbon*, 44(2):267–275, 2006.

[37] Katerina Dedkova, Barbora Janikova, Katerina Matejova, Kristina Cabanova, Rostislav Vana, Ales Ale?? Kalup, Marianna Hundakova, Jana Kukutschova, Kate??ina D??dkov??, Barbora Jan??kov??, Kate??ina Mat??jov??, Kristina ??abanov??, Rostislav V????a, Ales Ale?? Kalup, Marianna Hund??kov??, and Jana Kukutschov?? ZnO/graphite composites and its antibacterial activity at different conditions. *Journal of Photochemistry and Photobiology B: Biology*, 151:256–263, 2015.

[38] P Dhamelincourt and J Laureyns. Carbon 1994 TascónCuesta - Raman microprobe studies on carbon materials.pdf. 32(8):1523–1532, 1994.

[39] Mamadou Diarra, Hakim Amara, François Ducastelle, and Christophe Bichara. Carbon solubility in nickel nanoparticles: A grand canonical Monte Carlo study. *Physica Status Solidi (B) Basic Research*, 249(12):2629–2634, 2012.

[40] Noah S Diffenbaugh, Daniel L Swain, and Danielle Touma. Anthropogenic warming has increased drought risk in California. *Proceedings of the National Academy of Sciences*, 112(13):3931–3936, 2015.

[41] Feng Ding, Peter Larsson, J. Andreas Larsson, Rajeev Ahuja, Haiming Duan, Arne Rosen, and Kim Bolton. The importance of strong carbon-metal adhesion for catalytic nucleation of single-walled carbon nanotubes. *Nano Letters*, 8(2):463–468, 2008.

[42] Feng Ding, Arne Rosén, Eleanor E B Campbell, Lena K L Falk, and Kim Bolton. Graphitic encapsulation of catalyst particles in carbon nanotube production. *Journal of Physical Chemistry B*, 110(15):7666–7670, 2006.

[43] Dejan Djurovic, Bengt Hallstedt, Jörg von Appen, and Richard Dronskowski. Thermodynamic assessment of the Fe–Mn–C system. *Calphad*, 35(4):479–491, 2011.

[44] M. S. DRESSELHAUS, G. DRESSELHAUS, and P. C. EKLUND. *Science of Fullerenes and Carbon Nanotubes*. Elsevier, 1996.

[45] Mildred S Dresselhaus, G. Dresselhaus, and Ph. Avouris. Carbon nanotubes: synthesis, properties, and applications, 2000.

[46] M.S. Dresselhaus, G. Dresselhaus, A. Jorio, A.G. Souza Filho, and R. Saitof. Raman spectroscopy on isolated single wall carbon nanotubes. *Carbon*, (40):2043–2061, 2002.

[47] Bo Duan, Huimin Gao, Meng He, and Lina Zhang. Hydrophobic modification on surface of chitin sponges for highly effective separation of oil. *ACS Applied Materials and Interfaces*, 6(22):19933–19942, 2014.

[48] Bo Duan, Huimin Gao, Meng He, and Lina Zhang. Hydrophobic modification on surface of chitin sponges for highly effective separation of oil. *ACS applied materials & interfaces*, 6(22):19933–42, nov 2014.

[49] Isabelle Durance and S J Ormerod. Climate change effects on upland stream macroinvertebrates over a 25-year period. *Global Change Biology*, 13(5):942–957, 2007.

[50] Kristina Edström, Marie Herstedt, and Daniel P. Abraham. A new look at the solid electrolyte interphase on graphite anodes in Li-ion batteries. *Journal of Power Sources*, 153(2):380–384, 2006.

[51] Morinubo Endo, Sumio Iijima, and Mildred S. Dresselhaus. Carbon Nanotubes. *Tetrahedron Letters*, page 202, 1996.

[52] Phase Equilibria. Al – C (Aluminum – Carbon). pages 5–8.

[53] Mohamed A. Fahim, Taher A. Alsahhaf, and Amal Elkilani. *Fundamentals of Petroleum Refining*. 2010.

[54] Larry R Faulkner and Allen J Bard. *Electrochemical Methods: Fundamentals and Applications*. John Wiley & Sons, INC, New York, Chichester, Weinheim, Brisbane, Singapore, Toronto, 2nd edition, sep 2001.

[55] Feng Ding, Arne Roséna, and Kim Bolton. Dependence of SWNT Growth Mechanism on Temperature and Catalyst Particle Size: Bulk versus Surface Diffusion. *Carbon*, pages 1–8, 2005.

[56] A C Ferrari, J C Meyer, V Scardaci, C Casiraghi, M Lazzeri, F Mauri, S Piscanec, D Jiang, K S Novoselov, S Roth, and A K Geim. Raman Spectrum of Graphene and Graphene Layers. 187401(NOVEMBER):1–4, 2006.

[57] A. C. Ferrari and J. Robertson. Interpretation of Raman spectra of disordered and amorphous carbon. *Physical Review B*, 61(20):14095–14107, may 2000.

[58] Andrea Carlo Ferrari and J. Robertson. Raman spectroscopy of amorphous, nanostructured, diamond-like carbon, and nanodiamond. *Philosophical Transactions of the Royal Society A: Mathematical, Physical and Engineering Sciences*, 362(1824):2477–2512, nov 2004.

[59] J. Gamby, P. L. Taberna, P. Simon, J. F. Fauvarque, and M. Chesneau. Studies and characterisations of various activated carbons used for carbon/carbon supercapacitors. *Journal of Power Sources*, 101(1):109–116, 2001.

[60] J. Gavillet, A. Loiseau, F. Ducastelle, S. Thair, P. Bernier, O. Stéphan, J. Thibault, and J. C. Charlier. Microscopic mechanisms for the catalyst assisted growth of single-wall carbon nanotubes. *Carbon*, 40(10):1649–1663, 2002.

[61] J. Gavillet, A. Loiseau, C. Journet, F. Willaime, F. Ducastelle, and J. C. Charlier. Root-growth mechanism for single-wall carbon nanotubes. *Physical Review Letters*, 87(27):275504–1–275504–4, 2001.

[62] Peter H. Gleick. Water, Drought, Climate Change, and Conflict in Syria. *Weather, Climate, and Society*, 6(3):331–340, 2014.

[63] Gretchen Goodbody-Gringley, Dana L Wetzel, Daniel Gillon, Erin Pulster, Allison Miller, and Kim B Ritchie. Toxicity of Deepwater Horizon Source Oil and the Chemical Dispersant, Corexit®9500, to Coral Larvae. *PLOS ONE*, 8(1):1–10, 2013.

[64] A. Gorbunov, O. Jost, W. Pompe, and A. Graff. Solid-liquid-solid growth mechanism of single-wall carbon nanotubes. *Carbon*, 40(1):113–118, 2002.

[65] D. Graf, F. Molitor, K. Ensslin, C. Stampfer, A. Jungen, C. Hierold, and L. Wirtz. Raman imaging of graphene. *Solid State Communications*, 143(1-2):44–46, 2007.

[66] Xuchun Gui, Hongbian Li, Kunlin Wang, Jinquan Wei, Yi Jia, Zhen Li, Lili Fan, Anyuan Cao, Hongwei Zhu, and Dehai Wu. Recyclable carbon nanotube sponges for oil absorption. *Acta Materialia*, 59(12):4798–4804, 2011.

[67] Béla Gyurcsik and László Nagy. Carbohydrates as ligands: Coordination equilibria and structure of the metal complexes. *Coordination Chemistry Reviews*, 203(1):81–149, 2000.

[68] M. Hämäläinen and I. Isomäki. Thermodynamic evaluation of the C-Co-Zn system. *Journal of Alloys and Compounds*, 392(1-2):220–224, 2005.

[69] E L Hansen, H Hemmen, D M Fonseca, C Coutant, K D Knudsen, T S Plivelic, D Bonn, and J O Fossum. Swelling transition of a clay induced by heating. *Scientific Reports*, 2(1):618, 2012.

[70] Peter Harris. *Chemistry and Physics of Carbon - Vol 30*, volume 13. 1997.

[71] M. Hasebe, H. Ohtani, and T. Nishizawa. Effect of magnetic transition on solubility of carbon in bcc Fe and fee Co-Ni alloys. *Metallurgical Transactions A*, 16(5):913–921, 1985.

[72] Yoshikazu Homma, Yoshiro Kobayashi, Toshio Ogino, Daisuke Takagi, Roichi Ito, Yung Joon Yj Yung Joon Jung, and Pulickel M. Pm Ajayan. Role of Transition Metal Catalysts in Single-Walled Carbon Nanotube Growth in Chemical Vapor Deposition. *The Journal of Physical Chemistry B*, 107(44):12161–12164, 2003.

[73] Zhonghua Hu and M. P. Srinivasan. Mesoporous high-surface-area activated carbon. *Microporous and Mesoporous Materials*, 43(3):267–275, 2001.

[74] Robert A. Huggins. *Advanced Batteries - Materials Science Aspects*. Springer US, Boston, MA, 2009.

[75] William S. Hummers and Richard E. Offeman. Preparation of Graphitic Oxide. *Journal of the American Chemical Society*, 80(6):1339–1339, 1958.

[76] Sumio Iijima. Helical microtubules of graphitic carbon. *Nature*, 354(6348):56–58, nov 1991.

[77] M Inagaki, F Kang, M Toyoda, and H Konno. *Advanced Materials Science and Engineering of Carbon*, volume 067. 2013.

[78] Michio Inagaki and Feiyu Kang. *Materials Science and Engineering of Carbon: Characterization*. 2016.

[79] IPCC. *Climate change 2007: Impacts, adaptation and vulnerability.* 2007.

[80] K. Ishida and T. Nishizawa. The C-Co(Carbon-Cobalt) system. *Journal of Phase Equilibria*, 12(4):417–424, 1991.

[81] Junyi Ji, Li Li Zhang, Hengxing Ji, Yang Li, Xin Zhao, Xin Bai, Xiaobin Fan, Fengbao Zhang, and Rodney S. Ruoff. Nanoporous Ni(OH)2thin film on 3d ultrathin-graphite foam for asymmetric supercapacitor. *ACS Nano*, 7(7):6237–6243, 2013.

[82] Bruce E Johansen. *Climate Change: An Encyclopedia of Science, Society, and Solutions.* ABC- CLIO, Santa Barbara, CA - Denver Colorado, 2017.

[83] Christian; Julien, Alain; Mauger, Ashok; Vijh, and Karim Zaghib. *Lithium Batteries - Science and Technology.* 2016.

[84] Konrad Kabza, Jason E. Gestwicki, and Jessica L. McGrath. Contact angle goniometry as a tool for surface tension measurements of solids, using zisman plot method. A physical chemistry experiment. *Journal of Chemical Education*, 77(1):63–65, 2000.

[85] P.S. Karthik, A.L. Himaja, and Surya Prakash Singh. Carbon-allotropes: synthesis methods, applications and future perspectives. *Carbon letters*, 15(4):219–237, 2014.

[86] J. H. Kaufman, S. Metin, and D. D. Saperstein. Symmetry breaking in nitrogen-doped amorphous carbon: Infrared observation of the Raman-active G and D bands. *Physical Review B*, 39(18):13053–13060, jun 1989.

[87] Qingqing Ke and John Wang. Graphene-based materials for supercapacitor electrodes – A review. *Journal of Materiomics*, 2(1):37–54, 2016.

[88] Kristy J. Kroeker, Rebecca L. Kordas, Ryan N. Crim, and Gerald G. Singh. Meta-analysis reveals negative yet variable effects of ocean acidification on marine organisms. *Ecology Letters*, 13(11):1419–1434, 2010.

[89] Yogesh Kumar, Jordan Ringenberg, Soma Shekara Depuru, Vijay K. Devabhaktuni, Jin Woo Lee, Efstratios Nikolaidis, Brett Andersen, and Abdollah Afjeh. Wind energy: Trends and enabling technologies. *Renewable and Sustainable Energy Reviews*, 53:209–224, 2016.

[90] Haruko Kurihara. Effects of CO2-driven ocean acidification on the early developmental stages of invertebrates. *Marine Ecology Progress Series*, 373:275–284, 2008.

[91] R Lal. Soil Carbon Sequestration Impacts on Global Climate Change and Food Security. *American Association for the Advancement of Science*, 304(5677):1623–7, 2004.

[92] Chee Huei Lee, Nick Johnson, Jaroslaw Drelich, and Yoke Khin Yap. The performance of superhydrophobic and superoleophilic carbon nanotube meshes in water-oil filtration. *Carbon*, 49(2):669–676, 2011.

[93] Zofia Lendzion-Bielun, Urszula Narkiewicz, and Walerian Arabczyk. Cobalt-based catalysts for ammonia decomposition. *Materials*, 6(6):2400–2409, 2013.

[94] Wen Ru Li, Xiao Bao Xie, Qing Shan Shi, Hai Yan Zeng, You Sheng Ou-Yang, and Yi Ben Chen. Antibacterial activity and mechanism of silver nanoparticles on Escherichia coli. *Applied Microbiology and Biotechnology*, 85(4):1115–1122, 2010.

[95] Z. Q. Li, C. J. Lu, Z. P. Xia, Y. Zhou, and Z. Luo. X-ray diffraction patterns of graphite and turbostratic carbon. *Carbon*, 45(8):1686–1695, 2007.

[96] Sumio Lijima. Single shell carbon nanotubes of 1-nm diameter.

[97] David Linden and Thomas B. Reddy. *Handbook of Batteries - 3rd Edition*. 2002.

[98] Nancy Lindisfarne and Steve Rayner. *Climate Change - Realities, Impacts Over Ice Cap, Sea Level and Risks*, volume 32. InTech, Rijeka, Croatia, jan 2013.

[99] Chueh Liu, Changling Li, Kazi Ahmed, Wei Wang, Ilkeun Lee, Francisco Zaera, Cengiz S. Ozkan, and Mihrimah Ozkan. Scalable, Binderless, and Carbonless Hierarchical Ni Nanodendrite Foam Decorated with Hydrous Ruthenium Dioxide for 1.6 v Symmetric Supercapacitors. *Advanced Materials Interfaces*, 3(6):1–8, 2016.

[100] J. Livage, M. Henry, and C. Sanchez. Sol-gel chemistry of transition metal oxides. *Progress in Solid State Chemistry*, 18(4):259–341, 1988.

[101] Craig Loehle and David LeBlanc. Model-based assessments of climate change effects on forests: A critical review. *Ecological Modelling*, 90(1):1–31, 1996.

[102] F. London. Zur Theorie und Systematik der Molekularkr??fte. *Zeitschrift f??r Physik*, 63(3-4):245–279, 1930.

[103] Fritz London. The general theory of molecular forces. *Trans. Faraday Soc.*, 33(8):8–26, 1937.

[104] Wen Lu and Liming Dai. Carbon Nanotube Supercapacitors. In Jose Mauricio Marulanda, editor, *Carbon Nanotubes*, pages 563–591. InTech, 2010.

[105] Jia Ma, Tao Xue, and Xue Qin. Sugar-derived carbon/graphene composite materials as electrodes for supercapacitors. *Electrochimica Acta*, 115:566–572, 2014.

[106] Minglin Ma, Randal M Hill, and Gregory C Rutledge. A Review of Recent Results on Superhydrophobic Materials Based on Micro- and Nanofibers. *Journal of Adhesion Science and Technology*, 22(March 2015):1799–1817, 2008.

[107] Arjun Makhijani. *Carbon-Free and Nuclear-Free: A Roadmap for U.S. Energy Policy*. IEER Press, RDR Books, Takoma Park, MD, 1st edition, 2007.

[108] Satish M. Manocha. Porous carbons. *Sadhana*, 28(1-2):335–348, 2003.

[109] Daniela C. D.C Marcano, D.V Dmitry V. Kosynkin, Jacob M. Berlin, Alexander Sinitskii, Zhengzong Z Sun, Alexander Slesarev, Lawrence B. Alemany, Wei Lu, and James M. Tour. Improved synthesis of graphene oxide. *ACS Nano*, 4(8):4806–4814, 2010.

[110] Ralph J. Masaki, Yoshio, Kozawa, Akiya, Brodd. *Lithium-Ion Batteries - Science and Technologies*, volume 53. 2013.

[111] Physics Condensed Matter. The Role of Metal Nanoparticles in the Catalytic Production of Single-Walled Carbon Nanotubes — A Review. (October 2003), 2017.

[112] Patrick May, Michele Lazzeri, Pedro Venezuela, Felix Herziger, Gordon Callsen, Juan S. Reparaz, Axel Hoffmann, Francesco Mauri, and Janina Maultzsch. Signature of the two-dimensional phonon dispersion in graphene probed by double-resonant Raman scattering. *Physical Review B - Condensed Matter and Materials Physics*, 87(7):1–6, 2013.

[113] C.L. L Mehltretter and C.E. E Rist. Saccharic and Oxalic Acids Oxidation of Dextrose by the Nitric Acid of Dextrose. *Agricultural and Food Chemistry*, 1(12):779–783, 1953.

[114] S. K. Mehta, Savita Chaudhary, and Michael Gradzielski. Time dependence of nucleation and growth of silver nanoparticles generated by sugar reduction in micellar media. *Journal of Colloid and Interface Science*, 343(2):447–453, 2010.

[115] Terrence P. Mernagh, Ralph P. Cooney, and Robert A. Johnson. Raman spectra of Graphon carbon black. *Carbon*, 22(1):39–42, 1984.

[116] Lothar Meyer. The surface reaction of graphite with oxygen carbon dioxide and water vapour at low pressures. *Transactions of the Faraday Society*, 34(1056):1056, 1938.

[117] Andrew D Mills, Dev Millstein, Seongeun Jeong, Luke Lavin, Ryan Wiser, and Mark Bolinger. Estimating the Value of Offshore Wind Along the United States ' Eastern Coast. page 21, 2018.

[118] Jacob Mu and D. D. Perlmutter. Thermal decomposition of metal nitrates and their hydrates. *Thermochimica Acta*, 56(3):253–260, 1982.

[119] R S Nerem, B D Beckley, J T Fasullo, B D Hamlington, D Masters, and G T Mitchum. Climate-change–driven accelerated sea-level rise detected in the altimeter era. *Proceedings of the National Academy of Sciences*, 0:201717312, 2018.

[120] Robert Neuman. Carbohydrates from Organic Chemistry. In *Organic Chemistry*, chapter 20, page Chapter 20. 1999.

[121] Erik C. Neyts, Yasushi Shibuta, Adri C T Van Duin, and Annemie Bogaerts. Catalyzed growth of carbon nanotube with definable chirality by hybrid molecular dynamics-force biased monte carlo simulations. *ACS Nano*, 4(11):6665–6672, 2010.

[122] The An Nguyen, Jae Ung Lee, Duhee Yoon, and Hyeonsik Cheong. Excitation energy dependent raman signatures of ABA- and ABC-stacked few-layer graphene. *Scientific Reports*, 4:1–5, 2014.

[123] Sebastian Osswald, Mickael Havel, and Yury Gogotsi. Monitoring oxidation of multiwalled carbon nanotubes by Raman spectroscopy. *Journal of Raman Spectroscopy*, 38(6):728–736, jun 2007.

[124] Aleš Panáček, Libor Kvítek, Robert Prucek, Milan Kolář, Renata Večeřová, Naděžda Pizúrová, Virender K. Sharma, Tat'Jana Nevěčná, and Radek Zbořil. Silver colloid nanoparticles: Synthesis, characterization, and their antibacterial activity. *Journal of Physical Chemistry B*, 110(33):16248–16253, 2006.

[125] Sudipa Panigrahi, Subrata Kundu, Sujit Ghosh, Sudip Nath, and Tarasankar Pal. General method of synthesis for metal nanoparticles. *Journal of Nanoparticle Research*, 6(4):411–414, 2004.

[126] J. S. Park, A. Reina, R. Saito, J. Kong, G. Dresselhaus, and M. S. Dresselhaus. 2D band Raman spectra of single, double and triple layer graphene. *Carbon*, 47(5):1303–1310, 2009.

[127] M. L. Parry, C. Rosenzweig, A. Iglesias, M. Livermore, and G. Fischer. Effects of climate change on global food production under SRES emissions and socio-economic scenarios. *Global Environmental Change*, 14(1):53–67, 2004.

[128] Shilong Piao, Philippe Ciais, Yao Huang, Zehao Shen, Shushi Peng, Junsheng Li, Liping Zhou, Hongyan Liu, Yuecun Ma, Yihui Ding, Pierre Friedlingstein, Chunzhen Liu, Kun Tan, Yongqiang Yu, Tianyi Zhang, and Jingyun Fang. The impacts of climate change on water resources and agriculture in China. *Nature*, 467(7311):43–51, 2010.

[129] M. A. Pimenta, G. Dresselhaus, M. S. Dresselhaus, L. G. Cançado, A. Jorio, and R. Saito. Studying disorder in graphite-based systems by Raman spectroscopy. *Physical Chemistry Chemical Physics*, 9(11):1276–1291, 2007.

[130] B. Predel. Phase Equilibria, Crystallographic and Thermodynamic Data of Binary Alloys · C-Cu (Carbon-Copper). *Phase Equilibria, Crystallographic and Thermodynamic Data of Binary Alloys · B-Ba – C-Zr*, 5b(1956):1986, 1992.

[131] S. Reich and C. Thomsen. Raman spectroscopy of graphite. *Philosophical Transactions of the Royal Society A: Mathematical, Physical and Engineering Sciences*, 362(1824):2271–2288, nov 2004.

[132] Brent W. Ritchie, John C. Crotts, Anita Zehrer, and George T. Volsky. Understanding the Effects of a Tourism Crisis: The Impact of the BP Oil Spill on Regional Lodging Demand. *Journal of Travel Research*, 53(1):12–25, 2013.

[133] Peter Rodgers. *Nanoscience and Technology*, volume 136. Co-Published with Macmillan Publishers Ltd, UK, aug 2009.

[134] Julio A. Rodríguez-Manzo, Mauricio Terrones, Humberto Terrones, Harold W. Kroto, Litao Sun, and Florian Banhart. In situ nucleation of carbon nanotubes by the injection of carbon atoms into metal particles. *Nature Nanotechnology*, 2(5):307–311, 2007.

[135] a Rundle, D Tang, H Hibshoosh, A Estabrook, F Schnabel, W Cao, S Grumet, and F P Perera. The relationship between genetic damage from polycyclic aromatic hydrocarbons in breast tissue and breast cancer. *Carcinogenesis*, 21(7):1281–1289, 2000.

[136] Andrew Rundle, Lori Hoepner, Abeer Hassoun, Sharon Oberfield, Greg Freyer, Darrell Holmes, Marilyn Reyes, James Quinn, David Camann, Frederica Perera, and Robin Whyatt. Association of childhood obesity with maternal exposure to ambient air polycyclic aromatic hydrocarbons during pregnancy. *American Journal of Epidemiology*, 175(11):1163–1172, 2012.

[137] R. Saito, G. Dresselhaus, and M. S. Dresselhaus. *Physical Properties of Carbon Nanotubes*. Imperial College Press, 1998.

[138] Luis F Sala, Laura Ciullo, Rubén Lafarga, and Sandra Signorella. Kinetics and mechanism of the oxidation of d-galactose by copper(II) in acidic medium. *Polyhedron*, 14(9):1207–1211, may 1995.

[139] Noriaki Sano, Hiroshi Akazawa, Takeyuki Kikuchi, and Tatsuo Kanki. Separated synthesis of iron-included carbon nanocapsules and nanotubes by pyrolysis of ferrocene in pure hydrogen. *Carbon*, 41(11):2159–2162, 2003.

[140] Mark Schrope and Beyond T H E Edge. Deep wounds. *Nature*, 472(14 Aprill 2011):152–154, 2011.

[141] Edward A G Schuur, James Bockheim, Josep G Canadell, Eugenie Euskirchen, Christopher B Field, Sergey V Goryachkin, Stefan Hagemann, Peter Kuhry, Peter M Lafleur, Hanna Lee, Galina Mazhitova, Frederick E Nelson, Annette Rinke, Vladimir E Romanovsky, Nikolay Shiklomanov, Charles Tarnocai, Sergey Venevsky, Jason G Vogel, and Sergei A Zimov. Vulnerability of Permafrost Carbon to Climate Change: Implications for the Global Carbon Cycle. *BioScience*, 58(8):701–714, 2008.

[142] J. Schwan, S. Ulrich, V. Batori, H. Ehrhardt, and S. R.P. Silva. Raman spectroscopy on amorphous carbon films. *Journal of Applied Physics*, 80(1):440–447, 1996.

[143] Lei Shi, Philip Rohringer, Kazu Suenaga, Yoshiko Niimi, Jani Kotakoski, Jannik C. Meyer, Herwig Peterlik, Marius Wanko, Seymur Cahangirov, Angel Rubio, Zachary J. Lapin, Lukas Novotny, Paola Ayala, and Thomas Pichler. Confined linear carbon chains as a route to bulk carbyne. *Nature Materials*, 15(6):634–639, 2016.

[144] V. Sihvonen. The influence of keto- and ketene groups, adsorbed molecules and ions on the mechanism of carbon oxidation. *Transactions of the Faraday Society*, 34:1062, 1938.

[145] Brian R Silliman, Johan van de Koppel, Michael W McCoy, Jessica Diller, Gabriel N Kasozi, Kamala Earl, Peter N Adams, and Andrew R Zimmerman. Degradation and resilience in Louisiana salt marshes after the BP-Deepwater Horizon oil spill. *Proceedings of the National Academy of Sciences of the United States of America*, 109(28):11234–9, jul 2012.

[146] Patrice Simon, Yury Gogotsi, and Bruce Dunn. Where Do Batteries End and Supercapacitors Begin? *Science*, 343(March):1210–1211, 2014.

[147] M. Singleton and P. Nash. The C-Ni (Carbon-Nickel) system. *Bulletin of Alloy Phase Diagrams*, 10(2):121–126, 1989.

[148] Liesje Sintubin, Wim De Windt, Jan Dick, Jan Mast, David Van Der Ha, Willy Verstraete, and Nico Boon. Lactic acid bacteria as reducing and capping agent for the fast and efficient production of silver nanoparticles. *Applied Microbiology and Biotechnology*, 84(4):741–749, 2009.

[149] Ranjani V. Siriwardane, Ming-Shing Shen, Edward P. Fisher, and James A. Poston. Adsorption of CO ₂ on Molecular Sieves and Activated Carbon. *Energy & Fuels*, 15(2):279–284, 2001.

[150] Tyler N. Smith, Kirk Hash, Cara Lee Davey, Heidi Mills, Holly Williams, and Donald E. Kiely. Modifications in the nitric acid oxidation of d-glucose. *Carbohydrate Research*, 2012.

[151] Susan Solomon, G.-K. Plattner, Reto Knutti, and Pierre Friedlingstein. Irreversible climate change due to carbon dioxide emissions. *Proceedings of the National Academy of Science*, 106:1704–1709, 2009.

[152] Yang Song, Rui Peng, Dale K Hensley, Peter V Bonnesen, Liangbo Liang, Zili Wu, Harry M Meyer, Miaofang Chi, Cheng Ma, Bobby G Sumpter, and Adam J Rondinone. High-Selectivity Electrochemical Conversion of CO 2 to Ethanol using a Copper Nanoparticle/N-Doped Graphene Electrode.

[153] United States, Jane Lubchenco, Marcia McNutt, Bill Lehr, Mark Sogge, Mark Miller, Stephen Hammond, and William Conner. BP Deepwater Horizon Oil Budget : What Happened To the Oil ? 2010.

[154] J. C. Swartz. Solubility of graphite in cobalt and nickel. *Metallurgical and Materials Transactions B*, 2(8):2318–2320, 1971.

[155] Binary Systems. C – Zn (Carbon – Zinc). pages 1–2, 2000.

[156] M. A. Tamor and W. C. Vassell. Raman "fingerprinting" of amorphous carbon films. *Journal of Applied Physics*, 76(6):3823–3830, 1994.

[157] Dimitrios Tasis, Nikos Tagmatarchis, Alberto Bianco, and Maurizio Prato. Chemistry of carbon nanotubes. *Chemical Reviews*, 106(3):1105–1136, 2006.

[158] ITOPF The International Tanker Owners Pllution Federal Limited. OIL TANKER SPILL STATISTICS 2017. (January), 2018.

[159] Masahiro Toyoda and Michio Inagaki. Heavy oil sorption using exfoliated graphite. *Carbon*, 38(2):199–210, 2000.

[160] Masahiro Toyoda and Michio Inagaki. Sorption and Recovery of Heavy Oils by Using Exfoliated Graphite Part II: Recovery of heavy oil and recycling of exfoliated graphite. *Spill Science & Technology Bulletin*, 8(5–6):467–474, 2003.

[161] Masahiro Toyoda, Kouji Moriya, Jun-ichi Aizawa, Hidetaka Konno, and Michio Inagaki. Sorption and recovery of heavy oils by using exfoliated graphite Part I: Maximum sorption capacity. *Desalination*, 128(3):205–211, 2000.

[162] Harold F Upton. The Deepwater Horizon Oil Spill and the Gulf of Mexico Fishing Industry. *CRS Report for Congress*, pages 1–14, 2011.

[163] Chengwei Wang, Michael J. O'Connell, and Candace K. Chan. Facile one-pot synthesis of highly porous carbon foams for high-performance supercapacitors using template-free direct pyrolysis. *ACS Applied Materials and Interfaces*, 7(16):8952–8960, 2015.

[164] Shutao Wang and Lei Jiang. Definition of superhydrophobic states. *Advanced Materials*, 19(21):3423–3424, 2007.

[165] Xuebin Wang, Yuanjian Zhang, Chunyi Zhi, Xi Wang, Daiming Tang, Yibin Xu, Qunhong Weng, Xiangfen Jiang, Masanori Mitome, Dmitri Golberg, and Yoshio Bando. Three-dimensional strutted graphene grown by substrate-free sugar blowing for high-power-density supercapacitors. *Nature Communications*, 4(May):1–8, 2013.

[166] Yang Wen, Kai He, Yujie Zhu, Fudong Han, Yunhua Xu, Isamu Matsuda, Yoshitaka Ishii, John Cumings, and Chunsheng Wang. Expanded graphite as superior anode for sodium-ion batteries. *Nature communications*, 5(May):4033, 2014.

[167] Robert N. Wenzel. Resistance of Solid Surfaces. *Ind. Eng. Chem.*, 28:988–994, 1936.

[168] A L Westerling, H G Hidalgo, D R Cayan, and T W Swetnam. Warming and earlier spring increase Western U.S. forest wildfire activity. *Science*, 313(5789):940–943, 2006.

[169] Martin Winter and Ralph J. Brodd. What are batteries, fuel cells, and supercapacitors? *Chemical Reviews*, 104(10):4245–4269, 2004.

[170] Christoph T. Wirth, Bernhard C. Bayer, Andrew D. Gamalski, Santiago Esconjauregui, Robert S. Weatherup, Caterina Ducati, Carsten Baehtz, John Robertson, and Stephan Hofmann. The phase of iron catalyst nanoparticles during carbon nanotube growth. *Chemistry of Materials*, 24(24):4633–4640, 2012.

[171] Borong Wu, Yonghuan Ren, and Ning Li. *Electric Vehicles – The Benefits and Barriers*. 2011.

[172] Hongjuan Xi, Zhixian Gao, and Jianguo Wang. Kinetics of oxidative decarboxylation of 3,4-methylenedioxymandelic acid to piperonal with dilute nitric acid. *Industrial and Engineering Chemistry Research*, 48(23):10425–10430, 2009.

[173] Hongjuan Xi, Zhixian Gao, and Jianguo Wang. Kinetics of oxidative decarboxylation of 3,4-methylenedioxymandelic acid to piperonal with dilute nitric acid. *Industrial and Engineering Chemistry Research*, 48(23):10425–10430, 2009.

[174] Pinxian Xi, Liang Huang, Zhihong Xu, Fengjuan Chen, Li An, Ben Wang, and Zhong-Ning Chen. Low cost and robust soot dipped polyurethane sponge for highly efficient and recyclable oil and organic solvent cleanup. *RSC Adv.*, 4(103):59481–59485, 2014.

[175] K Yase, S Horiuchi, M Kyotani, M Yumura, K Uchida, S Ohshima, Y Kuriki, F Ikazaki, and N Yamahira. Angular-resolved EELS of a carbon nanotube. *Thin Solid Films*, 273(1-2):222–224, 1996.

[176] Yu Guo Yuan, Qiu Ling Peng, and Sangiliyandi Gurunathan. Effects of silver nanoparticles on multiple drug-resistant strains of Staphylococcus aureus and Pseudomonas aeruginosa from mastitis-infected goats: An alternative approach for antimicrobial therapy. *International Journal of Molecular Sciences*, 18(3), 2017.

[177] Lingling Zhang, Yunhong Jiang, Yulong Ding, Malcolm Povey, and David York. Investigation into the antibacterial behaviour of suspensions of ZnO nanoparticles (ZnO nanofluids). *Journal of Nanoparticle Research*, 9(3):479–489, 2007.

[178] Cheng Zhong, Yida Deng, Wenbin Hu, Jinli Qiao, Lei Zhang, and Jiujun Zhang. A review of electrolyte materials and compositions for electrochemical supercapacitors. *Chemical Society Reviews*, 44(21):7484–7539, 2015.

[179] Cheng Zhong and Wenbin Hu. *Electrolytes for Electrochemical Supercapacitors*. 2016.

[180] Hongwei Zhu, Kazutomo Suenaga, Ayako Hashimoto, Kouki Urita, Kenji Hata, and Sumio Iijima. Atomic-resolution imaging of the nucleation points of single-walled carbon nanotubes. *Small*, 1(12):1180–1183, 2005.

[181] Qing Zhu, Qinmin Pan, and Fatang Liu. Facile removal and collection of oils from water surfaces through superhydrophobic and superoleophilic sponges. *Journal of Physical Chemistry C*, 2011.

[182] Yanwu Zhu, Shanthi Murali, Weiwei Cai, Xuesong Li, Ji Won Suk, Jeffrey R. Potts, and Rodney S. Ruoff. Graphene and graphene oxide: Synthesis, properties, and applications. *Advanced Materials*, 22(35):3906–3924, 2010.